Alma Mater Studiorum - Università di Bologna

DOTTORATO DI RICERCA IN

FISICA

Ciclo 35

Settore Concorsuale: 02/A1 - FISICA SPERIMENTALE DELLE INTERAZIONI FONDAMENTALI

Settore Scientifico Disciplinare: FIS/01 - FISICA SPERIMENTALE

THE COSMIC RAY TAGGER OF THE ICARUS DETECTOR: CONSTRUCTION, COMMISSIONING AND PERFORMANCES IN THE FIRST PHYSICS RUN

Presentata da: Francesco Poppi

Coordinatore Dottorato

Michele Cicoli

Supervisore

Laura Patrizii

Esame finale anno 2023

This work was made possible
by my supervisors and all the technicians
who entrusted me and suffered my exuberance
during in its realization.

Abstract

The Short Baseline Neutrino Program at Fermilab aims to confirm or definitely rule out the existence of sterile neutrinos at the eV mass scale. The program will perform the most sensitive search in both the ν_e appearance and ν_μ disappearance channels along the Booster Neutrino Beamline. The far detector, ICARUS-T600, is a high-granularity Liquid Argon Time Projection Chamber located at 600 m from the Booster neutrino source and at shallow depth, thus exposed to a large flux of cosmic particles. Additionally, ICARUS is located 6° off axis with respect to the Neutrino beam from the Main Injector. This thesis presents the construction, installation and commissioning of the ICARUS Cosmic Ray Tagger system, providing a 4π coverage of the active liquid argon volume. By exploiting only the precise nanosecond scale synchronization of the cosmic tagger and the PMT optical flashes it is possible to determine if an event was likely triggered by a cosmic particle. The results show that using the Top Cosmic Ray Tagger alone a conservative rejection larger than 65% of the cosmic induced background can be achieved. Additionally, by requiring the absence of hits in the whole cosmic tagger system it is possible to perform a pre-selection of contained neutrino events ahead of the full event reconstruction.

Contents

Introduction

In the last decades, neutrino physics gathered more and more interest as the Nobel prize-winning discovery of neutrino oscillations demonstrated that neutrinos are massive particles. The discovery led to the standard three neutrino mixing paradigm where ν_e, ν_μ and ν_τ are superposition of ν_1, ν_2 and ν_3 massive states. Starting from the mid-1990's, a series of anomalous results were reported by neutrino oscillation experiments at relatively short baselines, suggesting the existence of at least an additional light sterile neutrino state. The Short Baseline Neutrino Program (SBN) at Fermilab aims to perform the most sensitive search for sterile neutrinos at the eV mass-scale through the analysis of both the ν_e appearance and ν_μ disappearance channels on the Booster Neutrino Beam. The novelty of the SBN Program is twofold: (I) the exploitation of a near and far detector system, (II) the implementation of the Liquid Argon Time Projection Chamber (LArTPC) technology for both the detectors. This configuration will allow to perform a joint analysis of the neutrino events detected at the Near and Far sites with constrained systematic uncertainty.

Three LArTPCs are located along the Booster Neutrino Beamline (BNB): SBND (the near detector), MicroBooNE and ICARUS (the far detector), at 110 m, 470 m and 600 m from the neutrino source, respectively. ICARUS is also exposed to the NuMI beam, $\sim$ 800 m from the proton target and 6° off-axis. The off-axis NuMI beam grants ICARUS acceptance to a significant flux of ν_μ and ν_e, in both neutrino and antineutrino mode beam configuration. The first phase of the SBN Program was carried out by MicroBooNE alone and it was completed at the beginning of 2021. The second phase of SBN is characterized by the joint program of the SBND and ICARUS experiments.

The ICARUS detector is located at shallow depth, thus exposed to a large flux of cosmic particles entering the detector during the 1.6 μs (BNB) or 9.6 μs (NuMI) neutrino beam-spill (*in time* activity) and during the $\sim$ 1 ms TPC drift time (*out of time* activity). In order to mitigate the rate of cosmic ray induced events, ICARUS is instrumented with a Cosmic Ray Tagger (CRT) system ensuring a 4π coverage of the detector. Additionally, 6 m water equivalent of concrete overburden are installed above the CRT system to suppress the soft electromagnetic and hadronic components of the

cosmic ray spectrum.

In this thesis I present the ICARUS CRT system, highlighting, in particular, the subsystem deployed on the top of the detector (Top CRT) which I built, installed and commissioned. The Top CRT alone intercepts $\sim 80\%$ of the incoming cosmics and it is composed of 123 hodoscope modules built at the INFN Frascati National Laboratory. The modules were moved to Fermilab and their installation on top of the ICARUS detector was completed at the end of 2021. In the first months of 2022 they were commissioned and fully integrated in the data acquisition system. ICARUS completed its commissioning phase in June 2022, setting the start of the first physics run on both BNB and NuMI beams.

In this work the first cosmic background rejection and event selection tools using the CRT system are presented. By exploiting only the nanosecond scale precision of the CRT and photo-detection system timing synchronization, it is possible to determine whether or not a specific event was likely triggered by a cosmic particle entering the TPC. Additionally, the selection of not fully contained ν_μ CC-like candidates can be achieved by requiring positive difference between the CRT hit and the optical flash timestamps. It was observed that, by requiring that optical flashes are not matched with any CRT hit, a selection of fully contained neutrino interactions can be performed ahead of the full event reconstruction. The pre-selection capability amounts to $\sim$ 32 (39)% of the whole *in time* collected sample for BNB (NuMI). Overall it is expected that, considering the Top CRT alone, a conservative rejection of more than 65% of the *in time* and *out of time* cosmic background can be achieved.

Chapter 1

Beyond the Standard Model

1.1 Neutrinos

Neutrinos were proposed in 1930 by W. Pauli to provide an answer to the continuous spectrum of β-decays[1]. Their first detection only happened in 1956 at the Savannah River Plant in South Carolina (Reines received the Nobel Prize in 1995)[2]. In the following years, neutrinos have been thoroughly studied and tested, the results have always delivered important insights, unveiling peculiar properties that significantly set neutrinos apart from the rest of the known particles. It was observed that neutrinos are always polarized in certain direction with respect to their motion, in particular they could only be left-handed (neutrinos) or right-handed (antineutrinos) [3, 4]. It was, then, proposed that neutrinos can be described by a left-handed Weyl spinor and this was first included in the V-A theory of weak interactions and ultimately in the Standard Model (SM) of particle physics [5, 6, 7, 8, 9].

Following the discovery of the muon, it was theorized that in analogy with their lighter counterpart (electrons) also these new particles would enter Fermi interactions coupled by a neutrino. In 1962 Lederman, Schwartz, and Steinberger created the first accelerator neutrino beam from the pion decays of a proton beam colliding with a target. It was observed that the neutrinos produced by the pion decays associated with a muon would not produce electrons when interacting with matter [10]. This was proof a that electron and muon neutrinos were distinct particles with similar properties that would participate separately in weak interactions with their charged leptonic counterpart. This result was rewarded with the Nobel prize in 1988. The neutrino family was enlarged in 2000 by the discovery of an additional type of neutrinos associated with the tau lepton by the DONUT experiment[11].

In 1957 B. Pontecorvo proposed the first idea of $\nu \iff \overline{\nu}$ oscillations in analogy with $K^0 \iff \overline{K}^0$[12]; following the discovery of a second type of neutrino, in 1969 he generalized his proposal to the two flavour

mixing (ν_μ and ν_e)[13]. This concept was embraced by Maki, Nakagawa, and Sakata, who introduced the concept of mixing between mass and flavor eigenstates [14]. The first hint of solar neutrino oscillations were observed by the Homestake experiment in the 60's, but the definitive answer was provided in 2001 by the SNO experiment[15, 16, 17]. In SNO two different neutrino interaction channels were exploited: the charged current (CC) interaction $\nu_e + d \rightarrow p + p + e^-$ and the neutral current (NC) interaction $\nu_\alpha + d \rightarrow p + n + \nu_\alpha$, with $\alpha = e, \mu, \tau$. While CC interactions depend on the ability to observe the charged lepton associated with the neutrino, the NC ones are indistinguishably sensitive to all flavors. By comparing the fluxes ν_e and ν_α, the SNO experiment demonstrated that the ν_e content of the total solar neutrino flux is only one third, while the total flux prediction (ν_α) was in good agreement with the theoretical predictions[17].

Neutrino oscillations were also observed in atmospheric neutrinos, produced by cosmic-ray interactions in the atmosphere, producing pions and kaons and consequently muon and electron neutrinos. In 1998, the Super-Kamiokande experiment observed a deficit in the up-going muon neutrinos and discovered that their depletion is dependent on L/E, where L is the oscillation length and E is the neutrino energy[18]. The observed deficit was due to the oscillation of the muon neutrinos in tau neutrinos, which could not be detected by the experiment. The Super-Kamiokande results were the definitive proof of neutrino oscillations which led, in 2015, to the Nobel Prize to T. Kajita (for the Super-Kamiokande collaboration) and A. B. McDonald (for the SNO collaboration) for "*for the discovery of neutrino oscillations, which shows that neutrino have a mass*".

The discovery of neutrino oscillations opened a new chapter in particle physics: they imply that the Standard Model is not complete, since in the SM neutrinos are massless.

1.2 Neutrinos in the Standard Model

The Standard Model is based on the gauge symmetry $SU(3) \times SU(2)_L \times U(1)_Y$ and all the known fermions are classified by the corresponding quantum numbers. The representation of the SM fermionic content is given in Table 1.1.

In the SM neutrinos are singlets of $SU(3)$, but they are $SU(2)_L$ doublets with their corresponding charged leptons. Their hypercharge (Y) is $-1/2$ and they do not carry electric charge ($Q = 0$). In the SM, neutrinos are Weyl fermions with left chirality only, $\nu_{\alpha L} \equiv P_L \nu_\alpha$, $\alpha = e, \mu, \tau$. As required by CPT (charge conjugation, parity, and time-reversal) invariance, left-handed neutrinos are accompanied by right-handed antineutrinos. In the SM there are no right-handed neutrinos; therefore, the parity is maximally violated.

Neutrinos interactions are mediated by the weak force according to the

Particles	$SU(3)$	$SU2_L$	$U(1)_Y$
Leptons			
$\begin{pmatrix}\nu_e\\ e\end{pmatrix}_L, \begin{pmatrix}\nu_\mu\\ \mu\end{pmatrix}_L, \begin{pmatrix}\nu_\tau\\ \tau\end{pmatrix}_L$	**1**	**2**	-1/2
e_R, μ_R, τ_R	**1**	**1**	-1
Quarks			
$\begin{pmatrix}u\\ d\end{pmatrix}_L, \begin{pmatrix}c\\ s\end{pmatrix}_L, \begin{pmatrix}t\\ b\end{pmatrix}_L$	**3**	**2**	1/6
u_R, c_R, t_R	**3**	**1**	2/3
d_R, s_R, b_R	**3**	**1**	-1/3

Table 1.1: Representation of the SM fermionic content subdivided with respect to the groups $SU(3)$, $SU(2)_L$ and $U(1)_Y$.

charged current and neutral current terms in the SM Lagrangian:

$$\mathcal{L}_{SM} = -\frac{g}{\sqrt{2}} \sum_{\alpha=e,\mu,\tau} \overline{\nu}_{\alpha L} \gamma^\mu \ell_{\alpha L} W_\mu - \frac{g}{2\cos\theta_W} \sum_{\alpha=e,\mu,\tau} \overline{\nu}_{\alpha L} \gamma^\mu \nu_{\alpha L} Z_\mu + h.c. \tag{1.1}$$

where g is the $SU(2)_L$ coupling and θ_W is the Weinberg angle.

In the SM, neutrinos are subdivided into three families, the existence of additional active neutrinos is not allowed, and it is strongly constrained by the invisible width of the Z boson, $Z \to \nu_\alpha \overline{\nu}_\alpha$. The Z invisible width was measured by the LEP experiment, and it strongly constrains the number of active neutrinos to 3 families[19]:

$$N_\nu = \frac{\Gamma_{inv}}{\Gamma_{\nu\overline{\nu}}} = 2.984 \pm 0.008 \tag{1.2}$$

Additional neutrinos can exist, but they cannot participate in SM interactions; therefore, they are called sterile neutrinos.

1.3 PMNS matrix

Due to the massive nature of neutrinos, they can be described using two different bases: the flavor basis ν_α, $\alpha = e, \mu, \tau$, in which each neutrino flavor is defined by the charged lepton to which it couples, and the mass basis ν_i,

$i = 1, 2, 3$, in which each neutrino has a definite mass. The two different basis are related by a unitary matrix U, the so-called Pontecorvo-Maki-Nakagawa-Sakata (PMNS) matrix:

$$\nu_{\alpha L} = \sum_{i=1}^{3} U_{\alpha i} \nu_L \tag{1.3}$$

Taking into account only the charged current part of equation 1.1, in the basis in which the charged lepton mass matrix is diagonal, the Lagrangian becomes:

$$\mathcal{L}_{SM} = -\frac{g}{\sqrt{2}} \sum_{\alpha,i} \overline{\nu_i} U^{\star}_{\alpha i} \gamma^{\mu} P_L \ell_a \alpha W_{\mu} + h.c. \tag{1.4}$$

with $\alpha = e, \mu, \tau$ and $i = 1, 2, 3$.

The PMNS matrix can be parameterized as [20, 21]:

$$U_{\alpha i} = \begin{pmatrix} c_{12}c_{13} & s_{12}c_{13} & s_{13}e^{-i\delta} \\ -s_{12}c_{23} - c_{12}s_{23}e^{i\delta} & c_{12}c_{23} - s_{12}s_{23}s_{13}e^{i\delta} & s_{23}c_{13} \\ s_{12}s_{23} - c_{12}c_{23}s_{13}e^{i\delta} & -c_{12}s_{23} - s_{12}c_{23}s_{13}e^{i\delta} & c_{23}c_{13} \end{pmatrix} \cdot \mathcal{P} \tag{1.5}$$

where $c_{ij} \equiv \cos\theta_{ij}$ and $s_{ij} \equiv \sin\theta_{ij}$, with $\theta_{ij} \in [0.90°]$. δ is the Dirac Charge Parity Violating (CPV) phase ($\delta \in [0, 360°]$) and $\mathcal{P} \equiv$diag(1,$e^{i\frac{\alpha_{21}}{2}}$, $e^{i\frac{\alpha_{31}}{2}}$), where α_{21} and α_{31} are the two Majorana CPV phases.

The entries of the PMNS matrix have been constrained by the results of several neutrino oscillation experiments. The latest results, within three sigma uncertainties, are the following.

$$|U_{PMNS}|_{3\sigma} = \begin{pmatrix} 0.797 - 0.842 & 0.518 - 0.585 & 0.143 - 0.156 \\ 0.233 - 0.495 & 0.448 - 0.679 & 0.639 - 0.738 \\ 0.287 - 0.532 & 0.486 - 0.706 & 0.604 - 0.754 \end{pmatrix} \tag{1.6}$$

1.4 Neutrino masses beyond the Standard Model

The existence of a neutrino mass basis and the confirmation of neutrino oscillations require the SM Lagrangian to be extended to account also for the neutrino mass terms. Depending on the neutrino intrinsic nature (whether or not they are Dirac or Majorana particles), the extensions of the SM should include different terms.

1.4.1 Dirac Masses

The most simple extension to the SM would require adding additional SM gauge singlets called sterile neutrinos (ν_R). In this extension, a new Yukawa coupling emerges:

$$-\mathcal{L}_y = \overline{L} y_n u \cdot \tilde{H} \nu_R + h.c. \tag{1.7}$$

where $L \equiv (\nu_L^T, \ell^T)^T$ is the leptonic doublet and $\tilde{H} = i\sigma_2 H^{\star}$, where H is the Higgs field. Once the neutral component of the Higgs field acquires a

vacuum expectation value $\langle \tilde{H} \rangle = (v_H/\sqrt{2}, 0)^T$, a Dirac mass term can be obtained for the light neutrinos:

$$-\mathcal{L}_{Dirac} = \frac{\nu_H}{\sqrt{2}} \overline{\nu}_L y_\nu \nu_R + h.c. \tag{1.8}$$

The new Yukawa coupling and the resulting Dirac mass conserve the lepton number. Since a Majorana mass term for ν_R is not forbidden by gauge invariance, its absence must require lepton number conservation; therefore, this symmetry needs to be promoted from an accidental symmetry of the SM to a fundamental element of particle interactions.

An estimation for the order of magnitude of the y_ν coupling can be estimated: considering one generation only, if $m_\nu = y_\nu v_H/\sqrt{2}$ is sub-eV, the coupling would be $y_\nu \sim 10^{-12}$. In such a model, there would be no explanation for the great hierarchy of masses between the charged leptons and the neutrinos. Moreover, if this was the case, there would be no reason to expect such a different hierarchy between neutrinos masses and similar mixing in the quark sector.

1.4.2 Majorana masses

Neutrinos are the only candidate among SM fermions to have a Majorana mass term. It would be possible to construct a singlet combination [22]:

$$\mathcal{L}_{M,BSM} = \frac{\lambda}{\Lambda} L^T \cdot \tilde{H}^\star C^\dagger \tilde{H}^\dagger \cdot L + h.c. \tag{1.9}$$

This new operator is called the Weinberg operator, it has 5 dimensions and requires a mass scale Λ in the denominator. The Weinberg operator is the only $D = 5$ operator allowed in the SM, suggesting that there is a new theory at high energy scale Λ, which does not show up at low energies. The Weinberg operator would break the lepton number by two units and lead to a Majorana mass term:

$$\mathcal{L}_{M,BSM} = \frac{\lambda v_H^2}{2\Lambda} \nu_L^T C^\dagger \nu_L + h.c. \tag{1.10}$$

1.4.3 The seesaw mechanism

In analogy with the Fermi theory, the four-fermion interactions could be mediated by the exchange of virtual massive particles at tree level and their mass M would correspond to the scale Λ. Depending on the exchanged particle, three main models have been studied:

- *Type I see-saw* for a fermion singlet;
- *Type II see-saw* for heavy triplet scalars;
- *Type III see-saw* for triplet fermions;

In Figure 1.1 the diagram corresponding to the contribution to the neutrino mass is shown in the three different seesaw scenarios.

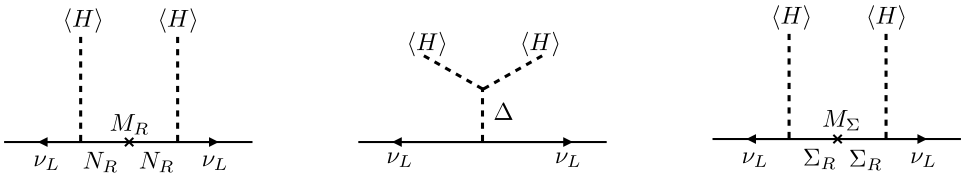

Figure 1.1: Diagrams corresponding to the neutrino mass contribution in the three see-saw scenarios. $\langle H \rangle$ is the vev of the neutral component of the Higgs field, N is a sterile neutrino singlet, Δ is a scalar triplet and Σ is the neutral component of a fermion triplet[23].

Several SM extensions support Λ close to the Grand Unification energy scale, $\sim 10^{14}$ GeV, providing an explanation for the suppression of neutrino masses. Seesaw mechanisms can be included in many GUT theories; this choice is very popular since it would explain the small neutrino mass and the baryon asymmetry of the Universe at the same time, but these models could not be tested directly. Another possibility would be considering smaller couplings, in order to lower the Λ energy scale and allow direct testing of the models. The TeV energy scale accessible at LHC allows the possibility to observe the characteristic signatures of new particles, such as scalar and fermion triplets and sterile neutrinos. An example of such a signature, in the case of sterile neutrinos, would be same-sign dileptons with jets without missing energy and lepton-flavor violating signals[24]. Accounting for even smaller couplings, the Λ scale could be lowered even further, suggesting the possibility of heavy neutrinos with GeV, MeV and even eV masses. For MeV-GeV masses, heavy neutrinos would induce peaks in the spectrum of electrons and muons emitted in meson decays, this signatures are model independent and are currently studied by several experiments, with the most recent constraints provided by the NA62 experiment[25]. In the keV range, the heavy sterile neutrinos could be emitted in beta decays, distorting the electron spectrum with kinks, and, for very small mixing angles, they could be stable on cosmological timescales, providing a candidate for dark matter[26]. For eV masses, the most interesting energy scale for neutrino oscillation experiments, they would introduce neutrino oscillations at short distances. In Figure 1.2, the values of the Yukawa couplings required to generate a light neutrino mass m_ν are reported for a simplified one-generation case. The mixing angle between the heavy neutrino and the active one is $\sin^2\theta = m_\nu / M_N$.

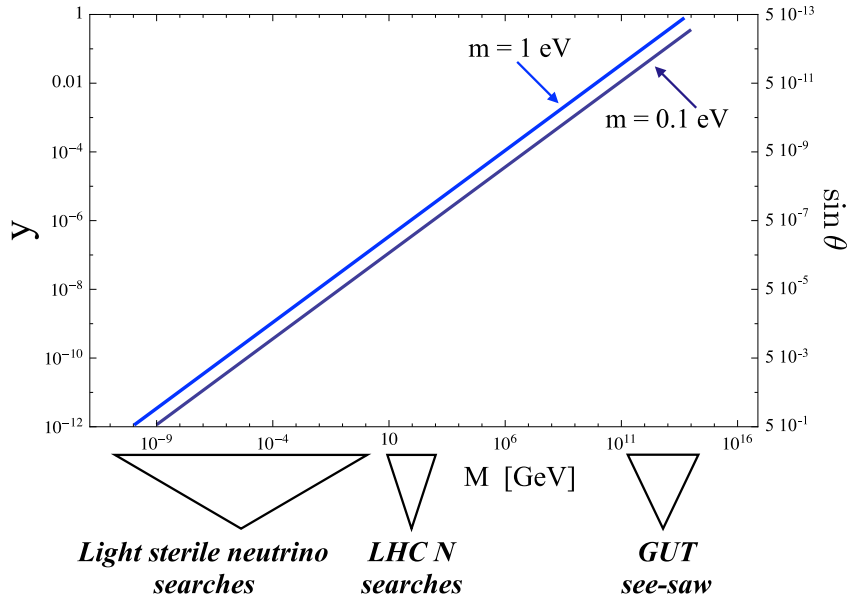

Figure 1.2: Yukawa coupling and the corresponding sterile neutrino mass needed to generate a light neutrino with mass ~ 0.1 eV. The corresponding value of $\sin\theta$ is reported. Different experimental strategies to observe sterile neutrinos in the different energy ranges are also shown[23].

1.5 Experimental neutrino anomalies

Neutrinos have been thoroughly studied in the past decades; a very diverse and rich program of experimental neutrino measurements clarified several aspects of this phenomenon. Nevertheless, several neutrino "anomalies" have been observed, which cannot be accomodates in the 3-neutrino framework: the *Reactor Neutrino Anomaly*, the *Gallium Anomaly*, the *LSND Anomaly* and the *MiniBooNE Low-Energy Excess*. Recently, one more anomalous result was observed and included in this list, the *Neutrino-4 Anomaly*.

The common interpretation of neutrino anomalies requires an oscillation frequency of $\Delta m^2 \gtrsim 1$ eV^2, which implies the addition of at least one sterile neutrino to the three-flavor mixing paradigm. This purely oscillatory interpretation is disfavored by several direct and indirect experimental tests and, in recent years, other more complex theoretical interpretation BSM have been proposed.

1.5.1 Reactor Neutrino Anomaly

In all the simplest light sterile neutrino oscillations, assuming one additional neutrino mass state, nonzero $\nu_\mu \to \nu_e$ oscillations imply that both ν_μ and ν_e disappearance must occur at short baselines. In agreement with this

interpretation, several reactor-detector experiments reported measurements of $\overline{\nu}_e$ fluxes at short reactor-detector distances (10-100 m) lower with respect to the prediction. This flux deficit was observed over a broad range of short baselines, and it is referred to as "Reactor Antineutrino Anomaly" (RAA).

Reactor neutrino experiments exploit the $\overline{\nu}_e$ produced by beta decays of neutron-rich fission fragments, generated by the fissionable isotopes ^{235}U, ^{238}U, ^{239}Pu and ^{241}Pu. These MeV-scale $\overline{\nu}_e$ are emitted isotropically from the reactor core. A typical reactor antineutrino source is very difficult to model due to the hundreds of fission isotopes with different yields. Reactor neutrino experiments have typically used Inverse Beta Decay (IBD), $\overline{\nu}_e + p \rightarrow e^+ + n$ as the desired detection process due to the high cross section and the substantial background rejection capability, which can be obtained by requiring prompt positron energy deposition followed by a delayed and spatially-correlated capture of the thermalized neutron. The $\overline{\nu}_e$ spectrum as a function of energy $E_{\overline{\nu}_e}$ measured by a detector using the IBD process is:

$$\frac{dN}{dE_{\overline{\nu}_e}}(E_{\overline{\nu}_e}) = \frac{1}{4\pi L^2}\epsilon N_p \sigma_{E_{\overline{\nu}_e}} \sum_i \frac{dS_i(E_{\overline{\nu}_e})}{dE_{\overline{\nu}_e}} \tag{1.11}$$

where L is the mean detector distance from the reactor, ϵ is the efficiency, N_p is the number of target protons, $\sigma_{E_{\overline{\nu}_e}}$ is the IBD cross section and $dS_i(E_{\overline{\nu}_e})$ is the antineutrino flux from isotope i. The event rate measured in reactor antineutrino experiments can be expressed in terms of "cross section per fission" $\sigma_{f,a}$, also called "IBD yield":

$$\sigma_f = \sum_i f_i \sigma_i \tag{1.12}$$

where σ_i is the IBD yield for the fissionable product. The IBD yields have been measured in a broad array of antinuetrino experiments in nearly four decades, with experimental reactor-detector baselines ranging from less then 10 m to more then 1 km.

In 2011, new antineutrino flux calculations, using improved sources modeling, predicted detection rates substantially different from previous estimates, leading to a 5-6% discrepancy between the prediction and the average of existing measurements. Figure 1.3 shows the ratio of measured to predicted IBD yields as a function of the reactor-detector baseline. A potential source for the discrepancy could be a model involving sterile neutrinos mixing with active neutrinos. In this scenario, a portion of the $\overline{\nu_e}$ from the nuclear reactor would oscillate at the $\Delta m^2_{new} \sim 1$ eV^2 frequencies to sterile states that go undetected, leading to a deficit in the measurements. The reactor anomaly does not show L/E signature, which justifies the study of additional theories, including inaccuracies in flux modeling. Recent experimental efforts investigated baseline-dependent $\overline{\nu}_e$ energy spectrum distortions to observe L/E dependence.

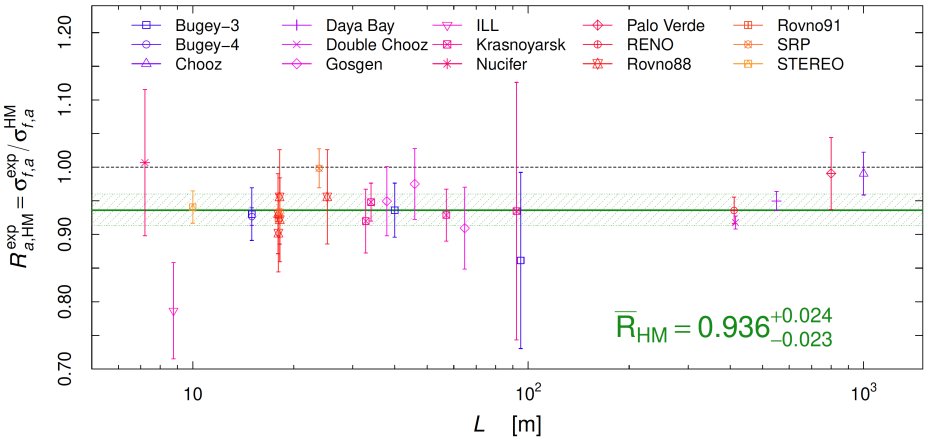

Figure 1.3: Ratio ($R_{a,HM}$) of the measured to the predicted IBD yields as a function of baseline. HM model is used for the predicted IBD yields (Huber and Mueller model). Each data point corresponds to an experiment. The green line and band show the average of $R_{a,HM}$ and average uncertainty respectively[27].

1.5.2 Gallium Anomaly

Electron neutrino disappearance measurements complementary to that of reactors, can be provided by intense radioactive sources, that, for example, were used in radiochemical experiments. Radiochemical experiments were designed to identify solar neutrinos that would interact with the detector chemical converting the element into a radioactive isotope:

$$\nu_e + N(A, Z-1) \rightarrow e^- + N(A, Z)$$

where A and Z are the mass and atomic numbers. Two solar neutrino experiments, GALLEX and SAGE used ^{71}Ga as a detector chemical [28, 29]. The interaction of electron neutrinos would produce electrons and ^{71}Ge isotopes extracted through chemical processes. During the calibration process, artificial ^{51}Cr and ^{37}Ar sources were located inside the detectors, as sketched in Figure 1.4. Electron neutrinos are emitted in the electron capture processes:

$$\begin{aligned} e^- + {}^{51}Cr &\rightarrow {}^{51}V + \nu_e \\ e^- + {}^{37}Ar &\rightarrow {}^{37}Cl + \nu_e \end{aligned} \tag{1.13}$$

with neutrino energies of hundreds of keV. The resulting electron neutrinos would interact with gallium through the reaction:

$$\nu_e + {}^{71}Ga \rightarrow {}^{71}Ge + e^- \tag{1.14}$$

The total number of neutrino produced by the radioactive source and interacting with the detector is determined by the amount of ^{71}Ge collected by

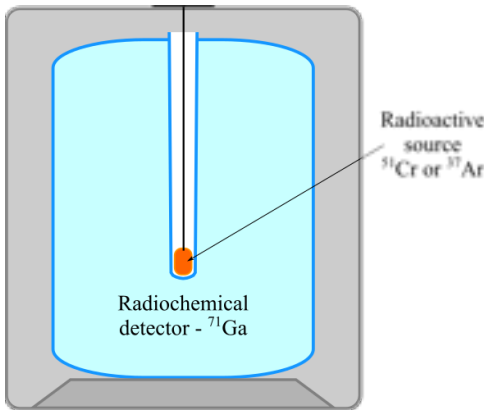

Figure 1.4: Scheme of a gallium based experiment, where the radioactive source (^{36}Ar or ^{51}Cr) is located inside liquid gallium tank[30].

GALLEX	SAGE
0.953±0.11	0.95±0.12
$0.812^{+0.10}_{-0.11}$	$0.791^{+0.084}_{-0.078}$

Table 1.2: Ratio of predicted and observed ^{71}Ge event rates measured by GALLEX (using ^{51}Cr twice) and SAGE (using ^{51}Cr and ^{37}Ar).

chemical extractions. The activity of the source measured by the detector was compared with previous directly measured activity, the ratio between the two is reported in Table 1.2.

The ratio between measured and predicted source activity is referred to as the Gallium Anomaly; in Figure 1.5 the results of Table 1.2 are shown together with the global average $R_{avg} = 0.86 \pm 0.05$, $\sim 3\sigma$ away from unity.

The Gallium Anomaly has been interpreted as the disappearance of electron neutrinos through short-baseline oscillations into sterile neutrinos. In a 3+1 mixing neutrino framework, considering only one sterile neutrino at the eV mass scale, the survival probability of electron (anti)neutrinos is:

$$P(\nu_e \to \nu_e) = 1 - 4|U_{e4}|^2(1 - |U_{e4}|^2)\sin^2(\frac{\Delta m^2_{41} L}{4E}) \qquad (1.15)$$

where L is the distance from source, E is the neutrino energy, U is the 4×4 PMNS mixing matrix and $\Delta m^2_{41} = m^2_4 - m^2_1$ is the squared-mass difference between the heavy sterile neutrino ν_4 and the light neutrino ν_1 (considering $\Delta m^2_{41} \approx \Delta m^2_{42} \approx \Delta m^2_{43}$).

1.5.3 LSND Anomaly

Accelerator experiments with pion decay-at-rest exploit a well-characterized $\overline{\nu}_\mu$ flux with a mean energy of $\sim$ 30 MeV, with negligible $\overline{\nu}_e$ contamination.

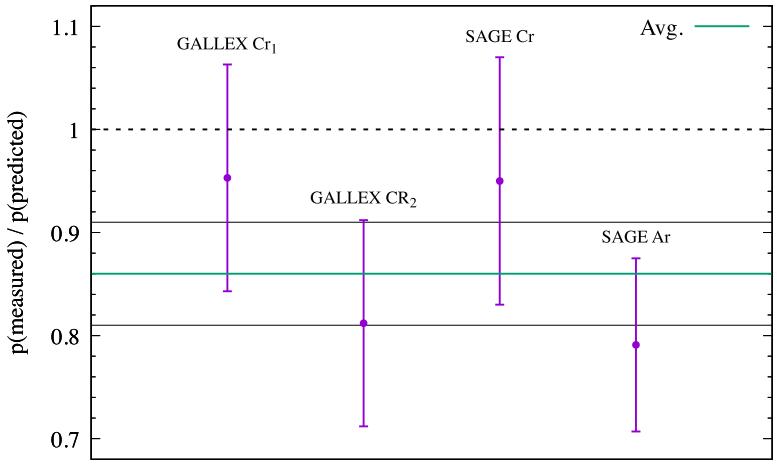

Figure 1.5: Ratio of the observed and predicted event rates as measured by the different radioactive source experiments GALLEX and SAGE. The shadowed region correspond to the 1σ area around the weighted average, $R_{avg} = 0.86 \pm 0.05$[30].

These detectors are located at short distances ($\sim$ 30 m) and they offer good sensitivity to $\overline{\nu}_\mu \rightarrow \overline{\nu}_e$ oscillations. Two of these experiments were Los Alamos Neutrino Detector (LSND) and the KArlsruhe Rutherford Medium Energy Neutrino (KARMEN)[31, 32].

The LSND detector at Los Alamos National Laboratory consisted of a cylindrical tank, 8.3 m long and 5.7 m in diameter, located $\sim$ 30 m from the neutrino source. Neutrinos were produced from the decay of charged pion to muons at rest, the charged pions were produced using a 798 MeV protons on target beamline. Muon antineutrinos were produced by a sequence of decays ($\pi^+ \rightarrow \mu^+ + \nu_\mu$ and $\mu^+ \rightarrow e^+ + \nu_e + \overline{\nu}_\mu$). The intrinsic $\overline{\nu}_e$ contamination from the π^- decay chain was highly suppressed and was expected to be 7.8×10^{-4} smaller then the $\overline{\nu}_\mu$ flux. The signal observed was the inverse beta decay $\overline{\nu}_e + p \rightarrow e^+ + n$ through the detection of 2.2 MeV photon from the neutron capture correlated with the identification of a positron. The detector target was 167 tons of mineral oil, doped with liquid scintillators for both the detection of Cherenkov light and scintillation light. The light readout was carried out using 1220 photomultiplier tubes (PMT) uniformly distributed on the inner surface of the tank. The positron energy and direction were obtained by reconstructing the Cherenkov ring.

LSND observed evidence for $\overline{\nu}_\mu \rightarrow \overline{\nu}_e$ oscillations that could be described by a two-neutrino oscillations with $\Delta m^2 \sim 1$ eV^2 and an oscillation amplitude $\sin^2 2\theta_{\mu e}$ smaller than 1%[33]. The anomaly corresponded to a background-subtracted excess of 87.9 ± 22.4 (stat) ± 6.0 (sys) events. The distributions of the observed excess are presented in Figure 1.6, both as functions of the L/E parameter and the positron energy for a clean sample of

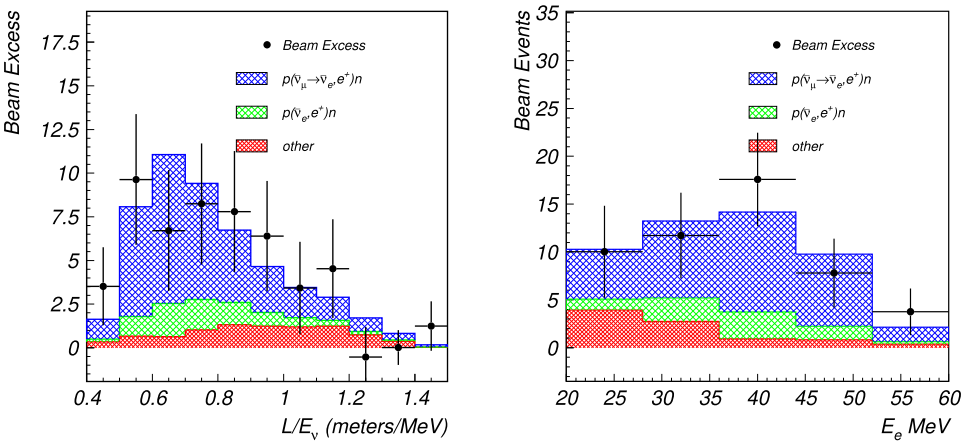

Figure 1.6: The LSND anomaly excess as a function of L/E_ν (left) and the observable positron energy (right). The blue shaded region corresponds to best fit values for two-neutrino oscillations $\sin^2 2\theta = 0.003$ and $\Delta m^2 = 1.2$ eV^2[33].

oscillation candidates.

The $3+1$ sterile neutrino fit was not performed simply in the reconstructed neutrino energy, but as a likelihood in four-dimensional E_e (electron energy), R_γ (coincidence variable), z (electron distance along the tank axis) and $\cos\theta$ (electron angle with respect to the neutrino beam) space. The best fit corresponded to an oscillation amplitude of $\sin^2 2\theta_{\mu e} = 0.003$ and a $\Delta m^2 = 1.2$ eV^2. The resulting allowed region in the parameter space are shown in Figure 1.7, alongside with other experiments that did not see a similar signal.

1.5.4 MiniBooNE Low Energy Excess

The LSND anomaly was investigated with a follow-up experiment. The new experiment needed to rely on different systematics and methodology, while preserving the sensitivity to the same Δm^2 and $\sin^2 2\theta_{\mu e}$. Differently from LSND, which studied neutrino produced by π^+ decaying-in-rest, the new experiment would exploit a π^+ decay-in-flight accelerator beam, which could produce a ν_μ-dominated flux with higher mean energy, granting the opportunity for an independent test at a longer baseline. Following this concept, a muon neutrino beamline was realized at the Fermi National Accelerator Laboratory (FNAL, or Fermilab) from protons extracted from the Booster accelerator. The Booster Neutrino Beamline (BNB) provided a $\sim$ 99.5%-pure muon neutrino beam with a mean energy of $\sim$600 MeV[34]. The test of the LSND anomaly along the BNB was performed with the MiniBooNE Cherenkov detector[35]. MiniBooNE and BNB at Fermilab were designed to provide an L/E ratio comparable to that of LSND ($L/E \approx 0.4-1.0$ m/MeV),

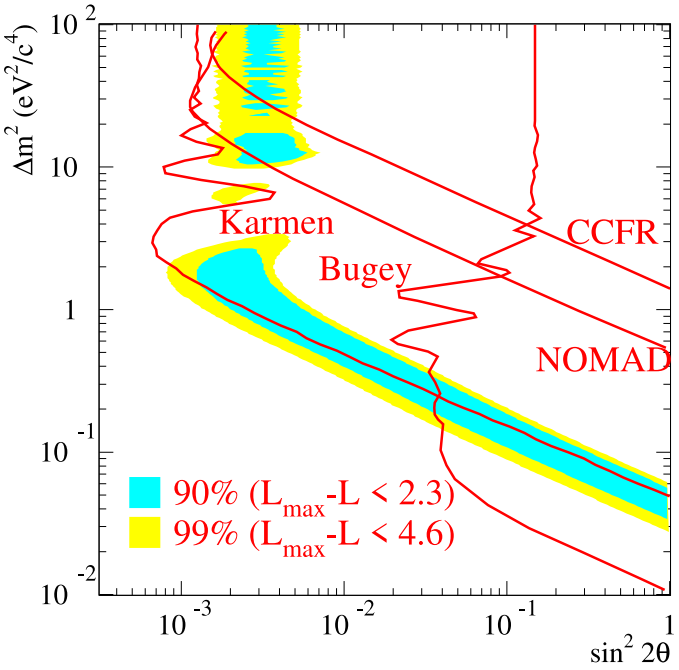

Figure 1.7: Two-neutrino oscillation fit results obtained by the LSND collaboration for events with reconstructed positron energy $20 < E_e < 200$ MeV, with 90% and 99% confidence levels for the allowed regions for $\sin^2 2\theta_{\mu e}$ and Δm^2. The 90% CL limits from other experiments are also shown[33].

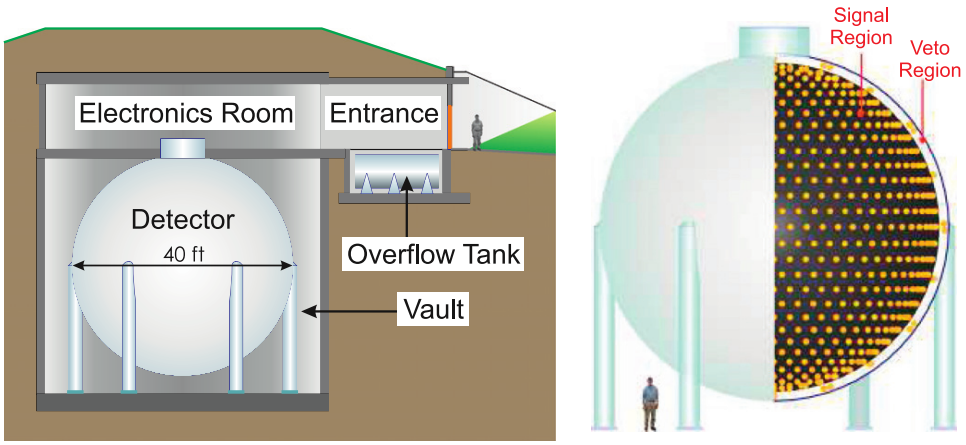

Figure 1.8: Schematic representation of the MiniBooNE Cherenkov detector.

but on a longer baseline (540 m from the neutrino source) and at a higher energy (peak energy of ∼700 MeV). The MiniBooNE experiment consisted of a single spherical tank, 12.2 m in diameter, filled with 818 tons of mineral oil. The inner surface of the detector was covered with 1520 PMTs. Cherenkov and scintillation light generated in the neutrino interactions were used to perform electron and muon identification, to distinguish ν_e and ν_μ interactions. A schematic representation of the MiniBooNE detector is reported in Figure 1.8.

The event reconstruction method in MiniBooNE uses the Cherenkov rings detected on the inner surface of the detector to differentiate electrons, muons and pions, while protons with kinetic energies smaller than the Cherenkov threshold in mineral oil (∼ 350 MeV kinetic energy) could not be observed. One of the main limitations of MineBooNE (and Cherenkov detector in general) was that the topology of the interactions was not directly reconstructed and single photons, for example, were indistinguishable from single electrons in terms of their Cherenkov ring reconstructions. The separation of neutral-current (NC) $\pi^0 \to \gamma\gamma$ events relied on the reconstruction of two separate Cherenkov rings. MiniBooNE main sources of background searching for ν_e from $\nu_\mu \to \nu_e$ oscillations were:

- intrinsinc ν_e contamination in BNB, $\mathcal{O}(0.5\%)$ ν_e and $\overline{\nu}_e$ that were an irreducible background;
- NC π^0 events, where one of the photons was not reconstructed and the event is indistinguishable from single electron, for example when the Cherenkov cones are overlapping;
- NC $\Delta \to N\gamma$ where gammas produced during the radiative decay of Δ baryon could mimic a single-electron production in MiniBooNE;
- "dirt" events, corresponding to neutrino-induced events in the material surrounding the detector, with some particles scattering in the active region of the inner volume.

A graphical representation of the signatures of CCQE ν_μ, CCQE ν_e, and NC π^0 inside the MiniBooNE detector is presented in Figure 1.9.

The first results from MiniBooNE in 2007, corresponding to a third of the total data set collected (5.58×10^{20} protons on target, POT), reported no evidence of neutrino oscillation within a $\nu_\mu \to \nu_e$ appearance paradigm, placing a 90% CL limit covering the majority of the allowed LSND parameter space. The first analysis was performed only for the region of reconstructed neutrino energy > 475 MeV, assuming quasi-elastic scattering. Although no excess was found for $E_\nu^{QE} > 475$ MeV, an excess was observed below this limit. This excess is referred to as the MiniBooNE "Low-Energy Excess" (or LEE), and consisted of $128.8 \pm 20.4 \pm 38.3$ excess events above the predicted backgrounds, corresponding to 3.0σ at energies < 475 MeV.

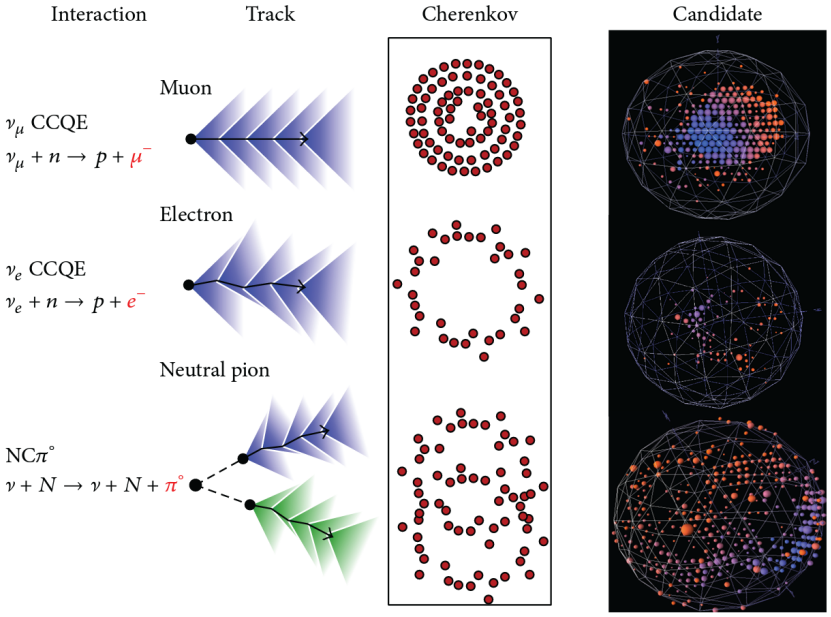

Figure 1.9: Graphical representation of ν_μ, ν_e and NCπ^0 signatures in the MiniBooNE detector.

Exploiting the BNB capabilities of switching from neutrino to antineutrino mode, by inverting the focusing horns magnetic field polarity, MiniBooNE repeated its search running in antineutrino mode, acquiring 5.66×10^{20} POT. The results from MiniBooNE's first $\overline{\nu}_\mu \rightarrow \overline{\nu}_e$ search showed an excess extending both at low energy and in the oscillation signal region of $475 < E_\nu^{QE} < 300$ MeV. Expanding the fit to the whole energy region($E_\nu^{QE} > 200$ MeV), the best fit was found at $\Delta m^2 = 4.42$ eV^2 and $\sin^2 2\theta = 0.0066$, with a significant overlap in the low Δm^2 allowed region of the LSND's 90% CL.

MiniBooNE ran for ten additional years, collecting 18.75×10^{20} POT in neutrino mode and 11.27×10^{20} POT in antineutrino mode. MiniBooNE's final results are reported in Figure 1.10 showing an excess of data over background prediction for both the beam modes. The excess is more visible below 600 MeV with an overall significance of 4.8σ, combining both beam modes. The observed excess was 560 ± 119.6 and 77.4 ± 28.5 events for neutrino mode and the antineutrino mode, respectively. The final best fit parameters for the two complete data samples, over the entire energy range ($200 < E_\nu^{QE} < 3000$ MeV), are $\Delta m^2 = 0.043 eV^2$ and $\sin^2 2\theta = 0.807$. MiniBooNE's best-fit close to maximal mixing is ruled out by several experiments and, as it can be seen in Figure 1.11, none of the allowed LSND region at $\Delta m^2 > 10$ eV^2 is within the combined MiniBooNE 95% CL.

Although the overall number of excess events is consistent with what is expected by the LSND's best-fit parameters, the predicted signal from

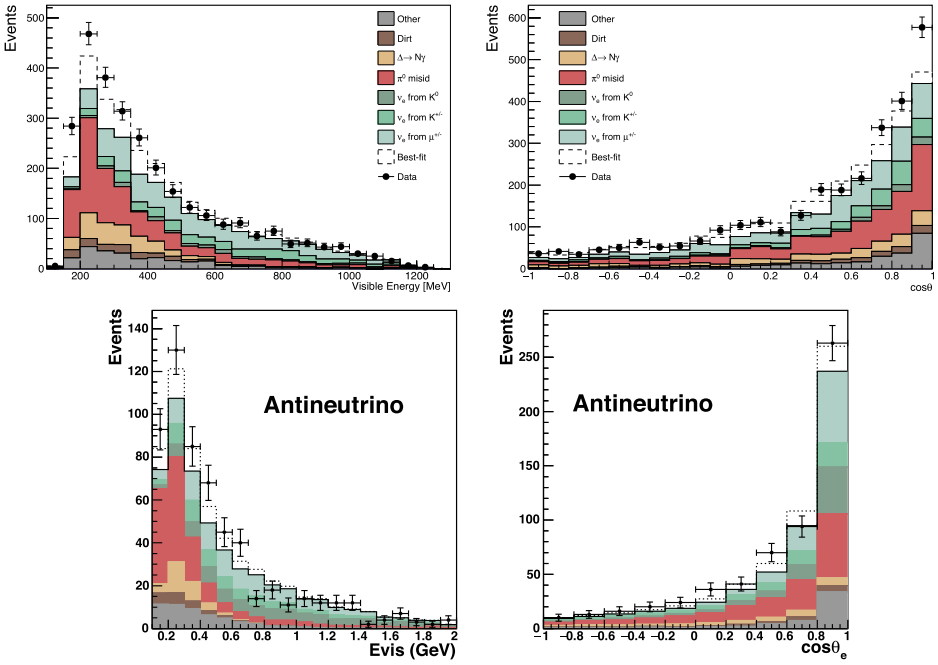

Figure 1.10: Final MiniBooNE results corresponding to 18.75×10^{20} POT in neutrino mode (top figures) and 11.27×10^{20} POT in antineutrino mode (bottom figures), for both the reconstructed visible energy (left) and the reconstructed Cherenkov cone angle with respect to the neutrino beam (right)[36, 37].

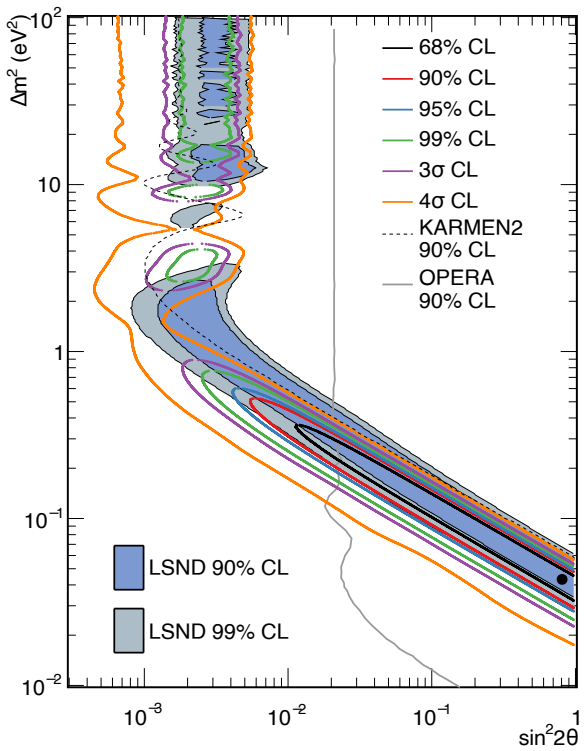

Figure 1.11: Final MiniBooNE allowed regions fit for the full fit of neutrino and antineutrino modes[37].

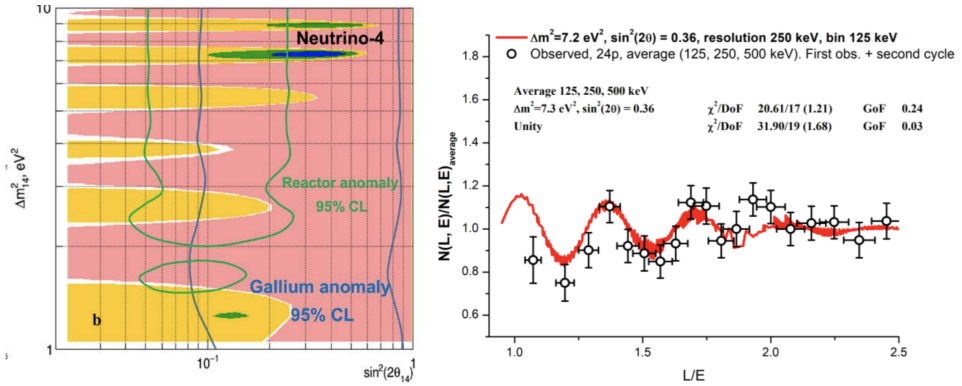

Figure 1.12: Left: 1σ (blue), 2σ (green) and 3σ (yellow) regions suggested from the Neutrino-4 sterile neutrino search. Right: L/E distribution of background (reactor off) subtracted IBD rates reported by the Neutrino-4 collaboration[39].

$\nu_\mu \rightarrow \nu_e$ oscillations, corresponding to MiniBooNE's two-neutrino best-fit, cannot describe the shape of the excess (see Figure 1.10). This difference motivated additional interpretations of the excess, considering energy misreconstruction, a not comprehensive estimation of the backgrounds and, possiblyy, other BSM physics as the source of the MiniBooNE LEE.

1.5.5 Neutrino-4 Anomaly

Neutrino-4 is a 1.8 m^3 Gd-doped liquid scintillator detector. It is divided into 10 rows, each consisting of 5 sections of 0.225 m $\times$ 0.225 m $\times$ 0.95 m. The detector is located in Dimitrovgrad (Russia) and detects $\overline{\nu}_e$ from the 57 MW$_{thorium}$ SN-3 reactor. A movable platform allows the detector to sample neutrinos at different distances, from 6 to 12 m. The short reactor power on (off) cycles of 8-10 (2-5) days allow for rapid signal and background measurements[38].

Neutrino-4 collected data from 2016 to 2021 with a rate of $\sim$300 events/day, corresponding to 720 (860) days of reactor on (off) data with a signal-to-background ratio of $\sim$0.5. The experiment performed a sterile neutrino search in the L/E parameter space and observed evidence with 2.9σ of neutrino oscillation effect with the best fit at $\Delta m^2_{14} = 7.3 \pm 0.13(\text{stat}) \pm 1.16(\text{syst})$ and $\sin^2\theta_{14} = 0.36 \pm 0.12(\text{stat})$. The results of the oscillation best-fit are presented in Figure 1.12, as well as a plot of the L/E oscillatory pattern observed after subtraction of the reactor off background[39].

It is worth noting that the Neutrino-4 results are widely debated by several collaborations; on top of this, the Neutrino-4 suggested parameter space is disfavored by the PROSPECT (Precision Reactor Oscillation and SPECTrum) and STEREO experiments.

1.6 Short Baseline sterile Neutrino Global Fit

All the anomalies described in section 1.6 can be explained by introducing one (or more) additional sterile neutrino states with masses $\mathcal{O}(1-10)$ eV. In the simplest 3+1 model, one additional neutrino flavor ν_s, not participating in the weak interactions, is added to the standard neutrinos. The three active neutrino flavors and the sterile neutrino, accounting for an extended PMNS matrix, would be mixtures of four different neutrino mass eigenstates, where m_4 is assumed to be of order $\sim$1 eV. The extended 4×4 oscillation matrix $U_{\alpha i}$, with $\alpha = e, \mu, \tau, s$ and $i = 1, 2, 3, 4$, would then describe the neutrino oscillation in the 3+1 model.

Assuming that the fourth m_4 is mostly sterile and much heavier then the other three mass eignestates, $\Delta m^2_{41} \gg |\Delta m^2_{31}|, \Delta m^2_{21}$, therefore Δm^2_{31} and Δm^2_{21} can be approximated as degenerate and null. In the limits where Δm^2_{31} and Δm^2_{21} oscillations are negligible, short baseline oscillations can be approximated by:

- *electron neutrino disappearance channel*:

$$P(\nu_e \to \nu_e) \cong 1-4|U_{e4}|^2(1-|U_{e4}|^2)\sin^2(\frac{\Delta m^2_{41}L}{4E_\nu}) \equiv 1-\sin^2(2\theta_{ee}\sin^2(\frac{\Delta m^2_{41}L}{4E_\nu}) \tag{1.16}$$

- *muon neutrino disappearance channel*:

$$P(\nu_\mu \to \nu_\mu) \cong 1-4|U_{\mu4}|^2(1-|U_{\mu4}|^2)\sin^2(\frac{\Delta m^2_{41}L}{4E_\nu}) \equiv 1-\sin^2(2\theta_{\mu\mu}\sin^2(\frac{\Delta m^2_{41}L}{4E_\nu}) \tag{1.17}$$

- *electron neutrino appearance channel*:

$$P(\nu_\mu \to \nu_e) \cong 4|U_{\mu4}|^2|U_{e4}|^2\sin^2(\frac{\Delta m^2_{41}L}{4E_\nu}) \equiv \sin^2(2\theta_{\mu e})\sin^2(\frac{\Delta m^2_{41}L}{4E_\nu}) \tag{1.18}$$

Short baseline oscillations are relevant for $L/E_\nu \approx 1$ m/MeV or km/GeV if $\Delta m^2_{41} \approx 1$ eV^2. It is important to note, that from equations 1.26, 1.27 and 1.28, if both $|U_{e4}|^2$ and $|U_{\mu4}|^2$ are not zero, electron-neutrino disappearance, muon-neutrino disappearance and muon-to-electron neutrino appearance must all occur at the same L/E_ν. The oscillation amplitudes for the appearance and disappearance channels are related by $\sin^2 2\theta_{\mu e} \leq 1/4 \sin^2 2\theta_{\mu\mu} \sin^2 2\theta_{ee}$.

Although anomalies have been observed and thoroughly studied in ν_e disappearance and $\nu_\mu \to \nu_e$ appearance, the $\nu_\mu/\overline{\nu}_\mu$ disappearance channel never observed anomalies. Strong limits to $\nu_\mu/\overline{\nu}_\mu$ disappearance channels, provided by several neutrino oscillation experiments such as MINOS / MINOS + and IceCube, are presented in Figure 1.13. Experimental data constrain

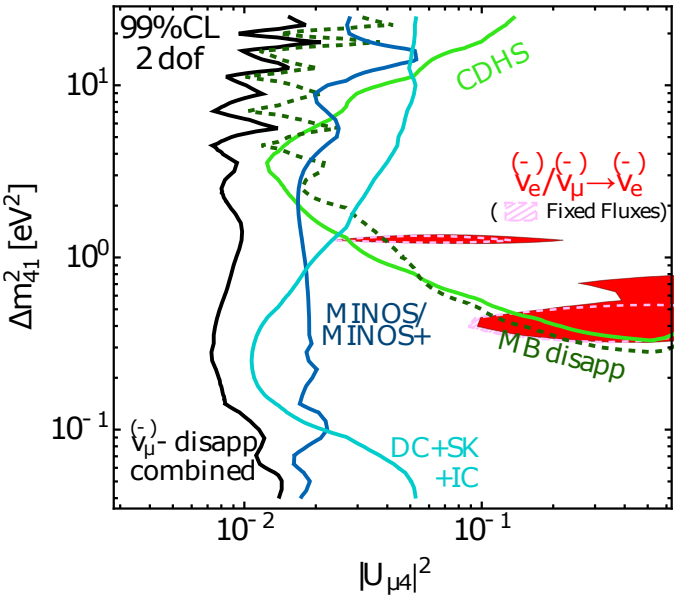

Figure 1.13: Constraints on the 3+1 scenario from $\nu_\mu/\overline{\nu}_\mu$ disappearance. For comparison, in red it is shown the parameter region favoured by ν_e disappearance and $\nu_\mu \to \nu_e$ appearance data[40].

$|U_{\mu 4}|^2 \lesssim 10^{-2}$ across a wide range of Δm^2_{41} from $\sim 2\times 10^{-1}$ eV^2 to ~ 10 eV^2. Atmospheric neutrino data, dominated by IceCube results, provide strong constraints at $\Delta m^2_{41} \lesssim 10^{-2}$. Given the constraints on $|U_{e4}|$ from reactor experiments, the values of $\sin^2 2\theta_{\mu e} \equiv 4|U_{e4}|^2|U_{\mu 4}|^2$, required by LSND and MiniBooNE can only be reached if $|U_{\mu 4}|$ is large. This, however, is clearly disfavoured by multiple $\nu_\mu/\overline{\nu}_\mu$ disappearance null results. This is the origin of a severe 4.7σ tension in the global fits between appearance and disappearance data, reported in Figure 1.14.

A coherent picture that accommodates all of the anomalies is still missing, and several experiments are taking data to provide an answer to them. The Short-Baseline Neutrino (SBN) program at Fermilab exploits the Booster Neutrino Beamline and three detectors located at different distances from the neutrino source. Thanks to the excellent detector capabilities, based on the Liquid Argon Time Projection Chamber (LArTPC) technology, SBN will investigate both the ν_e appearance and the ν_μ disappearance channels simultaneously. With 5 years of data taking, SBN aims to provide a definitive answer to neutrino anomalies by confirming or rejecting at $> 5\sigma$ CL the light sterile neutrino solution.

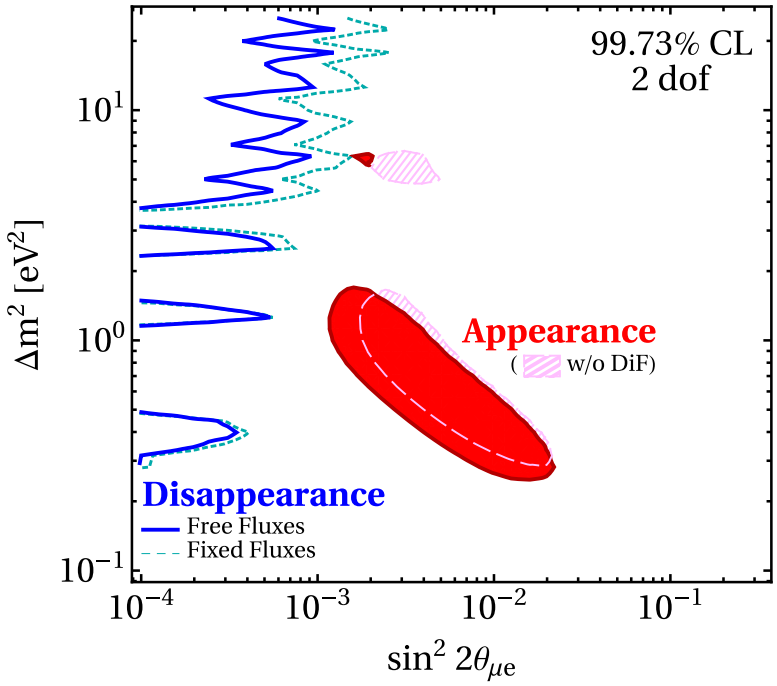

Figure 1.14: Appearance versus disappearance data in the parameter space spanned by the effective mixing angle $\sin^2 2\theta_{\mu e} \equiv 4|U_{e4}|^2|U_{\mu 4}|^2$ and the mass squared difference Δm^2_{41}. The blue curves show limits from the disappearance data sets using free reactor fluxes (solid) or fixed reactor fluxes (dashed), while the shaded contour are based on the appearance data sets using LSND DaR+DiF (red), Decay at Rest + Decay in Flight, and LSND DaR (pink)[40].

Chapter 2

The Short-Baseline Neutrino Program

The *Short-Baseline Neutrino* Program (SBN) will carry out the most sensitive search to address the possible existence of 1 eV mass-scale sterile neutrinos hinted by experimental anomalies. It is based on three LArTPCs (Liquid Argon Time Projection Chambers[41]) detectors located along the *Booster Neutrino Beam* (BNB) line[42].

2.1 SBN

The detectors located at different baselines allow to search for high-Δm^2 neutrino oscillations in the $\nu_\mu \rightarrow \nu_e$ (*Appearance*) and $\nu_\mu \rightarrow \nu_\mu$ (*Disappearance*) channels. Figure 2.1 shows an illustration of the SBN LArTPCs sitting along the Booster Neutrino Beam. The Short-Baseline Near Detector (SBND) has an active mass of 112 t of liquid argon and is located at 110 m from the neutrino source. SBND is currently under construction and it is expected to begin data taking in late 2023. The MicroBooNE detector has an active mass of 89 t of liquid argon and it is located 470 m from the BNB target. MicroBooNE started collecting data in October 2015 and completed its program in 2021 after five years of physics data. The far detector is the ICARUS-T600 detector refurbished and upgraded for optimal performance in SBN. ICARUS is located 600 m from the BNB source and has an active mass of 476 t of liquid argon; the detector is in data collection operation since June 2022. The complementarity of the three LArTPCs will create a world-leading sterile neutrino search program that will cover the parameters allowed by past anomalies at a significance $\geq 5\sigma$.
The SBN physics program goals are:

- understanding the nature of MiniBooNE Low Energy Excess with MicroBooNE (Phase 1);

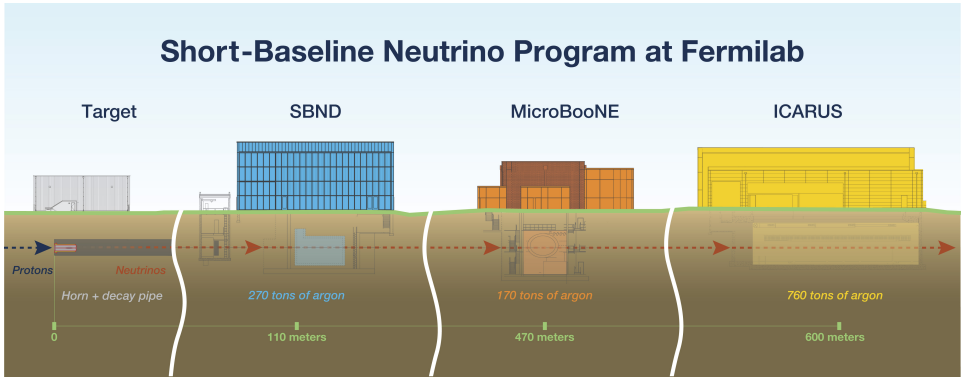

Figure 2.1: Illustration of the three SBN detectors along the Booster Neutrino Beam. The Short-Baseline Near Detector is the closest to the neutrino source, MicrooBooNE, the first to complete its operations sits in the middle, ICARUS, the largest of the three, is the furthest.

- searching for sterile neutrinos both in appearance and disappearance channels, using SBND and ICARUS as near and far detector respectively (Phase 2);
- provide verification or refutation of the Neutrino-4 experiment's evidence for a large mixing angle sterile neutrino;
- paving the ground for the future long-baseline experiment DUNE, by a further development of the LArTPC technology and by high-statistics measurements of ν-Ar cross sections in the few GeV region.

In addition to its primary goals, the SBN Program will perform a rich program of BSM serches, looking for neutrino tridents, Higgs portals for scalar dark matter, heavy leptons, Lorentz and CPT violating effects among others.

The global ν_e appearance data points to a mass splitting (Δm^2_{41}) between 0.3 eV^2 and 1.5 eV^2, with a mixing strength in the range $0.002 \lesssim \sin^2 2\theta_{\mu e} \lesssim 0.015$. Figure 2.2 shows the shape of the oscillation probability for two sets of parameter in these ranges. The projected sensitivities (assuming an exposure of 6.6×10^{20} protons on the BNB target) to the ν_e appearance and ν_e disappearance oscillation signals are shown in Figure 2.3 and 2.4. The BNB will operate until the LBNF (*Long Baseline Neutrino Facility*) long-shutdown expected by early 2027, enabling the joint ICARUS and SBND phase II to collect more then twice the statistic of the SBN proposal, while it is expected that ICARUS alone will acquire more then three times the proposed statistic. The ν_e disappearance channel will be studied by both SBND (BNB) and ICARUS (NuMI), providing a direct probe of $\sin^2 2\theta_{ee}$ using a neutrino beam rather then lower energy reactor antineutrinos. Accounting

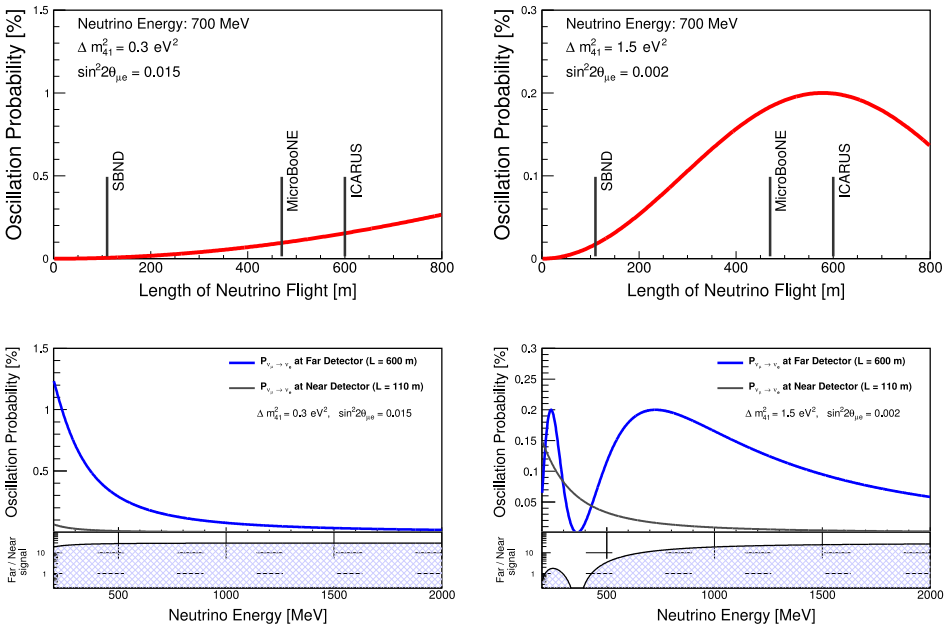

Figure 2.2: Top row: $\nu_\mu \to \nu_e$ oscillation probability for a 700 MeV neutrino as a function of the baseline for two different sets of oscillation parameters. Bottom row: $\nu_\mu \to \nu_e$ oscillation probabilities at the near (110 m) and far (600 m) detector as a function of the neutrino energy, for the same set of parameters. The far/near ratio of appearance probabilities is also shown.[43]

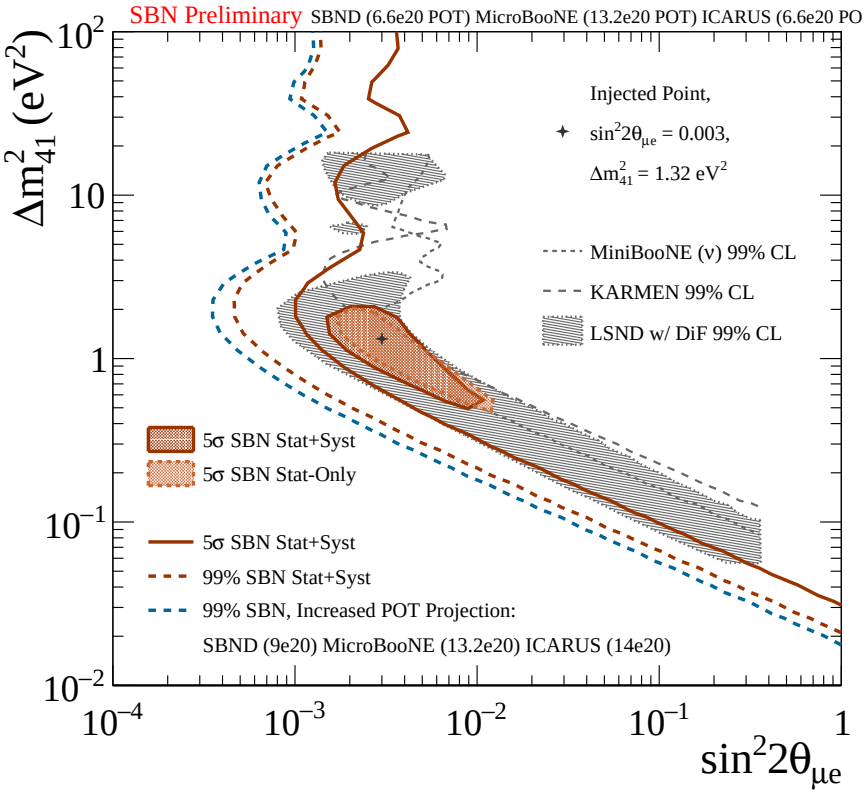

Figure 2.3: SBN 5σ sensitivity to a light sterile neutrino in the appearance channel. For comparison, the LSND preferred region at 99% C.L. (shaded black) is also shown. The SBN sensitivities correspond to an integrated 6.6×10^{20} protons on the BNB target. The sensitivity for the expected POTs is also shown (blue).

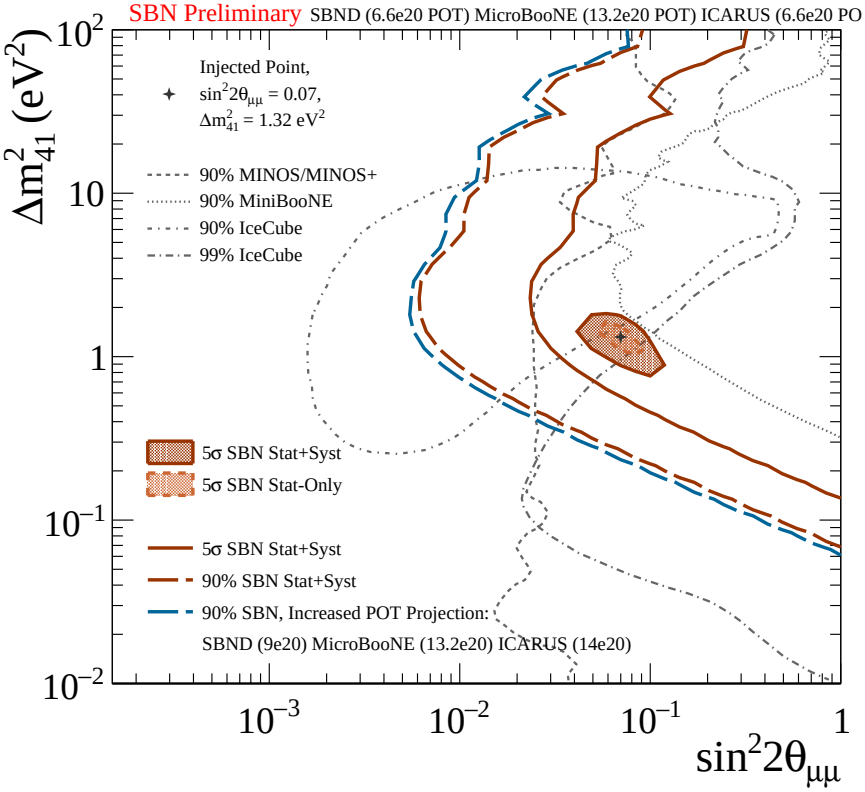

Figure 2.4: SBN 5σ sensitivity to a light sterile neutrino in the disappearance channel. The SBN sensitivities correspond to an integrated 6.6×10^{20} protons on the BNB target. The sensitivity for the expected POTs is also shown (blue).

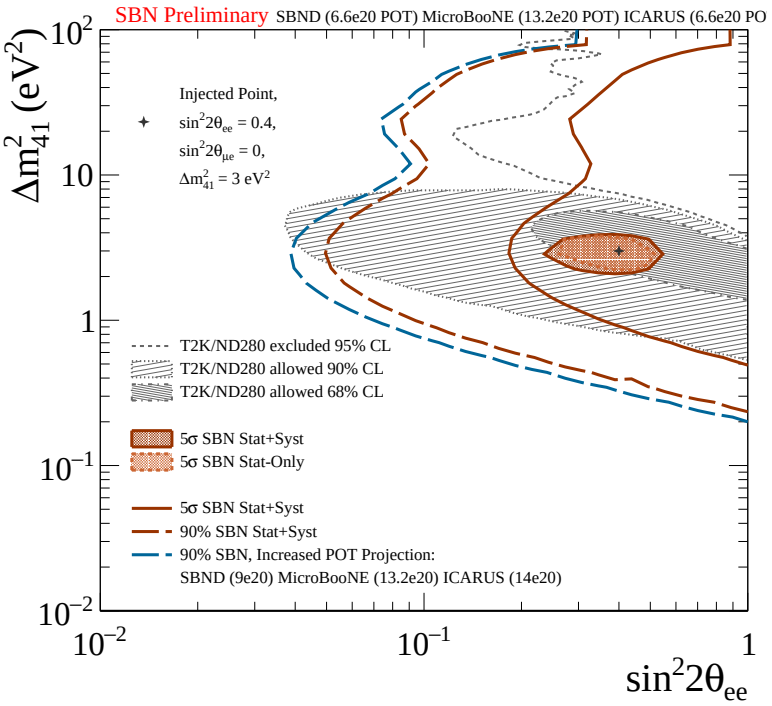

Figure 2.5: SBN 5σ sensitivity to the $\nu_e \rightarrow \nu_e$ disappearance channel for an integrated 6.6×10^{20} protons on the BNB target. The sensitivity for the expected POTs is also shown (blue).

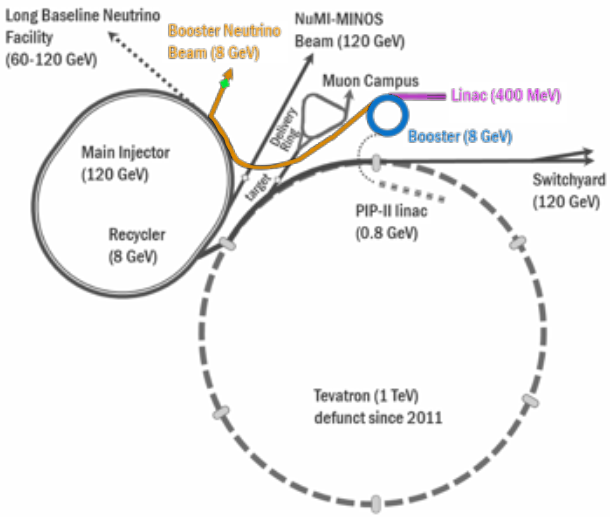

Figure 2.6: Illustration of the Fermilab Accelerator complex. Each component of the BNB production system is highlighted in color. Protons exiting the 400 MeV Linac (purple) are boosted to 8 GeV in the Booster synchroton (blue). 8 GeV protons are extracted from the Booster ring and fired at a beryllium target (green) to produce secondary hadrons which decay, producing the Booster Neutrino Beam.

for 6.6×10^{20} protons on target, SBND will collect $\sim$ 35000 ν_e. ICARUS can leverage its off-axis position along the NuMI beam (6 degrees) and observe a ν_e enriched flux. The SBN sensitivity in the ν_e disappearance channel, considering only BNB events, is shown in Figure 2.5.

2.2 The Booster Neutrino Beam

The BNB is generated by extracting 8 GeV protons from the Booster accelerator (Figure 2.6) and firing them on a 1.7λ beryllium target, to produce a secondary beam of hadrons, mainly pions[44]. Charged secondary particles are focused by a single toroidal aluminum alloy focusing horn that surrounds the target. It is supplied with 174 kA in 143 μs pulses in coincidence with the proton delivery. The magnetic horn focuses or defocuses pions based on their charge in order to steer the maximal amount of same-charge pions into a collimated beam. Focused mesons pass through a collimator and are allowed to propagate in the decay tunnel, a 50 m long, 0.9 m radius air-filled volume. In the decay tunnel, the majority of the charged mesons decay mostly via the dominant channel

$$\pi^{+/-} \rightarrow \mu^{+/-} + \nu_\mu/\overline{\nu}_\mu \tag{2.1}$$

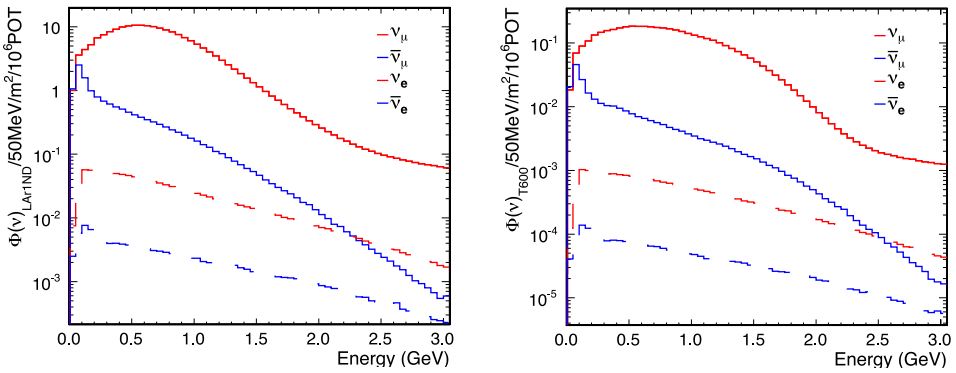

Figure 2.7: ν_μ, $\overline{\nu}_\mu$, ν_e, and $\overline{\nu}_e$ components of the flux distribution for SBND (left), and ICARUS (right) in neutrino mode.

which occurs with a 99.9877% branching ratio. At the end of the decay tunnel, a 25 m concrete and steel plates wall stops residual particles. The Booster spill width is 1.6 μs with $\sim 5{\times}10^{12}$ protons per spill delivered to the beryllium target with an extraction rate of up to 5 Hz. The main Booster RF is operated at 52.8 MHz and the beam is extracted using a fast-rising kicker that steers all the particles in a single turn. The resulting structure is a series of 81 bunches of protons each $\sim$ 2 ns wide and 19 ns apart.

The polarization of the magnetic horn can be reversed, allowing for both forward and reverse horn currents (FHC and RHC) operations. In forward mode, the BNB horn focuses positive mesons to produce a ν_μ dominated beam, whereas in reverse mode, negative mesons are focused to produce an $\overline{\nu}_\mu$ dominated beam. Currently, it is not expected for the BNB to run in reverse mode throughout the Phase 2 of the SBN Program.

Figure 2.7 shows the fluxes of neutrinos observed in the SBND and ICARUS detectors. The flux peaks at around $\sim$ 0.7 GeV. The neutrino beam consists almost entirely of ν_μ (and $\overline{\nu}_\mu$), with only a 0.5% of $\nu_e/\overline{\nu_e}$ component.

2.3 NuMI

The *Neutrinos at the Main Injector* (NuMI) beam is currently the most powerful neutrino beam produced by extracting 120 GeV protons from the Fermilab Main Injector[45]. The protons are first accelerated to 8 GeV in the Booster, as described in section 2.2, and then steered in the Main Injector. The Main Injector is 7 times the circumference of the Booster, which allows the injection and the storage of seven Booster batches, however a maximum of six proton batches can be accelerated as the last slot is used for the pulse kicker rise time. The Main Injector accelerates protons up to 120 GeV. The

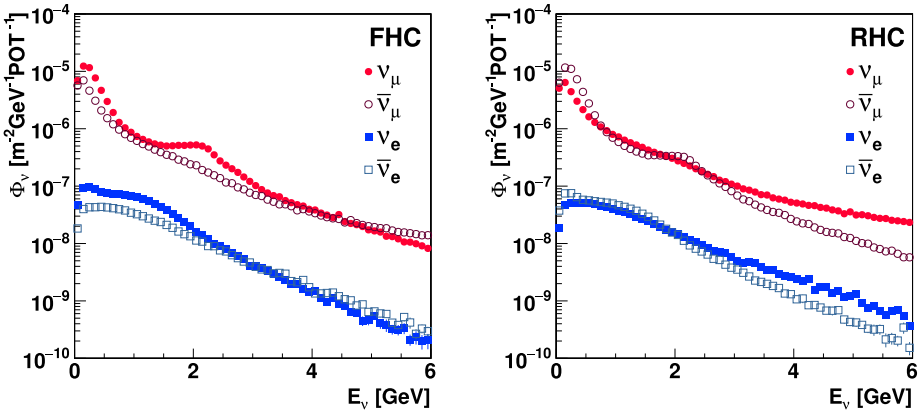

Figure 2.8: NuMI beam flux in ICARUS for forward (*left*) and reverse (*right*) horn current.

protons destined for the NuMI beam line are extracted, bent downward to point at the MINOS Far Detector, and transported to the NuMI target. The protons are fired onto a graphite target and the produced hadrons are focused by two magnetic horns and then enter a 675 m long decay volume. An hadron monitor is located at the end of the decay volume, in front of a 5 m thick absorber, followed by 240 m of rocks, interspersed with 4 muon monitors. The NuMI horns are pulsed with an half-sine wave with a duration of 2.3 ms, producing magnetic fields up to 3 T. The maximum design current is 205 kA with a repetition rate of 1.87 s. The NuMI is able to deliver up to $6.5{\times}10^{13}$ protons per spill with a beam pulse width of 9.6 μs.

Originally, NuMI was built in 2005 to provide neutrinos for the MINOS experiment, later on it was used in other experiments such as MINERνA, ArgoNeuT, NOνA and MINOS+. The ICARUS detector lies 795 m downstream of the NuMI neutrino beam at an off axis angle of 5.7°. The large off axis angles provides a significant flux of both muon and electron neutrinos and antineutrinos in both the neutrino (FHC) and antineutrino (RHC) beam configurations, corresponding to $3{\cdot}10^{20}$ POT/yr. Figure 2.8 shows the expected neutrino flux at the ICARUS detector for FHC (left) and RHC (right) mode.

2.4 The SBN Near Detector: SBND

The Short-Baseline Near Detectr (SBND) has an active LAr mass of 112 t and is located 110 meters from the BNB target. SBND as the near detector of the SBN program will measure the unoscillated BNB neutrino flux. SBND is composed of two TPCs with a drift region of 2 m, for a total volume of 4 m (H) × 4 m (W) × 5 m (L). The drift direction is perpendicular

to the neutrino beam and the maximal drift length corresponds to about 1.3 ms drift time, for the nominal 500 V/cm. The innovative SBND TPC is composed of 2 cathode planes and 4 anode planes (two adjacent anode planes per TPC, APAs). The cathode planes lie side-by-side and are located at the joint region of the two TPCs. The anode planes are located on the opposite wall to the cathode and are adjacent one to the other. Each anode plane is composed of three wire planes angled at $\pm 60°$ and $0°$ to the vertical plane. The wire planes are 3 mm apart with a wire pitch of 3 mm. The wires are 150 μm in diameter and are made of copper-beryllium. Overall, the SBND TPC is composed of 2816 wires. Each of the two jointed cathode planes are composed of metallic subframes supporting a reflective foil coated in TPB wavelength-shifter between them. The TPB covered foil maximises the light yield of the detector by reflecting the scintillation photons to the Photo-Detection System (PDS) on the opposite wall. SBND front-end electronics for the TPC readout is located inside the liquid argon (*cold electronics*), maximizing the signal-to-noise ratio.

The SBND PDS is composed of multiple components and it will be the benchmark for future LArTPC experiments. The PDS is divided into 24 modules, 12 behind each anode plane. Each module is composed of 5 PMTs (4 PTB-coated and 1 uncoated) and 4 X-ARAPUCA pairs. The SBND PDS will allow detection of both direct and indirect scintillation light. The ARAPUCA are novel devices aiming to record scintillation photons by trapping them within a box with highly reflective internal surfaces[46][47]. The vacuum ultraviolet (VUV) LAr scintillation light enters the ARAPUCA box crossing a dichroic filter which is transparent to the entering wavelength, but reflective to the shifted ones. The entering VUV light goes through a WLS embedded slab and the shifted light is collected by Silicon Photo-Multipliers (SiPMs). Figure 2.9 shows a cartoon of the SBND TPC with visible two modules of the PDS.

Being SBND located on ground on average 3 cosmic rays per neutrino event will cross the active volume, in coincidence with the neutrino beam. In order to reject this abundant source of background, SBND is instrumented with a Cosmic Ray Tagger (CRT) system. The CRT is composed of 7 planes, one on each detector face and an additional plane above the top one, creating a telescopic tagging system with a coordinate resolution of < 2 cm.

The SBND detector is currently under construction and Figure 2.10 shows a drawing of the detector lifted out of the cryostat. The external cryostat is completed (Figure 2.11 shows a picture of the cryostat during the construction phase) and, recently, the TPC has been assembled and moved to the near detector building for its installation.

It is expected that the near detector will be ready to be filled with liquid argon by July 2023; the cold commissioning is expected by the end of the year. Due to its proximity to the neutrino source, SBND will be able to collect > 5000 neutrinos events per day. Considering an exposure of $\sim 10^{21}$

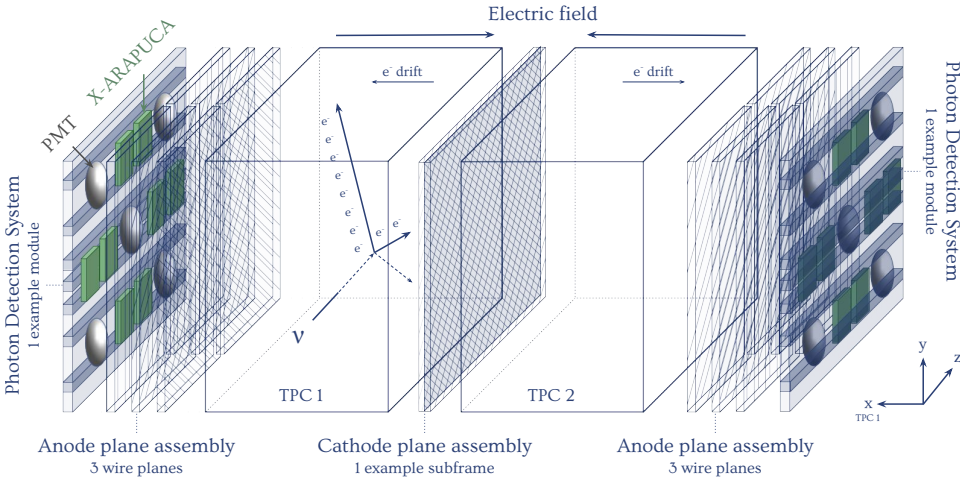

Figure 2.9: Illustration of a subvolume of the SBND TPC. An example of 2 PDS modules (one per TPC) is shown. An example of neutrino interaction is also visible.

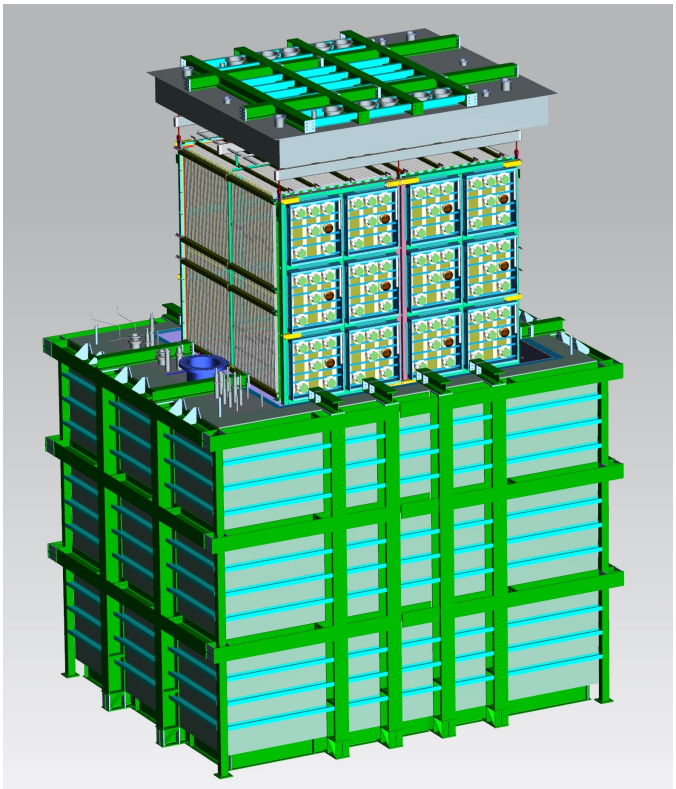

Figure 2.10: Technical design drawing of the SBND detector. The TPC is shown lifted out of the cryostat with a wall of PDS modules exposed.

Figure 2.11: Picture of the external cryostat taken during its construction.

POTs (∼3 years run), SBND will generate a dataset of ∼ 6 million ν_μ and ∼ 45 k ν_e CC events.

2.5 MicroBooNE and the Low Energy Excess

The MicroBooNE detector is a single LArTPC with a total active mass of 89 t of liquid argon, at a baseline of 470 m from the BNB source[48]. The cryostat has a cylindrical shape (Figure 2.12). The inner TPC has a volume of 2.3 m (H) × 2.6 m (W) × 10.4 m (L); it has a single cathode and anode planes and operates at a nominal electric field of 273 V/cm. The anode plane is composed of wire planes angled at ±60° and 0° to the vertical plane. The light collection system consists of primary and secondary sub-systems: the primary system is made of 32 optical units each consisting of a PMT located behind a wavelength-shifting plate. The secondary system consists of four light guide paddles, included in MicroBooNE as an R&D. MicroBooNE is located at shallow depth. The electron drift time is 2.2 ms, determining an increased rate of cosmic ray events per neutrino w.r.t. SBND or ICARUS. MicroBooNE was instrumented with a CRT system (installed after the first data run) composed of 4 planes, providing a coverage to the top, bottom and both long sides of the cryostat.

The MicroBooNE experiment collected ∼0.5 million neutrino interaction-from October 2015 until the beginning of 2021; Figure 2.13 shows a CC ν_e candidate collected by the MicroBooNE collaboration. MicroBooNE investigated the nature of the MiniBooNE LEE. A first set of results related to the low-energy excess were recently reported. They targeted multiple final-state topologies of CC ν_e interactions and NC Δ resonance decay producing

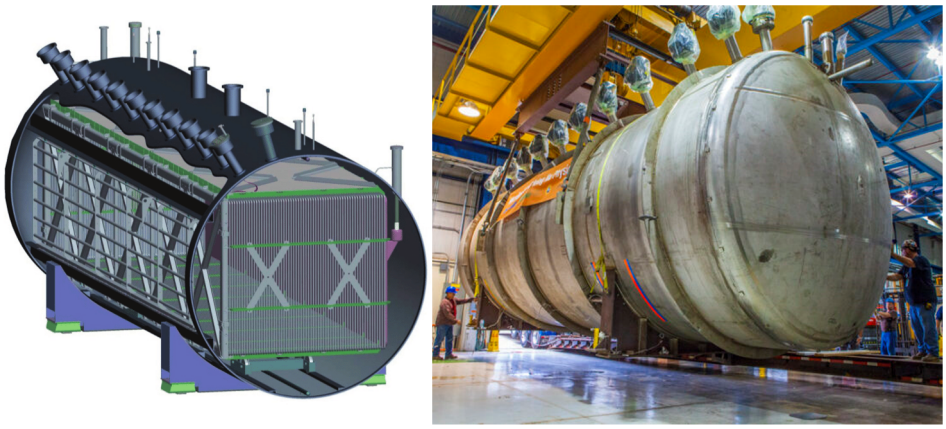

Figure 2.12: Left: schematic drawing of the MicroBooNE detector. Right: picture of the MicroBooNE cryostat.

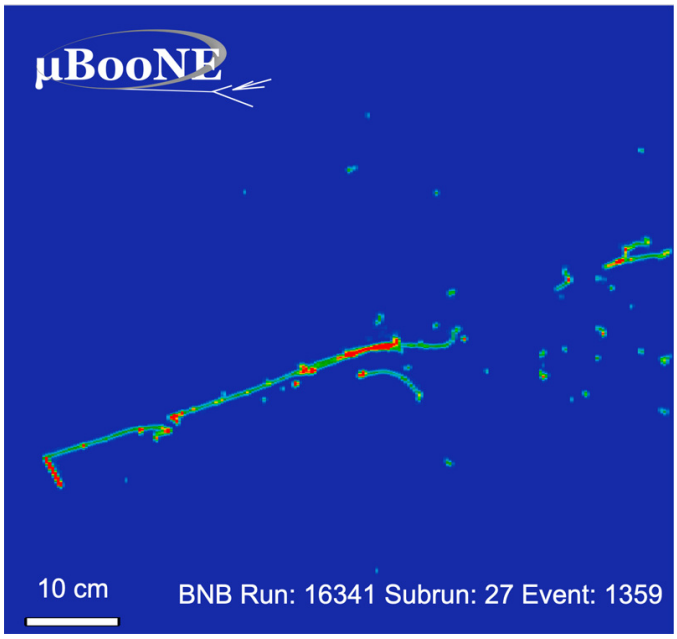

Figure 2.13: ν_e event in MicroBooNE from the event display.

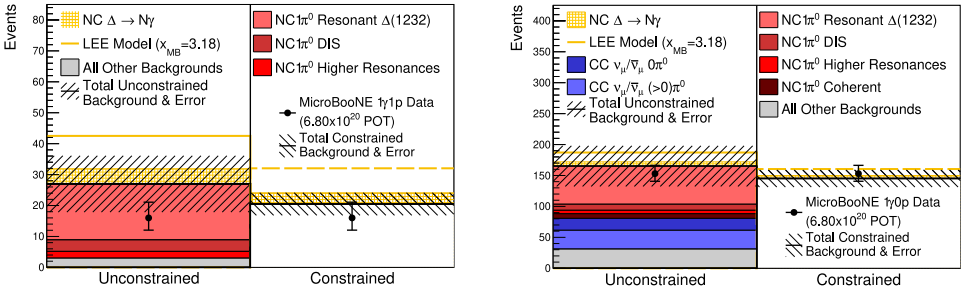

Figure 2.14: Observed rates for the $1\gamma 1p$ (left) and $1\gamma 0p$ (right) event samples. The comparisons with unconstrained and constrained background and LEE model predictions are shown.

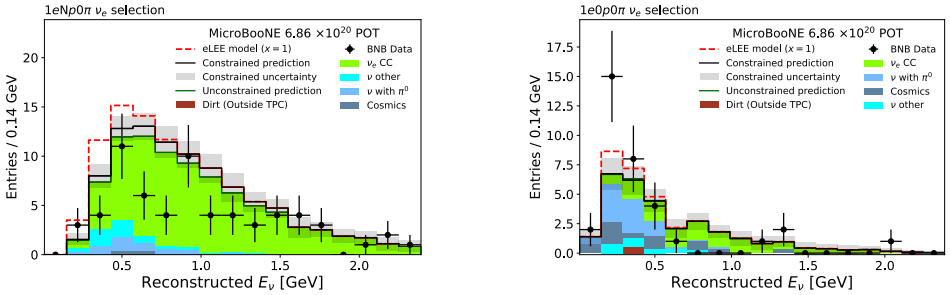

Figure 2.15: Reconstructed neutrino energy for the selected $1e\mathrm{N}p0\pi$ (left) and $1e0p0\pi$ (right) events in MicroBooNE. The prediction using the muon neutrino data is also shown with (red) and without (black) the eLEE model included.

a single photon in the final state[49, 50, 51, 52, 53].

The analysis of the single photon in the final state was performed in the $1\gamma 1p$ and $1\gamma 0p$ NC Δ single-photon channels. The results, presented in Figure 2.14, disfavour the most suspected single-photon background as a sole source of the MiniBooNE excess at 94.8% confidence level.

The hypothesis of an energy-dependent enhancement of intrinsic ν_e events at low energy was also tested. An empirical model was derived from MiniBooNE and three independent searches were performed on the MicroBooNE dataset targeting four different final states: $1e\mathrm{N}p0\pi$, $1e0p0\pi$, $1e1p$ and $1e\mathrm{X}$. The results of these analyses are reported in Figure 2.15 and Figure 2.16: the observed ratex of ν_e candidates are statistically consistent with the predicted background rates in the LEE region. With the exception of the low ν_e purity channel $1e0p0\pi$, the hypothesis that ν_e events are fully responsible for the median MiniBooNE LEE is rejected at 97% confidence level, and $>3\sigma$ in the inclusive channel.

Full 3+1 oscillation analyses were carried out to interpret the Micro-

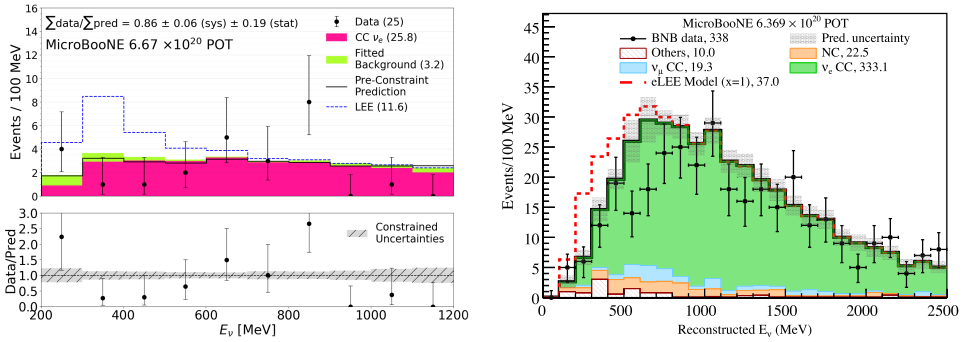

Figure 2.16: Left: reconstructed neutrino energy for the selected $1e1p$ events in a deep-learning-based analysis. The ν_e data is shown without (solid histogram) and with (red dotted) a model from MiniBooNE. Right: reconstructed neutrino energy for inclusive ν_e candidates events in the Wire-Cell based analysis. The predictions are shown both with (red) and without (black) a model of the LEE.

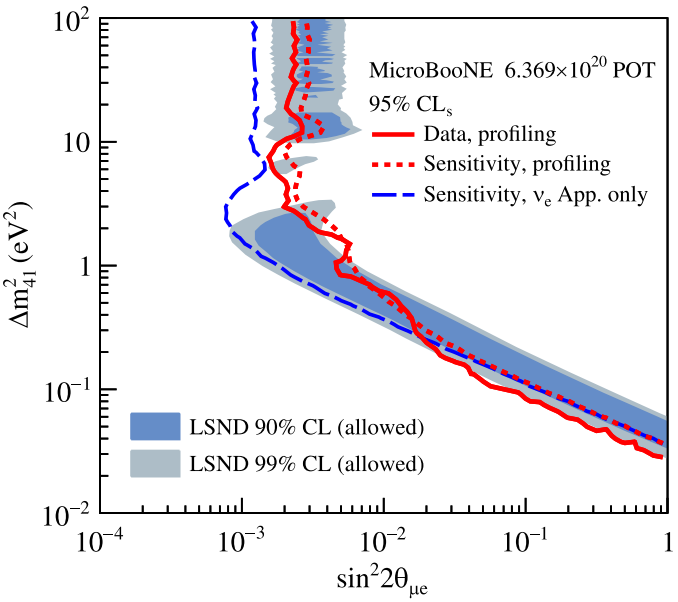

Figure 2.17: MicrooBooNE exclusion contours at the 95% confidence level for the $\nu_\mu \to \nu_e$ appearance channel.

BooNE eLEE (LEE with an electron in the final state) results under a sterile neutrino oscillation hypothesis. The data were found to be consistent with 3-flavour hypothesis and the resulting exclusion contours are presented in Figure 2.17. The existence of sterile neutrinos cannot be ruled out by the MicroBooNE eLEE results[54].

2.6 The SBN Far Detector: ICARUS

The ICARUS-T600 detector with an active mass of 476 t of liquid argon has been the first large-scale operating LAr-TPC detector[55, 56]. ICARUS (*Imaging Cosmic And Rare Underground Signals*) consists of two adjacent modules of 3.6 m × 3.9 m × 19.9 m filled with a total mass of 760 tons of liquid argon, which was purified by removing the electronegative impurities (H_2O, CO_2, N_2, etc.). Each module is composed of two LAr-TPCs, separated by a common cathode. The anode and the cathode planes have a maximum drift distance of 1.5 m, corresponding to ∼0.96 ms drift time at the nominal 500 V/cm electric drift field. The cathode is composed by an array of nine punched stainless-steel panels, granting a 58% optical transparency between the two TPCs. The anode plane is composed of three parallel wire planes 3 mm apart and oriented at different angles with respect to the horizontal direction: 0° (induction 1), +60° (induction 2) and -60° (collection). The anodic wires are made in stainless steel and have a diameter of 11μm; in total, 53,248 wires with a 3 mm pitch and maximum length of 9 m are installed in the detector. The anode plane is set at an appropriate wire bias tension such that the induction 1 and induction 2 planes provide a non destructive charge measurement and the ionization charge is fully collected by the collection plane. The optical system is composed of PMTs located behind the anodic wire planes, to collect the scintillation light used to generate the global event trigger.

2.6.1 ICARUS at LNGS

The ICARUS-T600 detector was first built and tested in Pavia, then, in 2004 it was moved in the hall B of LNGS. In 2013, ICARUS completed a 3 years long run collecting 3000 neutrino events on the CNGS beam, corresponding to 8.6 $\times 0^{19}$ protons on target. During the data taking, the liquid argon was kept at an exceptional purity level, reaching a 16 ms lifetime.

Results from the Gran Sasso data taking campaign demonstrated high-level technical performances and the feasibility of the LAr-TPC technology at the kton scale. The event reconstruction showed a remarkable e/γ separation and particle identification exploiting the measurement of dE/dx versus range. The momentum of escaping muons was measured by the multiple Coulomb scattering with $\sim 15\%$ average resolution in the $0.4 - 4$ GeV/c energy range, which is relevant for the next generation neutrino experiments.

Figure 2.18: Picture of the ICARUS TPC during the CERN overhauling. Cathode (left), field shaping electrodes (top and bottom) and PMTs (right) are visible.

In addition, cosmic ray events were studied, identifying 6 ν_μ CC and 8 ν_e CC events in a 0.43 kton·y exposure.

2.6.2 ICARUS Overhauling at CERN

At the end of the data-taking at LNGS, ICARUS was disassembled and moved to CERN, where it underwent a significant overhauling. The refurbishing mainly consisted in:

- the realization of new cold vessels with purely passive insulation;
- an improved cryogenic system and LAr purification equipment;
- flatting of the TPC cathode;
- the implementation of new TPC read-out electronics;
- the upgrade of the LAr light detection system.

In Figure 2.18 an inner view picture of the ICARUS TPC during its overhauling at CERN is shown.

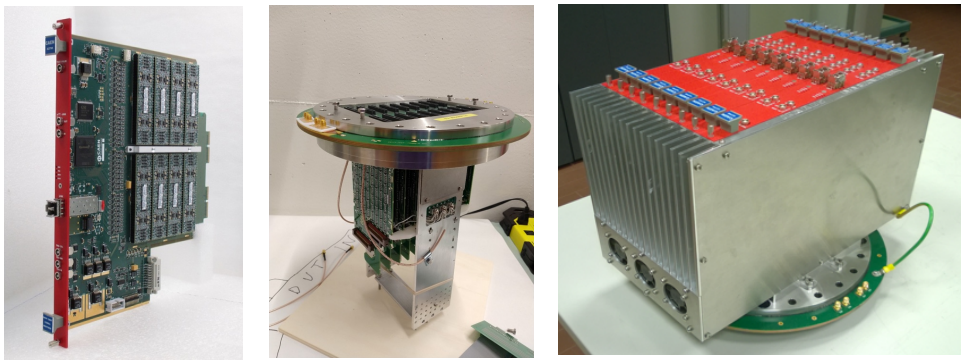

Figure 2.19: Left: A2795 custom board housing 64 amplifiers, AD converter, digital control and optical link. Center: assembled feed-through with nine DBBs and the biasing cables. Right: a mini-crate populated by the nine A2795 boards installed on a feed-through flange.

The TPC electronics

The electronics used in ICARUS at LNGS was based on flange modularity, each flange serving 567 TPC wire-channels. The analogue front-end integrated the cascode stage with two different filtering, one for collection and induction 1, another for induction 2 with the aim to produce in all the cases an unipolar signal. This showed strong limitations in the induction 2 signals in case of dense showers. During the overhauling, new electronics for the 53,348 wire-channels were designed to be compatible with the higher data rates foreseen at FNAL. The new electronics adopts the same modularity and architecture, but the analogue and digital electronics are integrated into the same custom board mounted directly onto the flange. Moreover, all the amplifiers have the same filtering, preserving the bipolar structure of induction 2 signals without distortion. The VME standard was abandoned in favor of a serial optical link, allowing for gigabit band-width data transmission, compatible with the higher rates. TPC wires are fed into the front-end amplifiers by means of Decoupling Biasing Boards (DBBs). The DBB has two functions: biasing each wire and conveying the signals to the amplifiers. The flange is realized in a multi-layer solid PCB $\sim$ 6 mm thick. Nine electronic A2795 boards are hosted by a mini-crate installed on a feed-through flange. In Figure 2.19 pictures with details of the overhauled TPC electronics are shown.

Scintillation light detection system

The ICARUS-T600 light detection system consists of 360 8 " Hamamatsu R5912-MOD PMTs installed behind the anodic wire planes, 90 PMTs per TPC. Since the PMT glass is not transparent to the 128 nm LAr scintillation

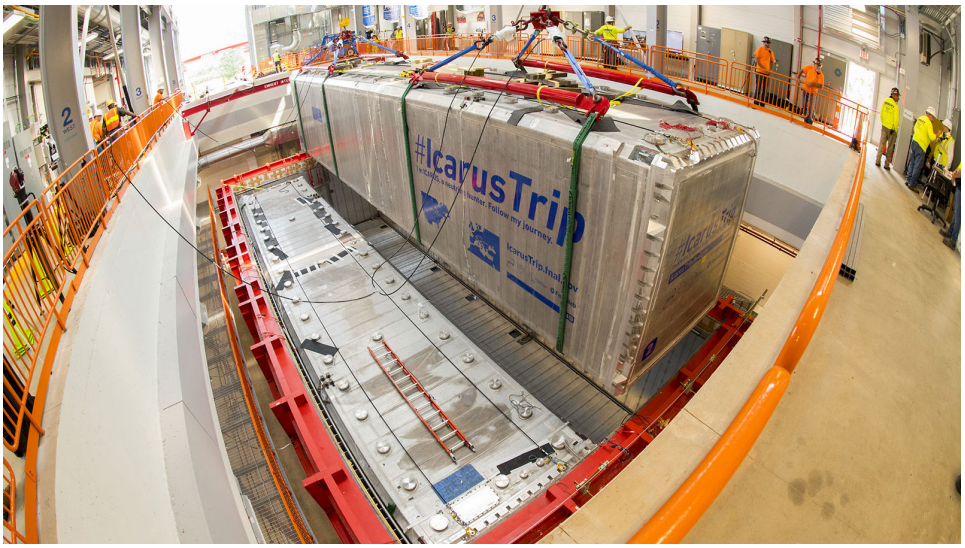

Figure 2.20: Deployment of the ICARUS T300 modules inside the pit of the SBN far detector experimental hall in August 2018.

light, each device was coated with Tetra-Phenyl Butadiene (TPB), to convert VUV photons to visible light. All PMTs are mounted into the wire chamber mechanical frames using supporting systems, 5 mm behind the collection plane wires. A stainless steel grid cage is mounted around each PMT to mitigate the induction of fake signals on the nearby wire planes. The light detection setup is equipped with a laser calibration system allowing for gain equalization, timing and monitoring of all the PMTs.

2.6.3 ICARUS at FNAL

After its overhauling at CERN, ICARUS was shipped to Fermilab in July 2017 and installed in the SBN far detector building in August 2018. In Figure 2.20 a picture of the deployment of the last T300 module inside the far detector pit is shown.

For the operations at Fermilab, the entire ICARUS-T600 cryogenic and purification system was rebuilt anew, following the original implementation at LNGS. Its main components are:

- LAr cold vessels, 273 m^3 each;
- set of heat exchangers filled with LN_2 (cold shields) surrounding the cold vessels;
- $\sim$ 600 mm thick thermal insulation made of polyurethane foam panels;
- warm vessel, providing encloseure and mechanical support for the thermal insultation;

Particle	without OB [Hz]	with OB [Hz]	without/with OB
$\mu^{\pm}$	17117	12761	1.34
p	54	0.10	> 500
γ	116	0.03	> 3500
n	1426	6.8	> 200

Table 2.1: Rate (Hz) of secondary cosmic particles at ground level with E_k>50 MeV entering the LAr active volume with and without the concrete overburden, chapter 2.6.4.

- LN_2 cooling circuits;
- argon gas recirculation units;
- liquid argon recirculation units;
- cryogenic control systems;
- LN_2 and LAr storage dewars;
- dedicated purification unit.

2.6.4 Cosmic Background

The ICARUS-T600 detector was initially designed to operate in the low muon cosmic background of the Gran Sasso laboratory. The conditions at FNAL are completely different: the detector is located at shallow depth ($\sim$ few meters) where the cosmic rays background may induce several additional and uncorrelated triggers during the $\sim$ 1 ms drift time. The expected rate of cosmics depositing more than 100 MeV within the T600 active volume is $\sim$ 17 kHz[57]. On average $\sim$ 17 cosmic muons are expected to cross the detector volume during the 0.96 ms event drift time. The cosmic ray fluxes on ICARUS were simulated using CORSIKA and including only the primary protons (*proton-only model*), predicting a total flux for $\mu^{\pm}$ above 50 MeV of 129 Hz/m^2. Figure 2.21 shows the flux of different particles impinging the roof of the ICARUS building.

In order to mitigate the cosmogenic induced background, the ICARUS-T600 detector is surrounded with an external *Cosmic Ray Tagger system* (CRT) below a 3 m concrete overburden (6 m water equivalent). The CRT system is described in-depth in chapter 3. A preliminary evaluation of the cosmic ray flux reduction through the ICARUS TPC by means of the concrete overburden was performed by simulating a total exposure of 6.6×10^{20} POTs with and without the OB. Table 2.1 summarizes the expected rate of different primary particles crossing the active LAr for kinetic energy >50 MeV. The overburden reduces the dominant muon flux by $\sim$ 20%, stopping the muons with a $E_K \leq$1.5 GeV. The suppression is more effective for

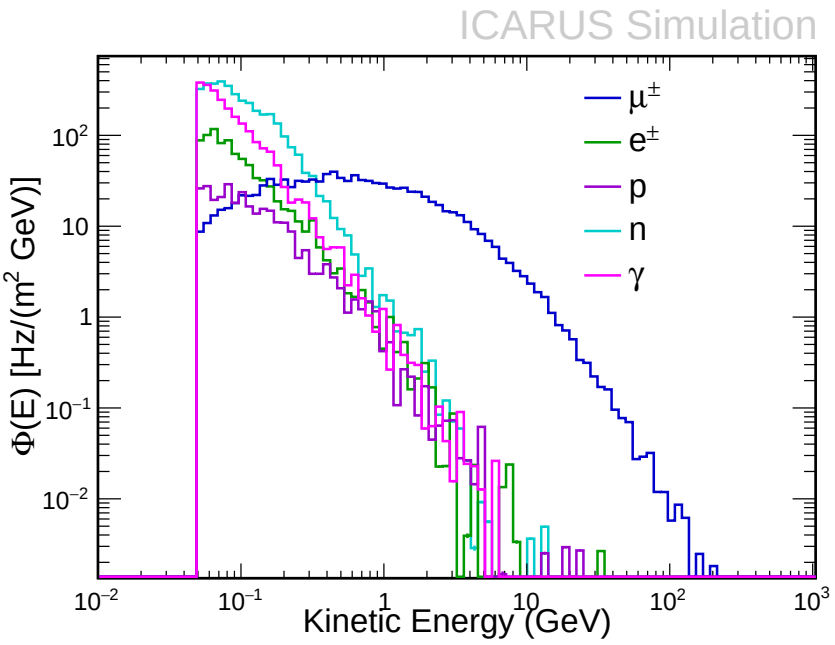

Figure 2.21: Cosmic ray fluxes impinging on the experimental hall predicted by CORSIKA proton-only model.

hadrons, with a reduction by a factor ~ 200 of primary neutrons and ~ 500 for the protons. Primary γ's are almost fully suppressed.

One of the most important sources of background to the ν_e appearance analysis is due to electromagnetic showers induced by γ produced by cosmic particles propagating through the detector and in the surrounding materials. By showering withing the active liquid argon volume, the cosmogenic photon can mimic a genuine $1e0p$ ν_e CC interaction. Figure 2.22 shows the overall number of γ initiated showers for an exposure 6.6×10^{20} POTs with (dashed lines) and without overburden (solid lines) for different cosmic parents. The results of the simulation show that the overburden reduces the most serious background due to γ initiated showers with kinetic energy > 200 MeV.

The ICARUS Overburden

The Overburden (OB) deployed on top of the ICARUS CRT is composed of three 1 m concrete layers, or 6 m water equivalent. The OB installation started in April 2022 after the completion of the Top CRT commissioning. The first OB layer is composed of 0.5 m wide blocks of low radioactive materials across the whole ICARUS pit. The concrete blocks are installed 10 cm above the Top CRT horizontal modules. Figure 2.23 shows the deployment of the first block floating on top of the sub detector. For the second and third layer of the OB, concrete blocks repurposed from previous Fermilab

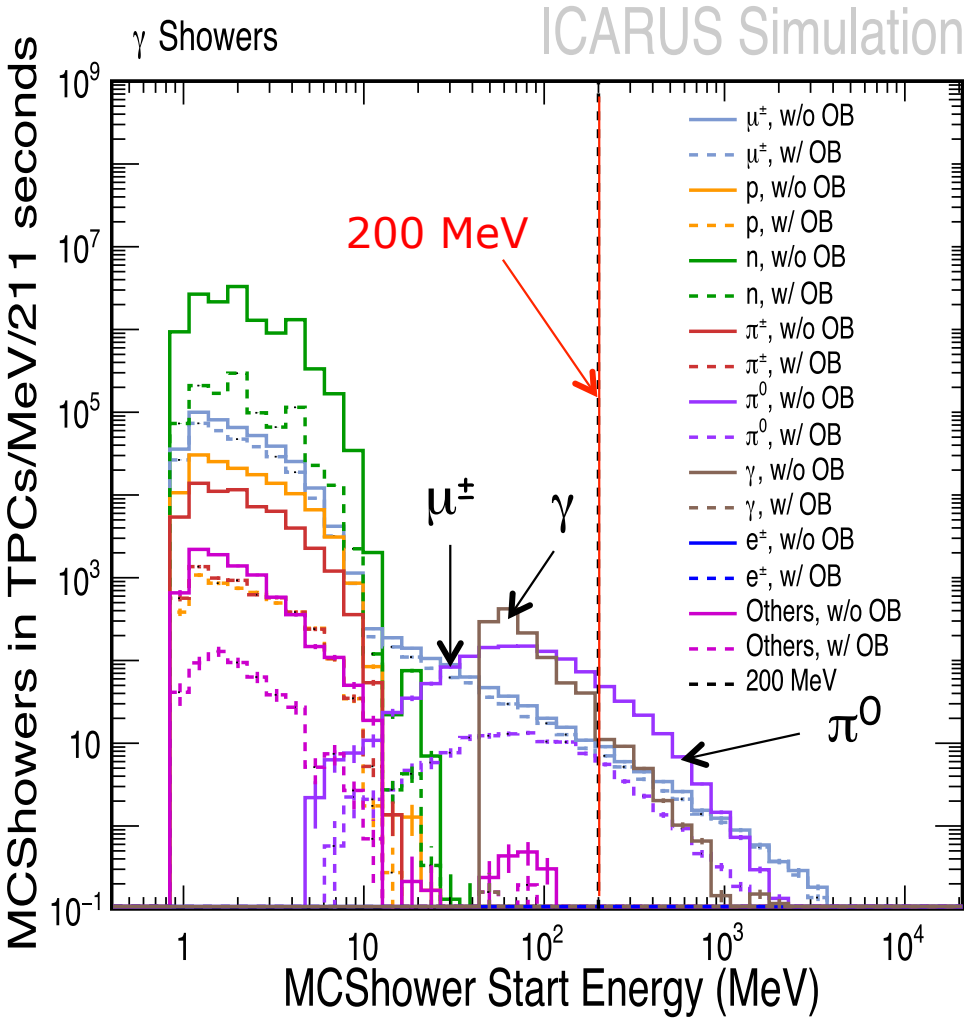

Figure 2.22: γ showers initiated in the active volume branching off their cosmic parent (211 s, corresponding to an exposure of 6.6×10^{20} protons on the BNB target): without (solid lines) and with overburden (dashed lines).

Figure 2.23: Picture taken during the deployment of the first concrete overburden block on top of the ICARUS CRT.

experiments were used. Before their installation, the blocks were tested with a Geiger counter to verify the low radioactivity. The concrete overburden was fully installed by mid June 2022 and its completion set the start of the beginning of the ICARUS Run 1. The completed overburden is shown in Figure 2.24.

2.6.5 ICARUS standalone physics program

The reactor Neutrino-4 experiment claims with a 2.7σ confidence level the observation of sterile neutrino-like oscillatory pattern with a characteristic period of 1.4 m for $\sim$ 4 MeV, with best fit parameters Δm^2_{N4}=7.25 eV^2 and $\sin^2 2\theta$=0.26. An oscillation with such parameters should be observable both with ν_e and ν_μ. The ICARUS experiment can provide a definitive verification the Neutrino-4 claim by testing both the ν_μ (BNB and NuMI) and ν_e (NuMI) disappearance channels.

A Neutrino-4 like oscillatory pattern should be directly observable in the ν_μ/ν_e survival probability as a function of L/E, averaged over the 50 m of pion decay tunnel. Figure 2.25 shows the signature of the Neutrino-4 like signal at ICARUS considering $\sim$ 11500 ν_μ CC events in 3 months of data taking on the BNB. Figure 2.26 shows the Neutrino-4 signature at ICARUS with a data sample of $\sim$ 5200 ν_e CC interactions collected on the NuMI beam line.

Figure 2.24: Picture of the fully completed ICARUS overburden.

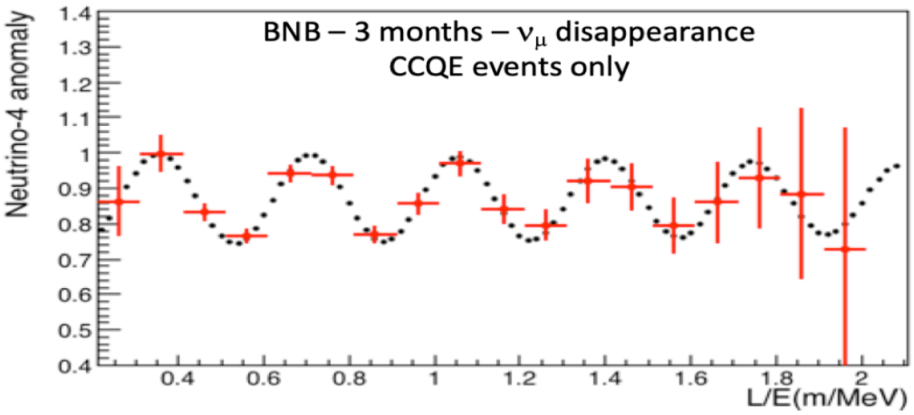

Figure 2.25: Predicted survival ν_μ oscillation probability for the Neutrino-4 anomaly (black) for the best fit (Δm^2_{N4}=7.25 eV^2 and $\sin^2 2\theta$=0.26) and expected signature observed at ICARUS with 3 months of BNB data (red).

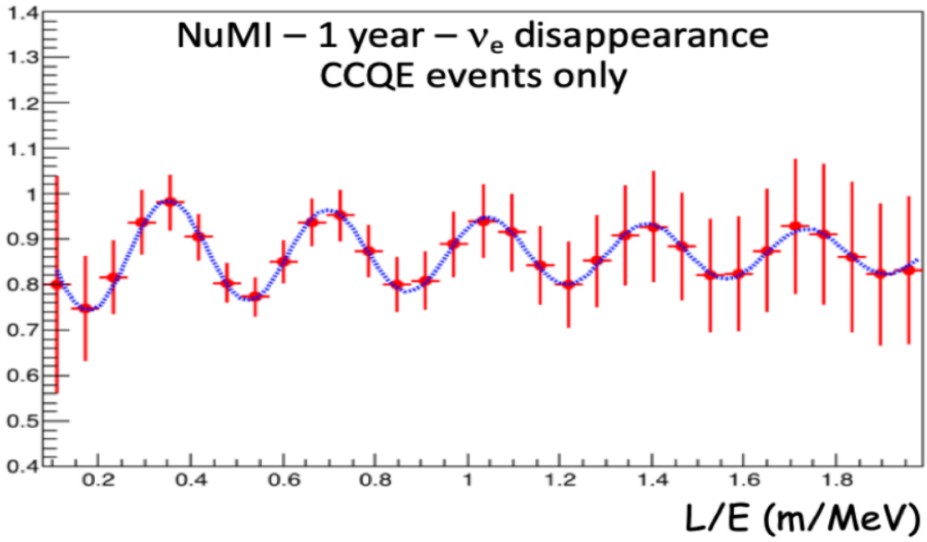

Figure 2.26: Predicted survival ν_e oscillation probability for the Neutrino-4 anomaly (blue) for the best fit (Δm^2_{N4}=7.25 eV^2 and $\sin^2 2\theta$=0.26) and expected signature observed at ICARUS with 1 year of NuMI data (red).

Figure 2.27: Picture of the ICARUS roof at Fermilab during the commissioning phase and before the Top CRT installation.

2.6.6 ICARUS-T600 commissioning

Starting from February 2020, the ICARUS-T600 began its filling operation with purified liquid argon. The filling was completed by mid April when the recirculation system was turned on. The detector activation took place by the end of August 2020, when the TPC wire planes and the cathode high voltage were taken to nominal voltages (75 kV for the cathode). All PMTs were also switched on and calibrated with the laser system and the detector started its data acquisition with a random 5 Hz trigger for calibration purposes (electron lifetime, space charge and drift velocity). Figure 2.27 shows a picture of the ICARUS-T600 roof taken during the commissioning phase of the detector, before the Top CRT installation.

Throughout 2021, the PMT and TPC systems were commissioned and included in the data acquisition. A trigger system was developed to trigger on the BNB and NuMI beam spill gates by means of the *Early Warning* signals, respectively sent 25 and 730 ms ahead of the protons on target firing. The trigger system is based on LVDS signals generated by the PMT digitizers; a more in depth description is provided in section 4.5.1. The ICARUS-T600 was first fully operational in June 2021 and in November 2021 it started data collection on both the BNB and NuMI beams. As a first of the general behaviour of the detector, a visual study campaign of the collected events was performed to select and identify neutrino interactions in the active liquid argon using a graphical event display. An example of a ν_μ CC candidate is shown in Figure 2.28, with an estimated total deposited energy of ~ 1.1 GeV. The CC muon candidate is 3.8 m long, while the highly ionizing track was identified as a 20 cm long proton track. The visual scanning also allowed the identification of the first ν_e CC candidates in the NuMI beam, an example is shown in Figure 2.29, with a total deposited energy of ~ 600 MeV.

The ICARUS commissioning was concluded by June 2022, following the commissioning of the Top CRT and the full deployment of the concrete overburden[58]. Throughout its commissioning phase, ICARUS collected 296×10^{18} and 503×10^{18} POTs on BNB and NuMI, respectively, with an overall beam efficiency, defined as the amount of POT collected vs the delivered, of 89% for BNB and 88% for NuMI.

2.6.7 ICARUS Run 1

The ICARUS Run 1 officially began on June 9 2022 and lasted until the beam summer shutdown on July 10 2022. The data acquisition was largely successful, with uninterrupted physics runs with a ~ 1 day duration extended up to 5 days. During Run 1 the experiment collected $\sim 6.8\times10^{19}$ POTs and $\sim 4.1\times10^{19}$ POTs for NuMI and BNB respectively. Figure 2.30 shows the POTs delivered and collected by ICARUS for both the BNB and NuMI beams during the Run1. ~ 6000 ν_μ CC quasi-elastic events are expected from

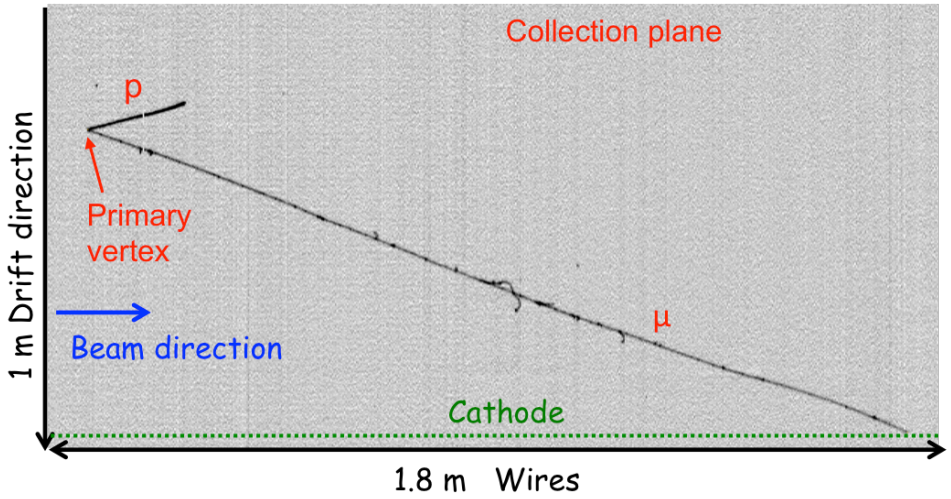

Figure 2.28: A visually selected ν_μ CC candidate from the BNB beam.

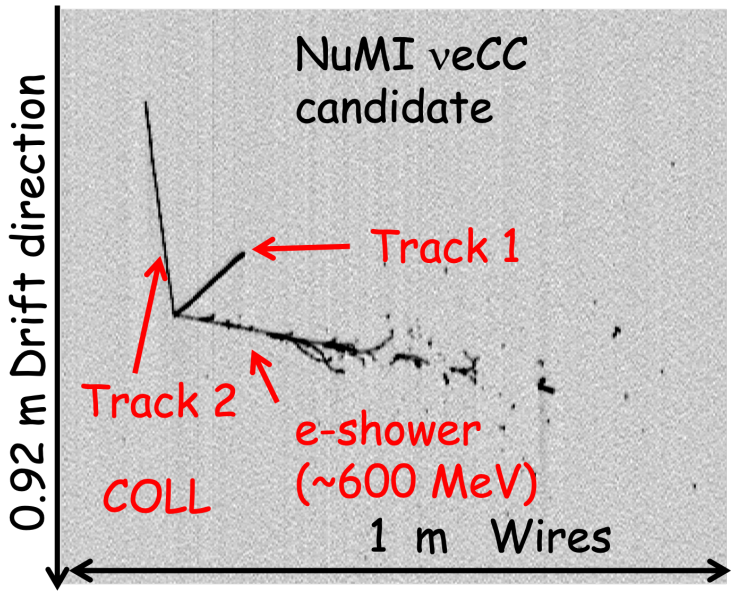

Figure 2.29: A visually selected ν_e CC candidate from the NuMI beam.

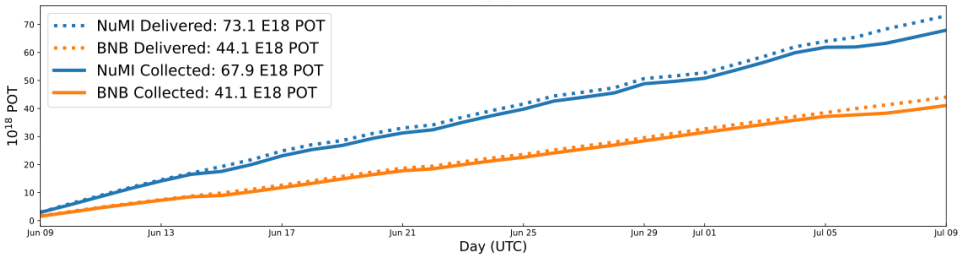

Figure 2.30: Plot of the POTs collected and delivered for both the BNB and NuMI beams throughout the ICARUS Run1.

the Run1 BNB data sample. These events will be used for the Neutrino-4 physics analysis.

Chapter 3

The Cosmic Ray Tagger System

The CRT system is a subdetector external to the cryostats aimed at identifying charged particles passing through or near the TPC active volume. With an expected time resolution of few ns for both the PMT and CRT systems, their synchronization and synergy enable to determine the direction of tagged particles. Moreover, by a fine timing calibration campaign, a preliminary filtering of events can be achieved by discarding those where the primary event trigger was due to a tagged entering cosmic particle.

The CRT system covers a surface area of $\sim$1100 m^2, it is divided into three different subsystems, each deployed over different regions of the TPC: Top CRT, Side CRT, and Bottom CRT. In Figure 3.1 a drawing of the CRT system with the Top and Side CRT sub-systems is shown. The three different systems complement one another, granting the possibility to identify $\sim$95% of the passing through cosmics. The CRT sub-detectors are comparable in terms of timing and spatial resolution. Top and Side CRT also share a common Front End Board (FEB) for the readout and biasing of the Silicon Photo-Multipliers (SiPMs).

In this thesis, I will give more emphasis to the Top CRT system because I contributed significantly to the different steps, from the testing of the prototype, to its construction, installation, commissioning and integration in the common data acquisition system.

3.1 The Bottom CRT

The layout of the Bottom CRT is sketched in Figure 3.2 (left): it consists of 14 modules divided into two daisy chains of 7 modules each and installed under the TPC warm vessel. The modules, repurposed from the Double Chooz experiment, consist of two layers of 32 parallel polystyrene scintillator strips, 5 cm wide each, [59]. A wavelength-shifting fiber is placed and read-

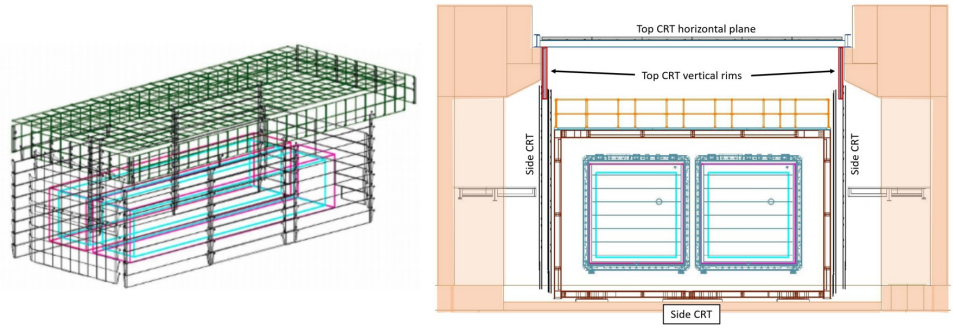

Figure 3.1: (Left) CRT layout including the cold vessels (magenta) and the argon active volumes (cyan). The Top and the Side CRT subsystems are visible. (Right) Design of the CRT system from the beam perspective.

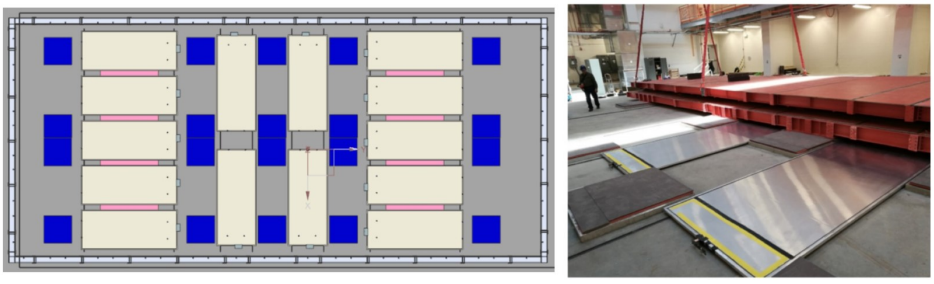

Figure 3.2: (Left) top-down view of the Bottom CRT layout. Each scintillation modules is illustrated as a yellow rectangle, blue squares are the warm vessels support feet. (Right) picture of the fully installed Bottom CRT modules during the warm vessel deployment.

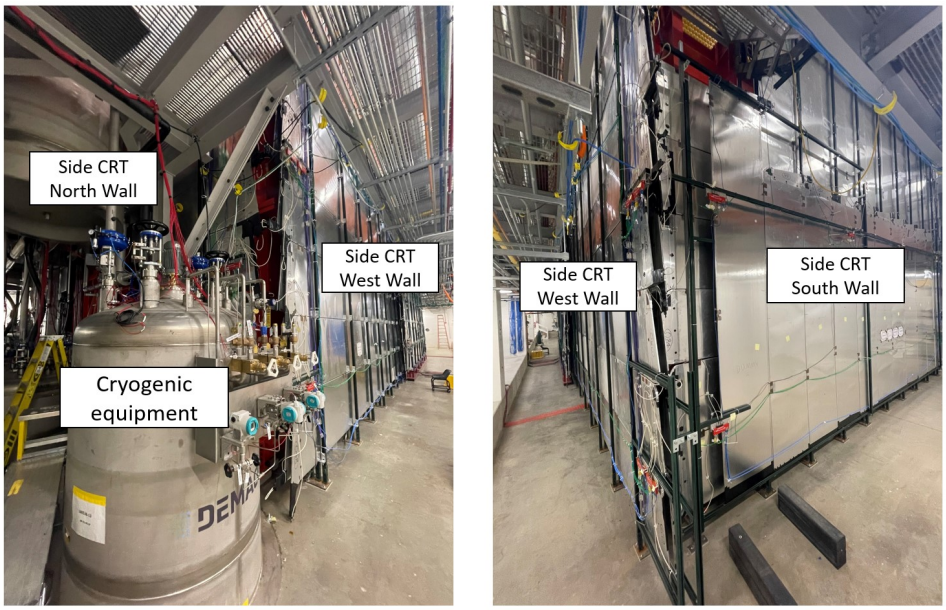

Figure 3.3: Left: picture of the Side CRT north and west walls as visible from the north-west corner of the ICARUS building ground pit. Right: picture of the Side CRT south and west walls as visible from the south-west corner of the ICARUS building ground pit.

out at one end by an Hamamatsu H8804 M64 multianode PMT, while its other end is mirrored. The overall dimensions of each module are 4 m $\times$ 1.6 m $\times$ 3.2 cm.

In Figure 3.2 (right) a picture of the inner most bottom CRT modules is shown. On September 2019, before the integration of the bottom CRT into the data acquisition system, the sump pump that prevents rainwater flow in the bottom pit of the SBN-FD building failed and a $\sim$2 inches flood was discovered. The water damaged the Bottom CRT readout electronic. Due to the presence of the warm vessel, it was not possible to access and repair the damaged boards. During further investigations in 2022, it was possible to isolate the damage to only 2 boards, which, due to daisy chaining, prevented the downstream half of the Bottom CRT from working. Additional testing of the upstream half of the Bottom CRT is expected in 2023 using a standalone DAQ. If the test will be successful, the upstream half of Bottom CRT will be included in the full detector data acquisition by the end of 2023.

3.2 The Side CRT

The Side CRT makes use of decommissioned scintillator modules from the MINOS experiment [60]. Each module is composed of twenty adjacent strips

of 800 cm × 4 cm × 1 cm polystyrene scintillator. The scintillator is contained in a metal sheath, and each strip has an embedded WLS fiber running down the middle. WLS fibers are collected at the end of the modules and connected to the optical readout, consisting of an array of ten Hamamatsu S14160-3050HS SiPMs. Each SiPM reads out two fibers and corresponds to a single electric readout channel on CAEN A1702 Front-End Boards. The Side CRT sub-detector is divided into eight different regions, each composed of two layers of MINOS modules: north (downstream), south (upstream), west-north, west-center, west-south, east-north, east-center and east-south. The upstream wall is the only one that exploits a configuration in which the two layers are arranged orthogonally (*X-Y configuration*); to achieve this, the modules oriented vertically were cut in half. Side CRT modules on the east and west regions consist of full-length modules with strips arranged horizontally and parallel to the cryostat. Due to the excessive length of the module with respect to the cryostat, central walls of both east and west regions are offset in order to allow modules overlapping. To grant access to the FEBs, the Side CRT mounting structures are fixed to rolling platforms. Due to its proximity with the liquid argon filtering system, the north wall is composed of cut MINOS modules of different lengths to maximize the coverage of the available surface. All the Side CRT modules, with the exception of the cut modules, are read-out on both ends of the scintillator strips, while the cut modules on the north wall and south wall (vertical modules) are read-out on one end only. In Figure 3.3 two pictures of the Side CRT taken from the groundpit of the ICARUS building on the north-west (left) and south-west (right) corners are shown. The full Side CRT system consists of 2,710 red-out channels across 93 FEBs, with 136 full and 81 cut modules in total.

3.3 The Top CRT

The Top CRT is designed to intercept 80% of the cosmic muons entering the ICARUS LArTPC. It is made of 123 modules: 84 modules are installed on the top horizontal plane, while 39 modules cover the upper perimeter of the TPC (vertical rims). In Figure 3.4 a scheme of the installed Top CRT is shown.

The modules are hodoscopes consisting of two orthogonal layers of eight 23 cm wide casted scintillator bars, encased in 1.86 m × 1.86 m aluminum boxes. The scintillator bars used in the top (bottom) layer are 10 (15) mm thick. The strips of the top layer were produced by the NUVIA company in Czech Republic and consist of casted polystyrene-based scintillators. The strips of the bottom layer were produced by the Institute for Scintillation Materials (ISMA) in Ukraine and consist of polyvinyltoluene scintillators. Overall, 2000 scintillators have been used for the Top CRT modules. An illustration of the Top CRT design is provided in Figure 3.5. Figure 3.6

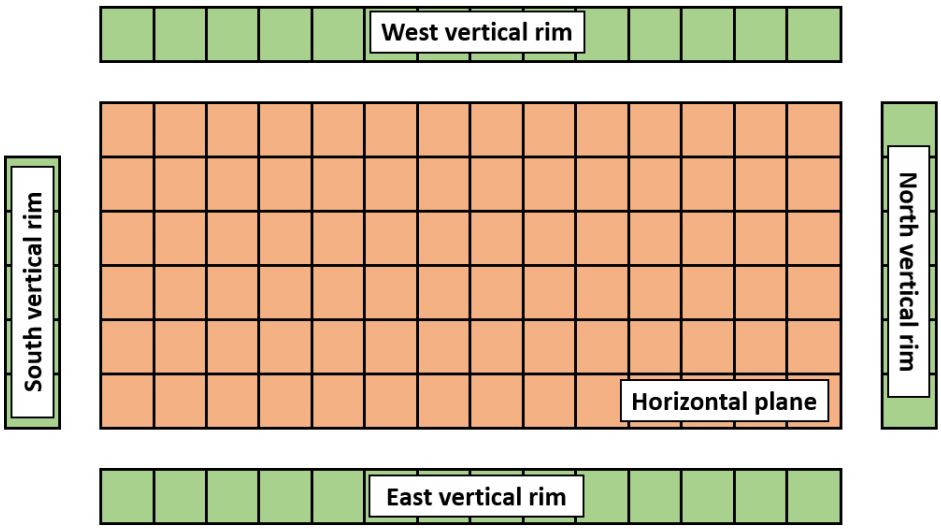

Figure 3.4: Illustration of the installed Top CRT modules at the far detector building. Orange modules are arranged horizontally on top of the cryostat, green modules are installed vertically.

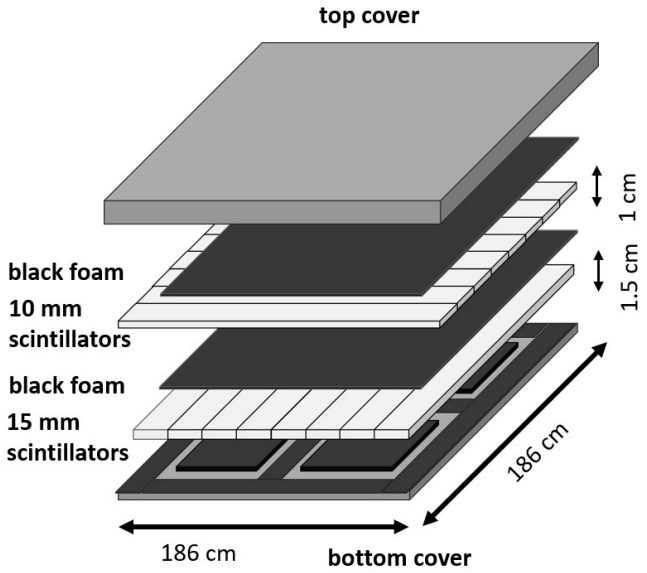

Figure 3.5: Illustration of the Top CRT module design, consisting of two orthogonal layers of eight scintillator bars, encased in an aluminum box.

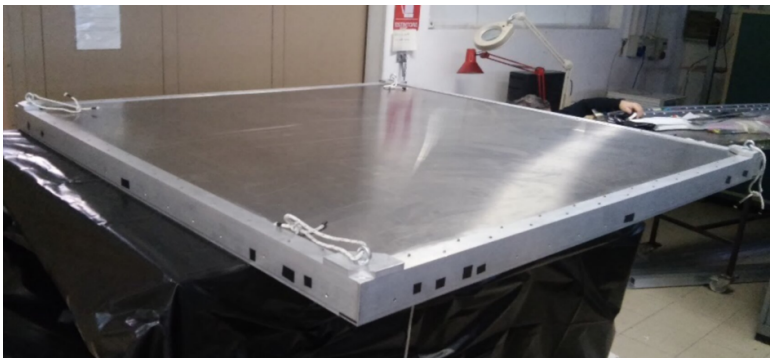

Figure 3.6: Picture of the Top CRT prototype assembled in Bologna INFN laboratories.

shows the Top CRT module prototype, assembled and tested at in Bologna INFN laboratories.

Each Top CRT scintillator strip is instrumented with two WLS fibers embedded along the longitudinal direction of the bar and located 6 cm from each side, as can be seen in the illustration in Figure 3.7 (bottom). The fibers are Kuraray Y-11(200), with an absorption peak at 430 nm, an emission peak in the green at 476 nm and an attenuation length greater than 3.5 m. The fibres are read-out only from one end, the opposite end-side is mirrored in order to enhance the light yield. The mirroring consists of polishing the end of the fiber and then coating it with aluminum reflective layers of a few micron thickness by aluminum spattering in vacuum. The WLS fibers were glued in the scintillator groove with an epoxy based hard optical cement. A total number of $\sim$ 7,400 m fibers were used for the construction of the Top CRT system. The light read-out is performed by an Hamamatsu S13360-1350CS SiPM (Figure 3.8 left), with an active area of 1.3 mm $\times$ 1.3 mm. The pitch of the pixels is 50 μ m, for a total of 676 cells per SiPM. The fill factor F is 74% and the breakdown voltage is 53$\pm$5 V. The probability of crosstalk is $\sim$ 3% and the photon detection efficiency is $\sim$40% at 450 nm. The SiPMs were inserted and glued (using a soft silicon based optical glue) into a custom made SiPM-holder and connected to the scintillator bar and to the wavelength shifting fibre. In Figure 3.8 (right) an illustration of the WLS to SiPM coupling is shown. SiPMs pins are connected to a PCB and routed via 50 Ω micro-coaxial cables 1.8 m long, carrying both signal and bias voltage to a PCB patch panel connected to the Front End Board. Overall, 4000 SiPMs were installed in the Top CRT modules, the assembling and testing of the modules was performed at the INFN-LNF in Italy.

In order to prevent damages during the transportation to FNAL, the inner volume of the aluminum box was covered with black sponge-like tape and each scintillator layer was separated with a black foam-like plastic sheets.

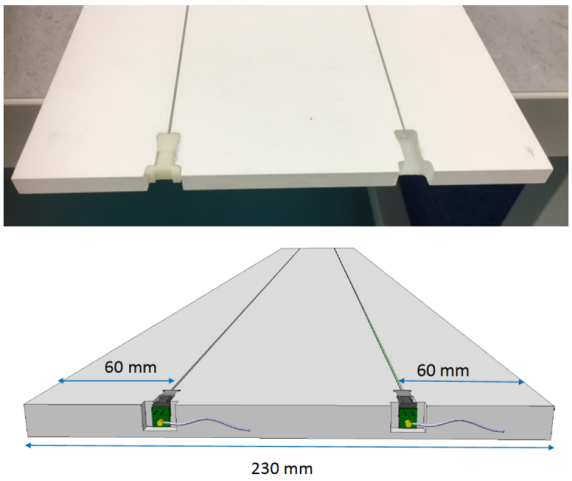

Figure 3.7: Top: picture of the 10 mm NUVIA scintillators, with a detail of a SiPM connector on the left and the empty socket on the right. Bottom: illustration of the fibers disposition along the scintillator bar.

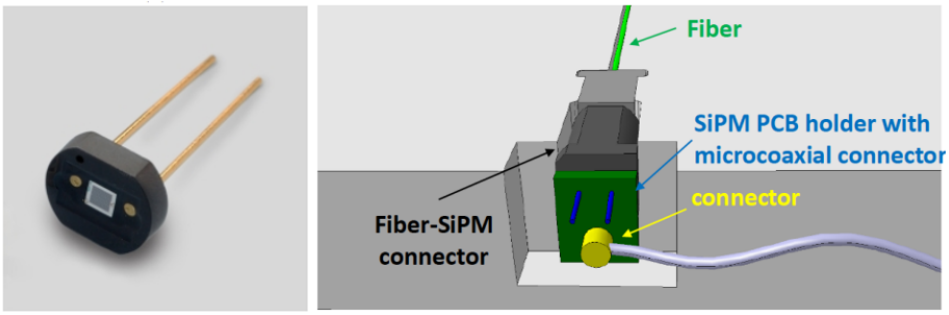

Figure 3.8: Left: picture of the Hamamatsu S13360-1350CS SiPM. Right: illustration of the SiPM connection scheme to WLS fiber.

Figure 3.9: Top: picture of the assembled scintillator hodoscope of the Top CRT. Bottom: picture of the CRT hodoscope wrapped in Tedlar® and black foam-like plastic sheets.

Figure 3.10: Picture of the last transportation rack of Top CRT modules built at LNF.

Before the enclosure of the aluminum box, the assembled scintillator strips are wrapped with Tedlar® strips to prevent reflected light from reaching the scintillators and the SiPMs, thus ensuring light tightness. In Figure 3.9 two pictures of the assembled scintillator hodoscope before and after the protective wrapping are shown. The construction of the modules started in April 2019 and was concluded in February 2020; Figure 3.10 is a picture of a transportation rack of 10 modules.

3.3.1 The Front End Boards

The Front End Board used, which is common to the Side CRT, is based on a multichannel custom design developed at the AEC for Fundamental Physics of the University of Bern and commercialized by CAEN [61]. The analog input signal is processed by a 32-channel ASIC (*CITIROC* [62]). For each channel the chip provides charge amplification with configurable gain, fast shaping with the peaking time of 15 ns and slow shaping with configurable peaking time in the range of 12.5 ns to 87.5 ns. The signal from the fast shaper is discriminated at configurable level and produces digital signals (T0-T31) for event triggering. These 32 signals are routed to an XILINX

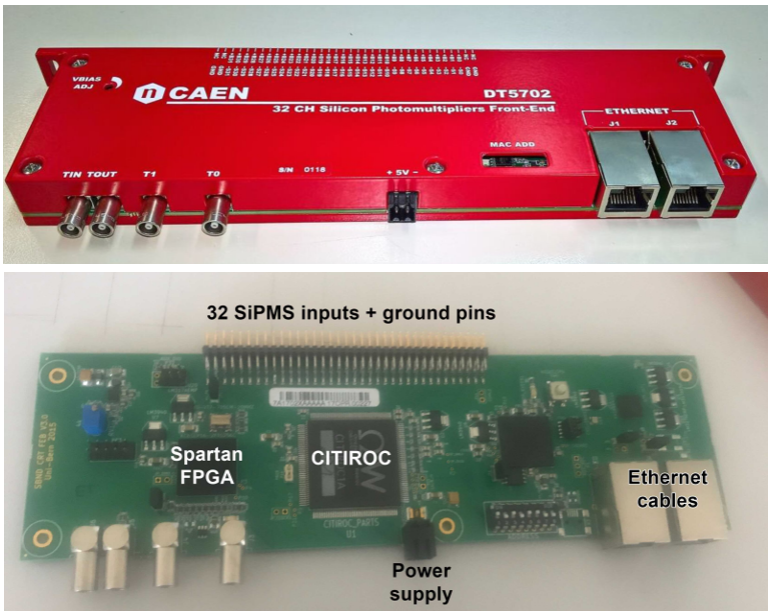

Figure 3.11: Top: the FEB in its case. Bottom: the FEB internal components

Spartan-6 FPGA chip, where the basic input coincidence and triggering logic is realized. The board communicates with the host computer via the Ethernet protocol. Two pictures of the FEB are shown in Figure 3.11.

Time stamp generator

The Time-to-Digit Converter (TDC) of the time stamp generator is composed of the coarse counter, working at a clock frequency of 250 MHz, and of the delay chain interpolator, improving accuracy down to 1 ns. The 20 MHz temperature compensated voltage controlled crystal oscillator (VCXO) is used as a source for the reference clock of the FPGA and the timing circuit. The feedback voltage for the VCXO is generated by the 10-bit DAC under control of the on-board CPU. The time stamp is defined as the interval of time between the event of interest and the input reference pulse. For each event, the FEB records two independent time stamps w.r.t. the positive rise edge on the *T0* and *T1* LEMO inputs. Each time stamp is a 32-bit word, with the two most significant bits used to flag special events. Two special events are foreseen, the first is the arrival of the reference signal at either T0 or T1 inputs, the so-called T0/T1 reset event. For such signals, the time passed since the previous reference event is recorded and the timing circuit is reset to 0. The second special event occurs in the absence of the reference pulse for more than 1074 ms, which leads to overflow of the coarse counter. In Figure 3.12 the block-scheme of time stamp generation circuit is shown.

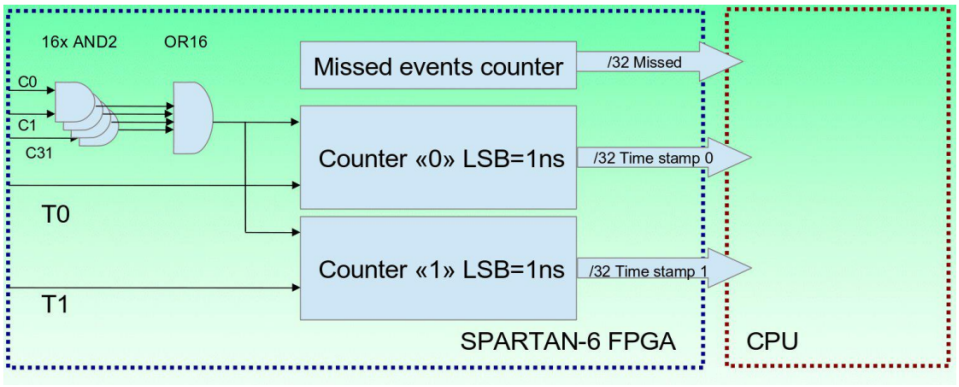

Figure 3.12: Block-scheme of time stamp generation circuit.

CITIROC

The *Cherenkov Imaging Telescope Integrated Read Out Chip* (CITIROC) is a 32 channel fully analog front-end ASIC dedicated to read-out of SiPMs. The CITIROC is the evolution of EASIROC chips and, as the name suggests, they were first developed for SiPMs used in Cherenkov imaging detectors. The processing of the analog signal takes place in the front-end channels of the device, while the read-out is handled at the internal back-end of the ASIC. Two separate electronic chains allow for high- and low-gain simultaneous processing of the analog signal. Each of the two chains, whose architecture is presented in Figure 3.13, is composed of an adjustable preamplifier followed by a tunable shaper (SSH, slow shaper), a track-and-hold circuit (SCA, switched capacitor array), and an active peak detector (PD, peak detector) to capture and hold the maximum value of a signal. Fine-tuning of each pixel gain is obtained by adjusting the voltage applied to the SiPM through an 8-bit digital-to-analog converter ranging from 0 V to 4.5 V.
The third chain implements the trigger channel generation using a fast shaper (FSB, bipolar fast shaper) with fixed shaping time of 15 ns. All CITIROC main parameters can be programmed by downloading a configuration bit string through a slow control-serial line.

3.3.2 Top CRT triggering logic

The main features of the CRT modules is determining the precise position of crossing muons. With the Top CRT modules, implementing an XY scintillator layer configuration, it is possible to obtain 64 23 cm × 23 cm coincidence of crossing strips (sectors) within each module. A possible coincidence sector is shown in Figure 3.14 at the passage of a cosmic muon. The block-scheme of the trigger formation circuit is presented in Figure 3.15. For each of the 32 channels, the CITIROC ASIC provides a charge amplifier with a configurable gain and dynamic range of 1 to 2000 photo-electrons (p.e.), the

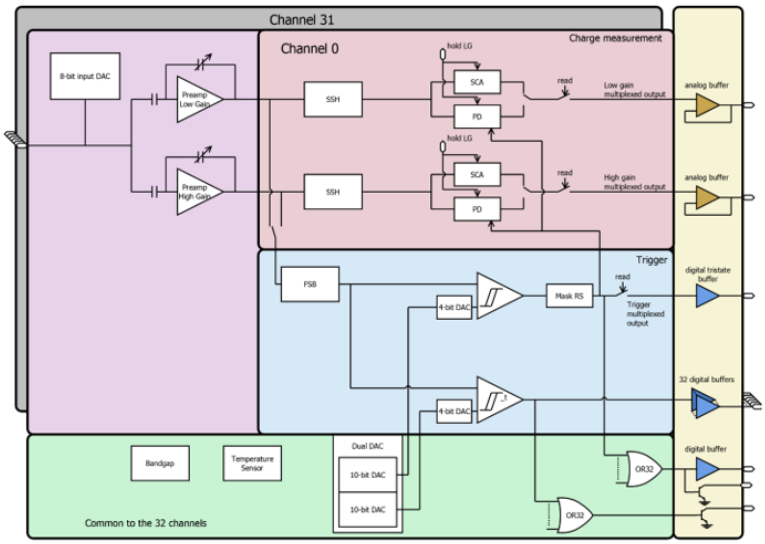

Figure 3.13: Architecture of the front-end CITIROC.

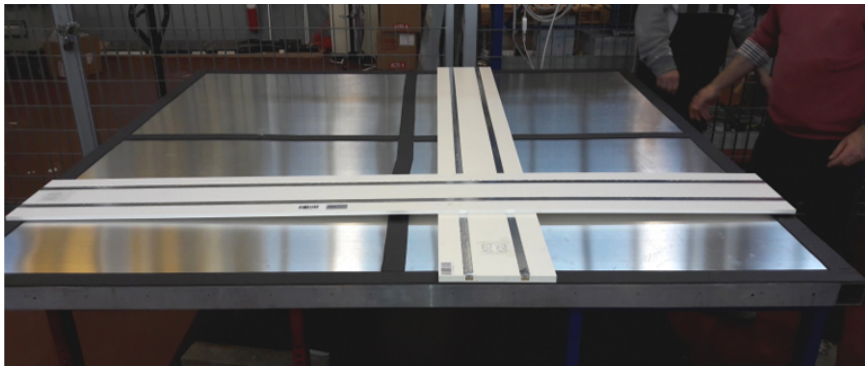

Figure 3.14: Picture of a possible geometrical coincidence of crossing scintillator strips within the Top CRT module.

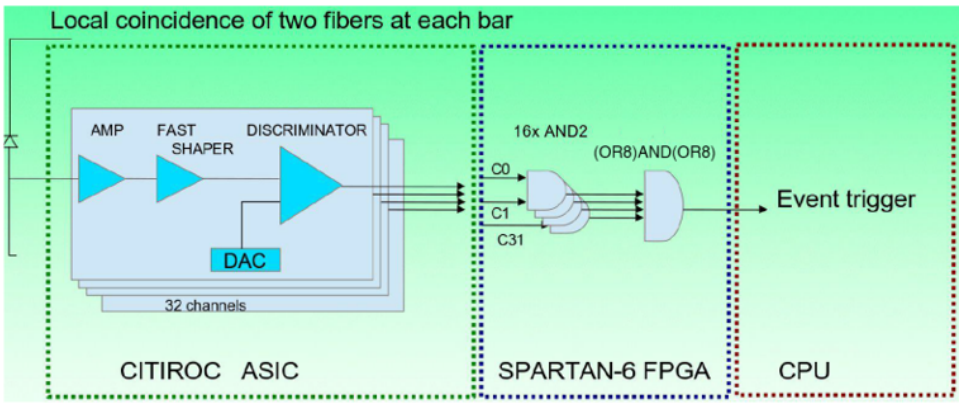

Figure 3.15: Block-scheme of the Top CRT FEB triggering circuit.

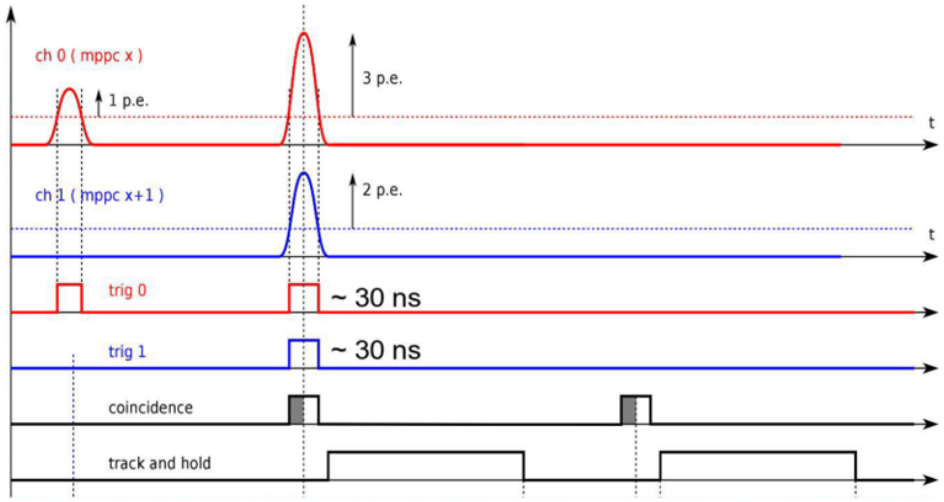

Figure 3.16: Timing diagram of the triggering circuit.

amplified signal goes through a fast shaper of 15 ns and the shaped signal is then binarized with a discriminator. The threshold for the discriminator is supplied by 10-bit DAC, common for 32 channels plus 4-bit DAC, individual for each of the 32 channels for fine-tuning. The 32 trigger signals (C0 to C31) are in LVCMOS logic (3.3 V active state) and they are routed to the FPGA where they are paired with AND logic to form coincidence signals for each of the two fibres from the same scintillator bar (coincidences of even-odd channels, e.g. $C0\&C1, C2\&C3$, ...).

The event trigger is obtained as the OR logic of the even-odd coincidence channels of a scintillator layer in AND logic with the OR even-odd coincidence of the other layer. This signal triggers the FPGA generation of the event timestamp. Each of the 32 discriminators can be individually enabled or disabled by the CITIROC configuration bit stream. The bit stream is produced by the on-board CPU on the basis of the configuration command, received via an ethernet link from the host computer. In Figure 3.16 the triggering diagram of the circuit is presented. The primary event trigger, after a delay of 50 ns, triggers an HOLD signal to store instantaneous signal levels in all 32 channels at the time of the peak maximum, and the same signal is sent to the *TOUT* LEMO connector on the FEB. The HOLD signal, which defines the read-out window of the FEB, is kept in active state for at least 150 ns. If during this period it detects high level at the input *TIN* LEMO connector of the FEB, the event is considered valid and the HOLD signal is kept high for 22 μs, until the CPU completes the digitization cycle, and reset it to its initial state. If no TIN signal is received, the HOLD signal is reset by the FPGA, and the event is discarded. TOUT is always reset to the low state after 150 ns. An additional feature of the trigger logic is the possibility of selecting an individual channel trigger where the primary event

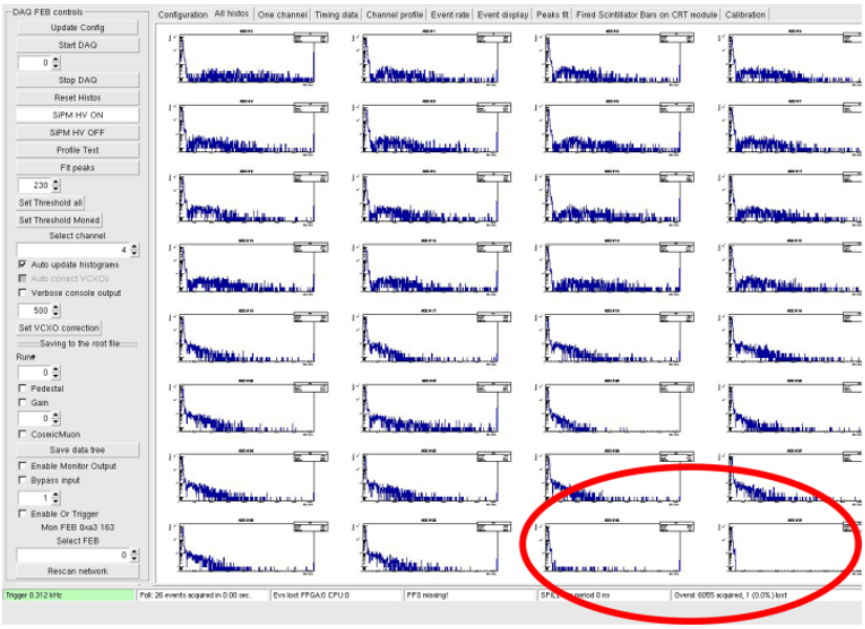

Figure 3.17: Screenshot of the channel monitor with an example of broken channel.

trigger is the OR logic of the active channels (e.g. *C0||C1||...||C31*). This feature is exploited in the Side CRT FEB triggering logic, as it is needed in order to reconstruct a signal from a long scintillator strip readout at both ends by two different FEBs.

3.3.3 Module Testing

During the construction of Top CRT modules, each of them was tested in terms of functionality and efficiency.

CRT functionality test

The functionality tests were performed using a simplified version of the data acquisition software based on the ROOT toolkit (this software is referred to as *Standalone DAQ*). An example is shown in Figure 3.17 where the electronic functionality test highlighted a faulty channel, likely due to broken SiPM or faulty FEB connection. The picture highlights a malfunctioning couple of even-odd SiPMs, where the last channel does not show signals above the channel pedestal. In such cases the module was first tested using a different FEB and, if the problem persisted, the CRT module was re-opened and the diode continuity of the SiPM was verified. Faulty SiPMs were replaced.
A second test was performed by monitoring the event rate across the module

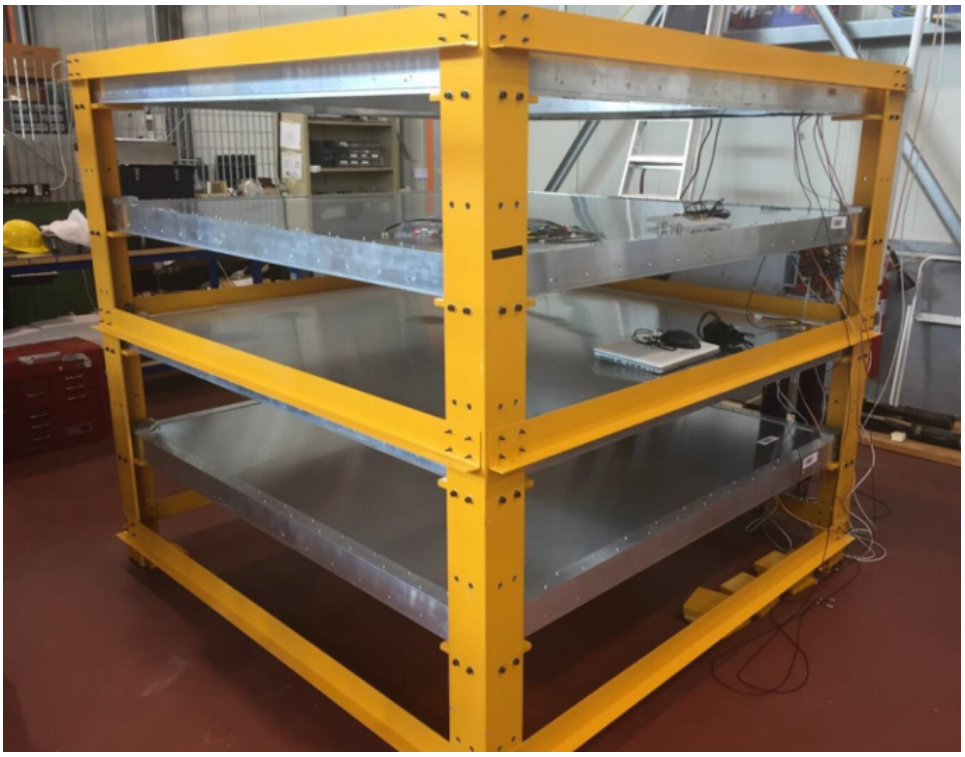

Figure 3.18: Picture of the Test Stand in the Top CRT assembly hall at LNF.

while illuminating corners and other sensitive points with a torch. If no light leakage were present, the rate of the modules was stable at ∼550 Hz, which was expected from the cosmic rays. If the rate increased while the torch was moved along the module, the possible light leakage was fixed with black tape and tested again.

Efficiency measurements

A preliminary evaluation of the CRT tagging efficiency was performed in LNF using a Test Stand (Figure 3.18). Modules were arranged on parallel planes in the rack test stand. An external trigger was obtained as the AND logic of TOUT signals of the top and the bottom modules. The external trigger was sent to the TIN LEMO connector of the tested modules and to a scaler channel in a NIM crate, to count the *external coincidences*. A AND logic of the external trigger and tested module TOUT signal was obtained and sent to another channel of the scaler to provide the *double coincidence* counts. The overall efficiency of the modules was calculated as the ratio of the *double coincidence* to the *external coincidence* counts. The sketched setup of the efficiency measurement performed at LNF is presented in Figure

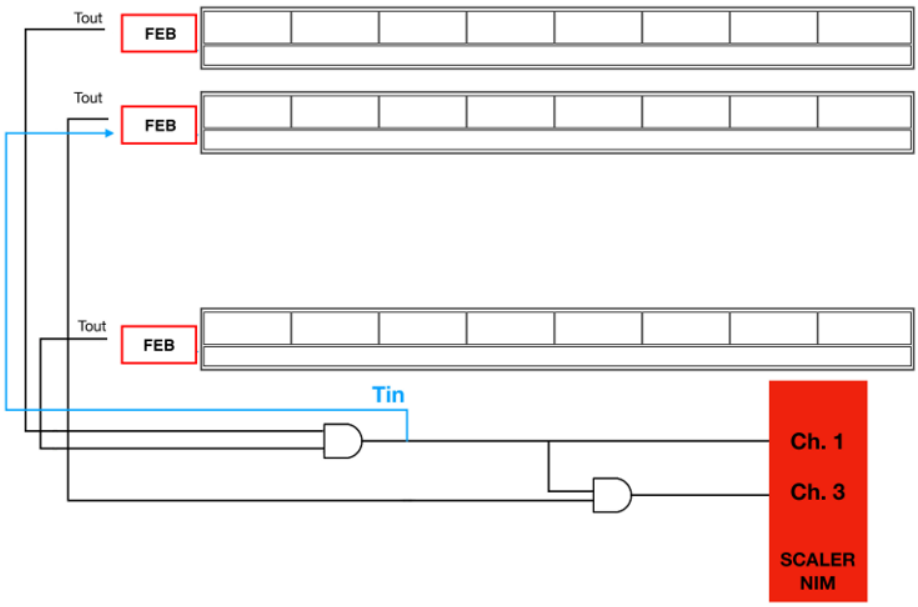

Figure 3.19: Illustration of the setup used in the efficiency measurement performed at the Test Stand in Frascati.

3.19.

The high rate of $\sim$ 600 Hz allowed to obtain a statistic of $\sim$300k events with a data taking of 10 minutes. The distribution of the Top CRT modules efficiency measured at the LNF Test Stand is shown in Figure 3.20. The average module efficiency was 96.0%.

3.4 Top CRT installation

3.4.1 Transportation to Fermilab

The construction and test of the 123 Top CRT modules (and two spares) at LNF was completed in February 2020; they were stacked in 12 racks of 10 or 11 modules each. The racks were moved inside 3 containers and moved on wheels from LNF to CERN. At CERN the racks were wrapped with protective plastic sheets. Some were tested to verify their functionality. In early 2021, the containers were shipped by cargo ship; they arrived at Fermilab in Spring 2021 and the CRT racks were stored in the warehouse. In Figure 3.21 a picture of the Top CRT modules stored inside the warehouse is shown.

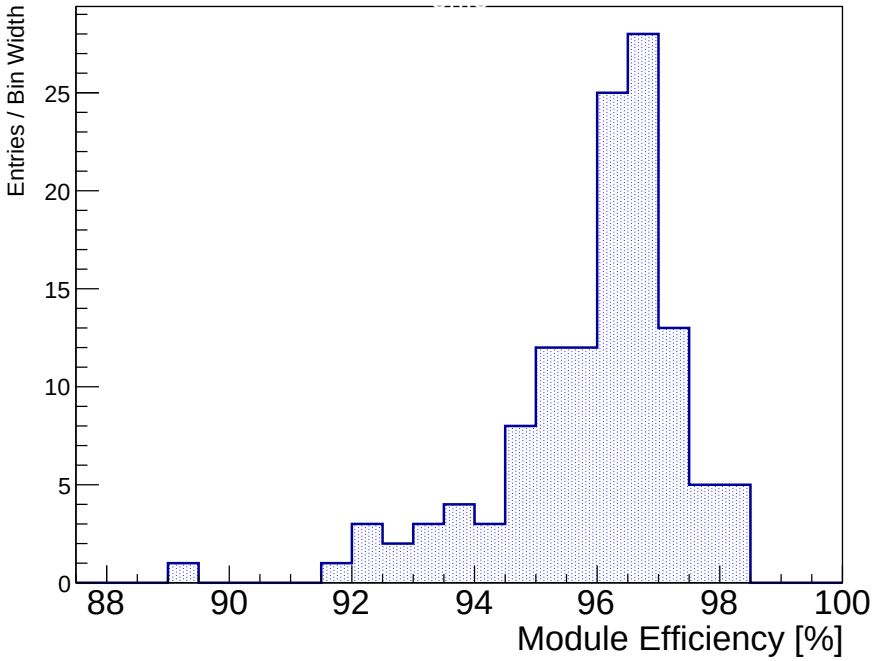

Figure 3.20: Distribution of the Top CRT modules efficiency measured at the Frascati LNF.

Figure 3.21: Picture of the Top CRT modules stored in the Fermilab warehouse.

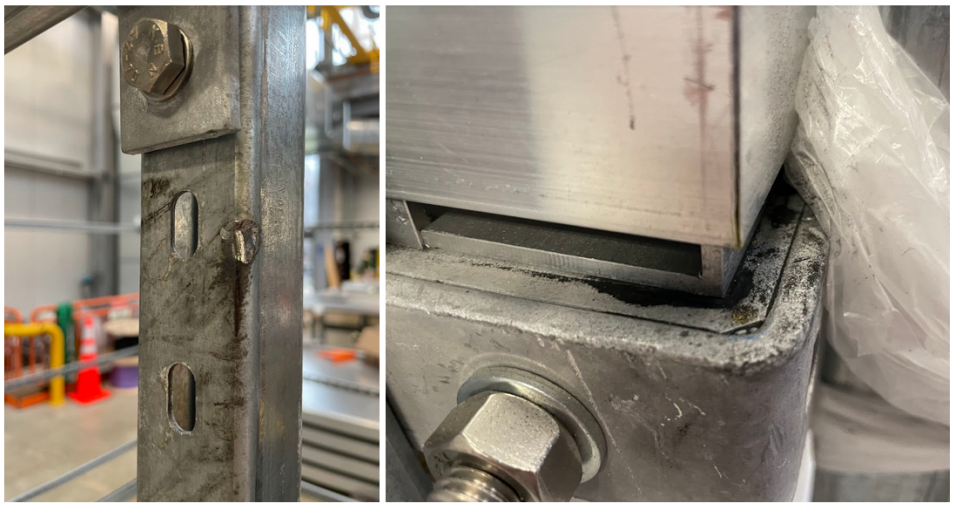

Figure 3.22: Left: detail of a dent found in one of the rack with malfunctioning modules. Right: details of black soot found on the CRT module supports of the rack.

3.4.2 SiPM replacement

Before installation, the modules were tested to verify their functionality. Unexpectedly, a large number of modules presented malfunctioning channels. After an investigation, the problem was attributed to broken SiPMs. New SiPMs were plugged in and the modules tested again, while, in parallel, an investigation started to find the cause of the damage. The broken SiPMs were tested and behaved as an open circuit. A visual inspection under microscope showed that the SiPM bonding were intact. By a further inspection, some of the racks with broken channels presented several dents accompanied by black soot and, eventually, melted-like edges, as if the structure had been hit by an electrical arc, suggesting the hypothesis of electrical damage during the transportation by ship. Another element that corroborated the electrical damage hypothesis was the presence of black soot covering all the inserts supporting the Top CRT modules, accompanied by visible discoloration of the anodization layer of the rack structure. Details of the holes in the rack and black soot are reported in Figure 3.22.
Overall, 223 SiPMs out of 4000 utilized had been found to be damaged. All the faulty devices were replaced and tested at the detector building on the far side before proceeding with the module installation.

3.4.3 Module Installation

The Top CRT modules along the vertical rims of the detector were the first ones to be installed since, following the deployment of the beams supporting

Figure 3.23: Picture of the first Top CRT module installed on top of the detector along the west vertical rim.

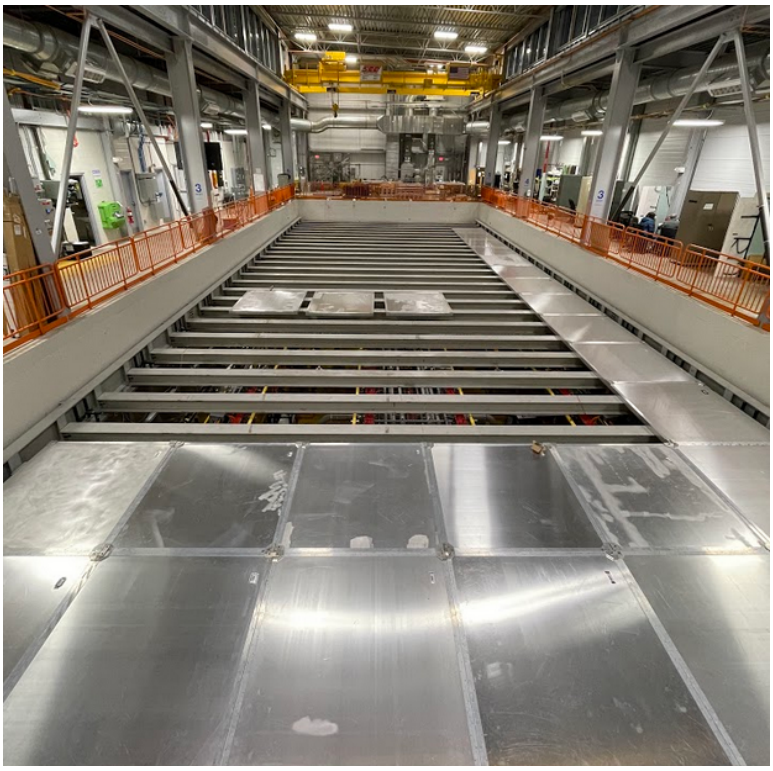

Figure 3.24: Picture of the Top CRT horizontal plane during the module installation with the supportive steel beams visible.

the horizontal CRT plane, they would have not been reachable. In Figure 3.23 a picture of the first Top CRT module installed along the west rim of the detector pit is shown. After the full installation of the 39 vertical modules located along the rims, 27 steel beams were installed to support the Top CRT horizontal plane. The CRT modules were aligned along the supportive beams and fixed one to the other by means of metal connectors which granted both rigidity to the structure and grounding connection. In Figure 3.24 a picture of the Top CRT horizontal plane during the module installation is shown, the steel supportive beams are also visible.

The full installation was completed in December 2021. In Figure 3.25 a detail of the deployment of the last Top CRT module (left) and a picture of the fully installed Top CRT subdetector (right) are shown.

3.4.4 Top CRT power distribution

The Top CRT are powered by a Wiener PL512 Modular Power Supply (PS). This unit has 12 independently controlled floating outputs. Each output in the Wiener supply is capable of providing 2-7 VDC and up to 30 A. Control of the supply is done through communication through the front-panel Ethernet

Figure 3.25: Left: details of the last installed Top CRT module. Right: picture of the fully installed Top CRT taken from the ground floor of the detector building.

connector via SNMP. The PL512 power supply contains an AC filter, power factor correction, and a primary AC-to-DC converter, as well as 6 dual power modules which down-convert the primary DC into the desired DC voltage for each of the 12 independent channels. The power supply is located inside the Top CRT utility rack and receives power from an interlock enabled Power Distribution Unit (PDU). Out of the 12 available channels, the Top CRT uses 11 channels, corresponding to 11 power distribution lines. Each channel is connected to a Power Distribution Box (PDB), which services a maximum of 12 FEBs. Figure 3.26 shows the Top CRT power distribution map with 11 lines, starting at the PS Rack and crossing the whole top area. The map ensures a small load spread, compensated for by the cables' length and relatively straight cable paths. The maximum load is about 7-8 A for 12 FEBs/line.

Low Voltage Distribution

The typical power consumption of a single CRT FEBis about 600 mA, with peaks above 700 mA, at 5 V. The power distribution line allows operating at minimal power drop and, consequently, with minimal voltage spread, keeping all the FEBs within the working voltage range (5.1 V $^{+200mV}_{-250mV}$) and granting a low ripple and noise reduction. Inside the power distribution box, a sensing line is connected to the Powerflex cable providing power to the FEBs. The interior layout of the PDB boxes is shown in Figure 3.27. Negative power lines are grounded on the CRT side. This ensures a sufficient number of ground

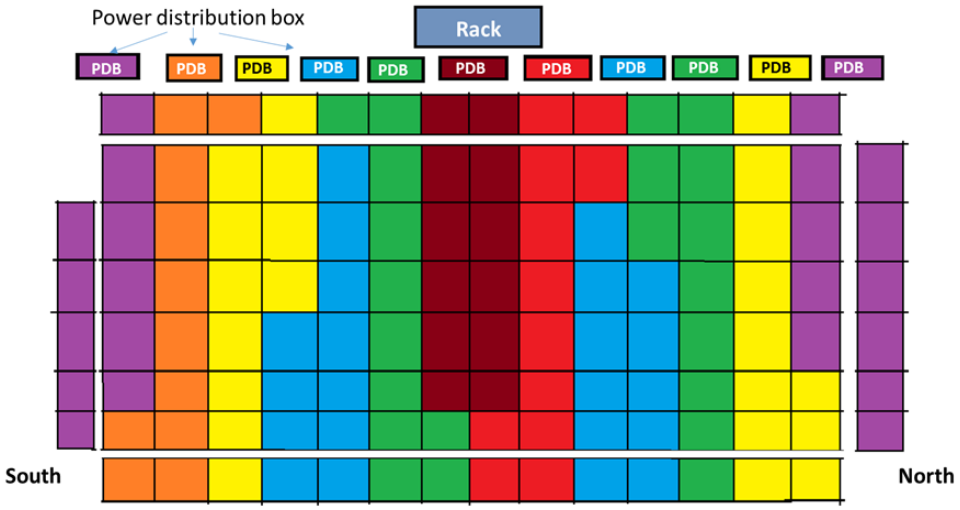

Figure 3.26: Top CRT power distribution map. Each color represent a zone/section powered on by a single power line.

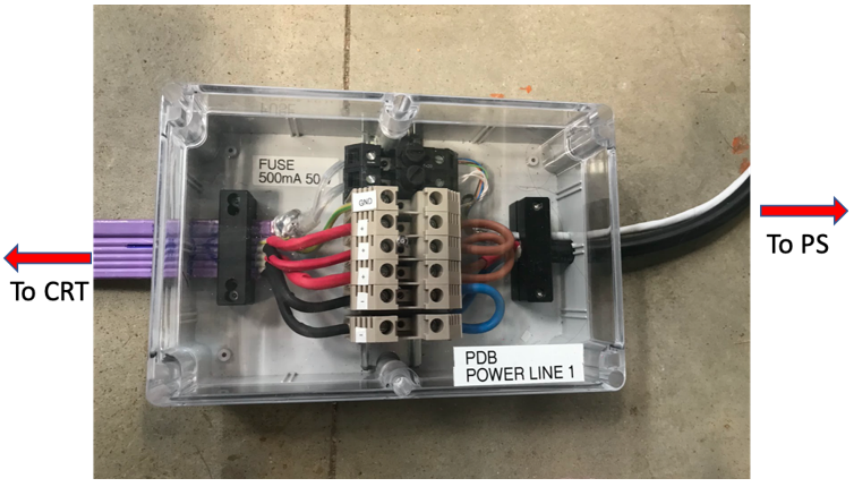

Figure 3.27: Power distribution box, mounting details.

Figure 3.28: Left: picture of a single powe line used to power on the first line of the Top CRT system. Center: picture of the adapters to power on a pair of FEBs, with the addition of ferrite with 4 winding on both wires used for noise filtering. Right: details of the inside of one of the plugs used to power on two CRT modules.

connections (11/12/line) to the CRT ground reference plane, all modules being electrically coupled to their neighbors and subsequently grounded to the hall reference. To minimize the possible effect of small local loops, the power cable to each FEB are instrumented withe ferrite rings. Locally, at the CRT-FEB side, the negative grounding is provided by 4 connections.

Figure 3.28 shows details of the Top CRT power distribution lines: the whole line (left), the adapter to power two modules (center) and details of the adapter plug.

3.4.5 Data Distribution Lines

The Top CRT modules are arranged into 8 different data lines, as illustrated in Figure 3.29, and connected to two different Servers, each with 4 available Ethernet ports. Data lines from 1 to 4 are connected to the first server, and those from 5 to 8 are connected to the second. Data lines 2 to 7 are made of up to 14 modules, while the first one has 18 modules, and the last one has 19 modules. The modules in each data line are daisy chained one to the other through the double Ethernet port in each FEB. The Ethernet cables used for the daisy chain are 3 m long shielded cables, while those used to connect the first module of each line with the corresponding server port are 30 m long unshielded data cables, to isolate the Top CRT modules ground from the server one.

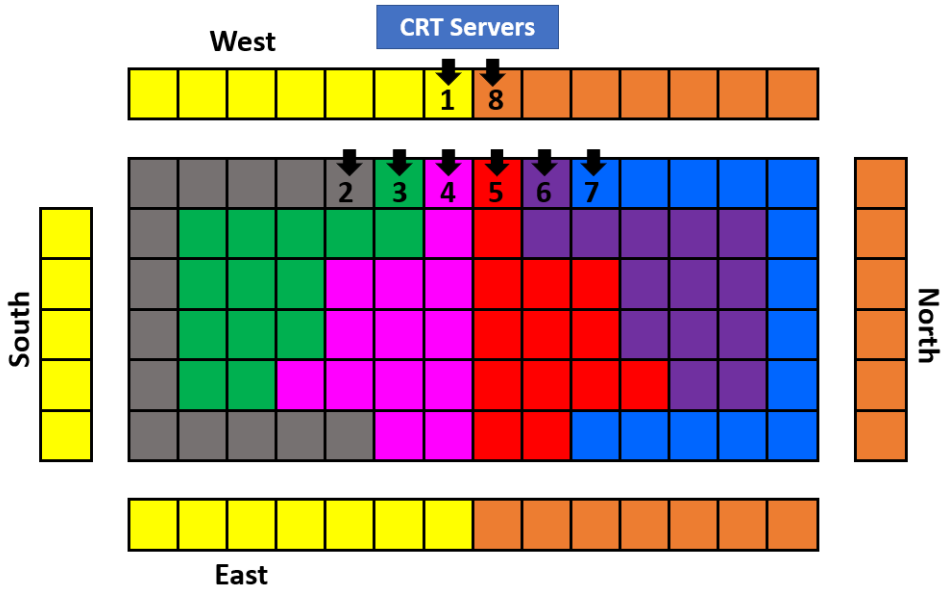

Figure 3.29: Top CRT Data distribution lines. Each color correspond to a different Top CRT data line. Black arrows correspond to the first module of each line.

3.4.6 Timing Lines

The CRT timing distribution chain is made up of two different timing lines:

- T0 line, along which the PPS signal is propagated;
- T1 line, along which the global trigger signal is propagated, see section 4.5.

Both the T0 and T1 lines are propagated to the Top CRT modules through a Timing Distribution Unit (TDU), Figure 3.30 .

T0 line

The PPS signal is generated by the SPEXI board inside the trigger utility rack and sent out through a lemo cable to a Fan Out where it is distributed to the three different CRT subsystems (Top CRT, Side West CRT and Side East CRT). The output signal of the Fan Out is converted into an optical signal by means of an electrical-to-optical converter and propagated along an optical fiber to the CRT TDUs. Inside the TDU, the optical signal is converted into an electrical signal by means of an optical-to-electrical converter, and the output signal is then propagated via lemo cables to two different fan-outs, each with twelve available lemo outputs. The PPS signal is then propagated to each CRT distribution lines. The scheme of the PPS distribution along

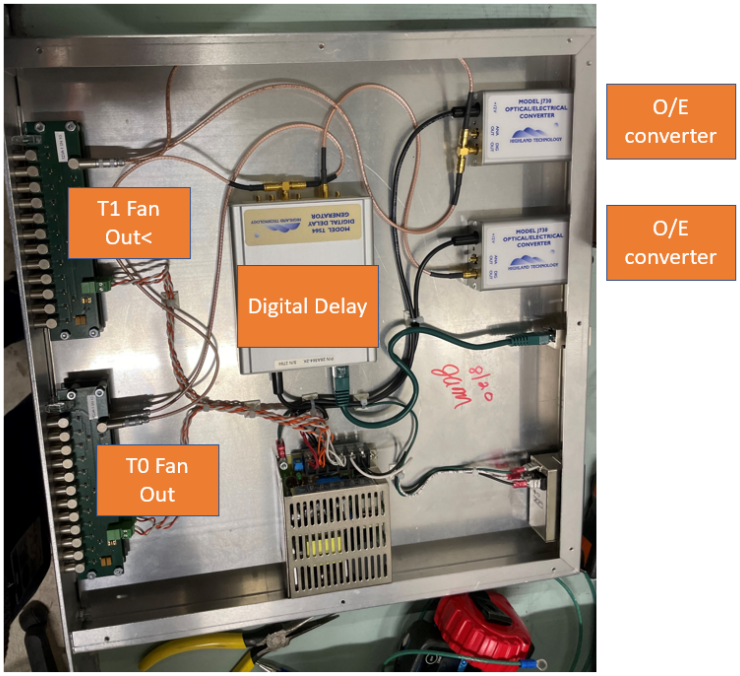

Figure 3.30: Picture of the Top CRT Timing Distribution Unit with its components.

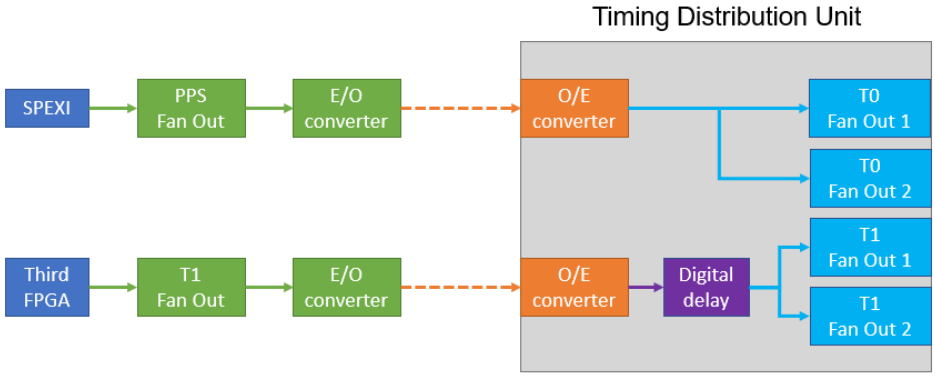

Figure 3.31: Scheme of the timing signal propagation for the PPS (top line) and the trigger signal (bottom line).

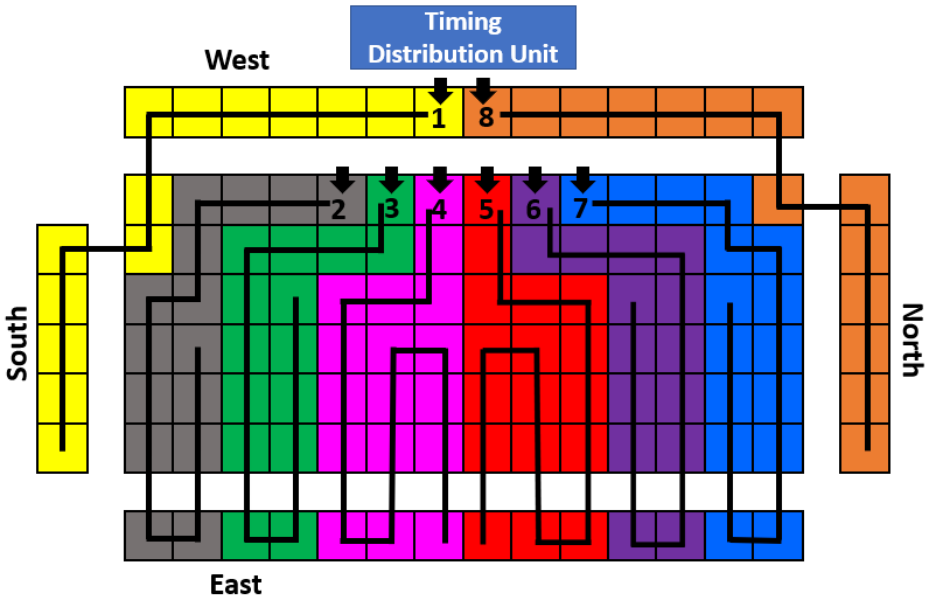

Figure 3.32: Top CRT Timing lines. Each color corresponds to a different Top CRT timing line. Black arrows correspond to the first module of each line.

the T0 timing line is shown in Figure 3.31. Each timing line is a *bus* of lemo cables connected via a Y connector plugged into each of the Top CRT FEBs T0 port at every step of the chain. The first FEB of each timing line is connected to the Top CRT TDU with a combination of long lemo cables (nominally 60 ns long) and short lemo cables (nominally 16 ns). From the first module of each line, the following FEBs are connected with a short lemo cable at each step of the chain. The last module of each chain is connected by a Y connector, but one end is terminated with 50 Ω plugs. The Top CRT modules were arranged into eight different timing distribution lines according to the map reported in Figure 3.32.

T1 line

The global trigger signal is generated by an FPGA located in the trigger rack when the required triggering logic is fulfilled. The electrical signal is then propagated along the T1 timing distribution line. The signal is first sent to a dedicated Fan Out and then distributed to the three different CRT subsystems (Top CRT, Side West CRT and Side East CRT). Analogously to the PPS, the global trigger electrical signal is converted into an optical signal and propagated through an optical fibre paired to the one used in the T0 line. The optical signal is converted into electrical signal inside the TDU and sent to a digital delay. The delayed signal is then propagated via lemo cables

to two Fan Outs similar to those used for the T0 line. The distribution of the global trigger signal along the T1 timing line is presented in Figure 3.31. The timing lines used for the T1 signal are the same as those described in the previous section, with the difference that the Y connectors are plugged in the T1 lemo port of the Top CRT FEBs.

Chapter 4

Top CRT Commissioning

The Top CRT installation was completed by mid December 2021. Starting from January 2022, the subdetector started its commissioning phase, which I performed during my period as Run Coordinator of the ICARUS experiment from February to May 2022.

4.1 Data taking

The ICARUS data acquisition (DAQ) system is based on the *artdaq* data acquisition software development framework, providing customizable applications for reading data from detector elements (*BoardReaders*), and configurable applications for performing event/building, data-logging, and data-dispatch to downstream online data quality monitoring processes. The BoardReaders acquire data fragments from the TPC, PMT, and CRT readout electronics, and from the trigger and White Rabbit timing systems. They then assign appropriate event counters and timestamps to each fragment and then queue those data for transfer to a configurable number of *EventBuilder* applications. For each triggered event, the ICARUS trigger BoardReader sends its data fragment to an EventBuilder, triggering a request for data from all other configured BoardReaders in the DAQ system. Depending on the trigger type (BNB, Offbeam BNB, NuMI, and Offbeam NuMI), data are written in separate file streams. The DAQ system is capable of supporting trigger rates up to 5 Hz, although the expected trigger rates are $\sim$ 1 Hz.

The Top CRT was integrated in the detector data-acquisition using the same format of the Side CRT. Unlike TPC or PMT, for which the digitizers require an external trigger to collect the waveforms, the CRT FEBs are in auto-trigger mode. Each Top CRT data line is read out by the corresponding Top CRT DAQ server, which performs a polling of the line every 80 ms, fragments within the time window of the triggered event are saved (*window mode*).

A preliminary configuration with the Top CRT data lines was tested in

a different DAQ working area using a software 10 Hz trigger. After some proper tuning of the DAQ parameters (e.g. expected fragment size, number of event builders, time window, ...) and the upgrade of the firmware of the FEBs, to correct for the so-called "time-spikes" described in the next section, the Top CRT modules were fully integrated in the detector data acquisition in march 2022. In order to increase the statistic of CRT Hits, mainly for calibration purposes, the acquisition window for the Top CRT was set to $\pm$ 25 ms w.r.t. trigger timestamp. The window is extremely larger than the $\sim$ 2 ms drift window of the TPC, this is why the CRT hits sample of the 50 ms window is used only for calibration purposes, the normal data flow of event reconstruction uses a software reduced window of $\pm$ 3 ms.

Differently from the Side CRT, for which all the FEBs use the same configuration, for the Top CRT each module is configured using the parameters proper of each channel. During the construction of the Top CRT modules, a database was created to record the channel-SiPM map. For each SiPM the corresponding nominal operation bias voltage was saved in the database, accompanied by the bias voltage set on the FEB. The latter value was first set on the board using the dedicated trimmer and then its stability was verified after 30 minutes of operation. Using the dedicated 10-bit DAC (up to 5 V), each channel/SiPM can be set to the desired overvoltage due to the known difference between the FEB voltage and the SiPM breakdown voltage. For each Top CRT module, a configuration file including channel-to-channel bias correction (after a proper conversion in the 10-bit format of the DAC) and threshold (set to 1.5 photo-electrons for all the channels) was produced. At the beginning of each run, the correct configuration is loaded in every FEB, this granted a more uniform gain/bias distribution across all the modules.

4.1.1 FEB testing and firmware upgrades

CAEN A1702 FEB assigns a ns timestamp to each trigger it produces. Typically, either with a cosmic induced trigger or generated artificially by resetting the clock, the timestamps gradually increases up to 1 s, and then start from 0 again. Following several tests, it was observed that the timestamps do not increase monotonically. Figure 4.1 shows the trigger timestamps over time for one specific FEB using the standalone DAQ. Clear *spike*-like structures can be seen in the plot of the timestamps over time.

It was observed that this unwanted feature originates in the original firmware of the LPC4370 ARM MicroController used in the CAEN A1702 FEB. The LPC4370 has a dual-core, shared memory architecture and during the buffer readout, both cores were reading and writing a particular memory location, used as a count of active events. One core was reading-incrementing-writing that location, while the other was reading-decrementing-writing. Both cores were doing the same operations at the same time. For a fraction of the time, there was a conflict in which the value written by one

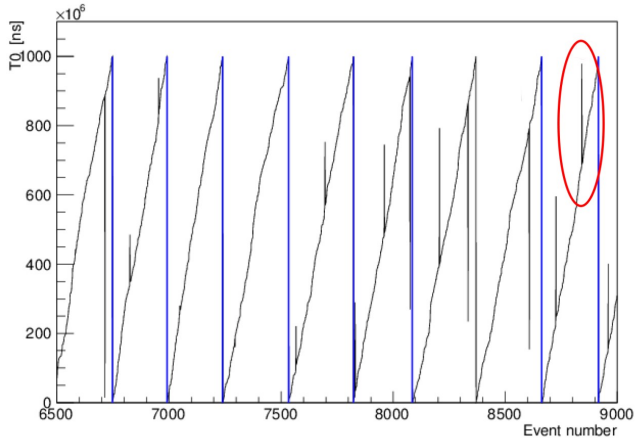

Figure 4.1: Timestamps vs the event number before the Micro-Controller firmware update. Blue lines correspond to reconstructed special reset events. Red circle highlight a so-called *spike*.

core overwrote the necessary value written by the other core. Incrementing and decrementing of the same memory location could work if the operations were atomic, however the Micro-Controller inside the LPC4370 does not support these atomic operations for both cores (SBN internal document, [63]). A fixed firmware was developed in order to use two memory locations, instead of the one previously described. Each location is exclusively written by one core, while the reading can be performed by both. The new firmware for the Microcontroller was first tested on one spare module, and then, once verified that it did not corrupt the data, it was updated on all the Top CRT FEBs, using the standalone DAQ.

A second problem was observed when digitizing a special reset event of the T0/T1 counters: not all reset events were correctly identified as special events, but despite correctly resetting the corresponding counter, they were treated as regular hits. The *special* event qualifier is assigned to a CRT Hit as a bit mask and it was assigned a *flag* variable. In Figure 4.1 it can be seen that, in correspondence with the reset of the counter value, a *special flag* is generated (positioned as a blue line), but in one case (event number $\sim$ 8400), this did not happen. It was empirically observed that the correct reset event is generated in average 65% of the times. As it will be described in section 4.2, the special reset events are an important feature which can be exploited to improve the whole CRT timing resolution. This bug did not affect the effectiveness of the data-taking, therefore it was possible to move on with the CRT implementation; a possible fix has been developed by the CAEN engineers, and a new firmware is currently under test.

4.2 CRT Timing

The $\sim$ ns resolution in the CRT timing, needed for an effective cosmic background rejection, can be achieved only by accounting for all the possible delays in the CRT T0 and T1 timing lines. During the Top CRT commissioning, an accurate delay measurement campaign was performed.

4.2.1 The two-ways technique

The delay measurements for T0 and T1 were performed using a two-way technique, using the paired and equal optical fibers that distribute the T0 and T1 signals to the CRT TDU; for the Top CRT, the paired optical fibers were 120 feet long. The two way technique is performed by setting up a second path to transmit the signal from the trigger rack, to the CRT TDU (t_A) and backwards (t_B); when measuring the T0 (T1) delay, for the second path, the signal was sent from the TDU backwards to the trigger rack through the T1 (T0) optical fibre. The two-way method consists of measuring the propagation time of the signal along the sum of the two paths ($TSUM = t_A + t_B$) and then the difference in time to propagate the signal along the two paths ($TDIFF = t_A - t_B$), as shown in Figure 4.2 and Figure 4.3 for T0 and T1, respectively. The signal propagated in the delay chain was generated from a pulse generator and the measurement of *TSUM* and *TDIFF* was performed by by means of a Tektronix MSO58 oscilloscope (500 MHz and 6.25 GS/s), using the delay measurement tool between the rise edge of the two signals. While performing he measurement, the two cables used to connect the oscilloscope are of the same length, therefore they are compensated. From TSUM and TDIFF we obtain t_A and t_B using the following equations:

$$t_A = (TSUM + TDIFF)/2$$

$$t_B = (TSUM - TDIFF)/2$$

Although the two paths were fairly similar, as described in Figure 3.31, at the time of the T0 delay measurement, the Side CRT was in data collection; therefore, we had to exclude from the A path the delay induced by the PPS FanOut. This was measured afterwards during a scheduled downtime of the DAQ. The delay measurement campaign along the T0 line was performed in February 2022 and the results are reported in Table 4.1. The missing delay

TSUM	393.8 $\pm$ 0.1 ns
TDIFF	7.6 $\pm$ 0.1 ns
t_A	200.7 $\pm$ 0.1 ns
t_B	193.1 $\pm$ 0.1 ns

Table 4.1: Delay measurements along the T0 line according to Figure 4.2.

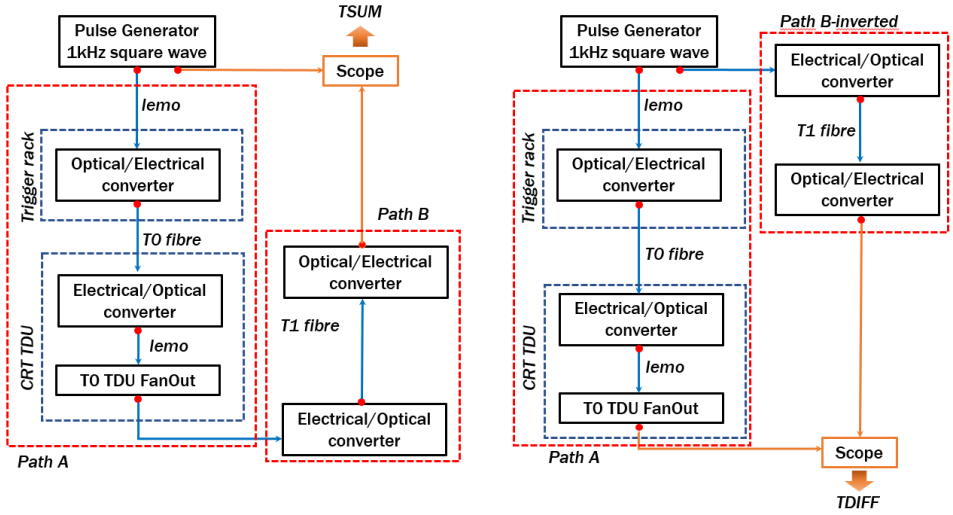

Figure 4.2: Measurement of T0 propagation using the two-way technique. Left: delay between a signal output from a pulse generator through T0 and the same signal sent back through path B (TSUM). Right: difference between the time delays along the T0 line and along the inverse path B (TDIFF).

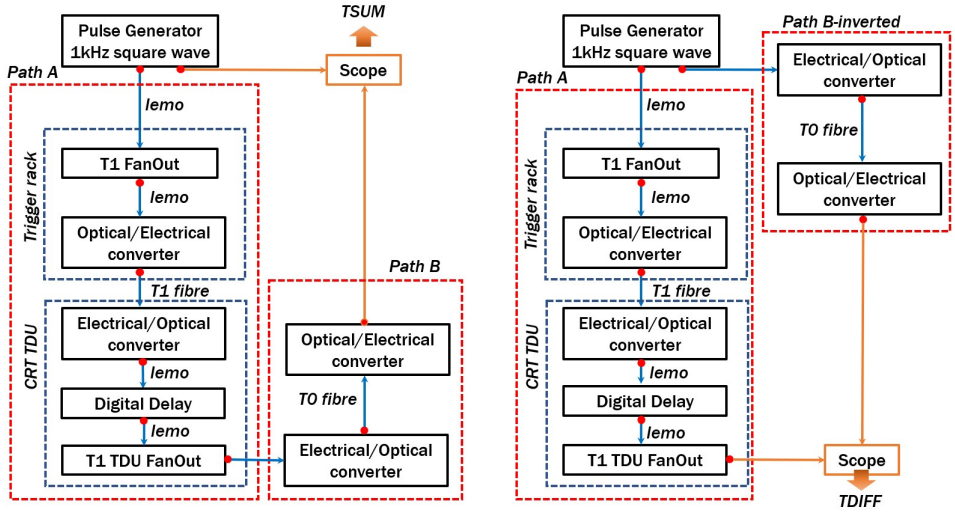

Figure 4.3: Measurement of T1 propagation using the two-way technique. Left: delay between a signal output from a pulse generator through T1 and the same signal sent back through path B (TSUM). Right: difference between the time delays along the T1 line and along the inverse path B (TDIFF).

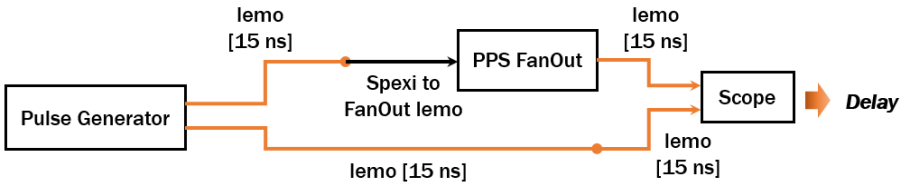

Figure 4.4: Schematic of the delay measurement between the SPEXI output and the PPS FanOut output.

TSUM	455.8 ± 0.1 ns
TDIFF	45.7 ± 0.1 ns
t_A	250.7 ± 0.1 ns
t_B	205.1 ± 0.1 ns

Table 4.2: Delay measurements along the T1 line according to Figure 4.3.

measurement between the SPEXI output and the PPS FanOut output was performed as illustrated in Figure 4.4. The result was an additional delay (t_{FO}) of 23.6 ± 0.1 ns. The overall delay measurement along the T0 line from the trigger rack to the Top CRT TDU was evaluated as

$$\Delta t_{T0} = t_A + t_{FO}$$

resulting in $\Delta t_{T0} = 224.3 \pm 0.2$ ns, but, due to limitation in sub-ns processing of timestamps inside the Icaruscode software, it was considered 224 ± 1 ns.

The measurement of the delay along the T1 line needs further considerations, the main difference w.r.t. T0 being the presence of a digital delay. As described in section 3.3.2, whenever the CRT FEB produces a trigger, a dead time of 22 μs is generated. The T1 line propagates the global trigger signal to be used as an additional and precise timing reference appropriate to each event acquired by the TPC. The acquisition of T1 generates a trigger in the FEB, which generates a special event. This special reset event induces a 22 μs dead time as real events. Without a proper handling of the global trigger logical signal, a 22 μs dead-time window would be present in TPC drift window. This problem can be solved by delaying the global trigger signal by such a large amount that the dead-time window occurs after the full TPC readout. The delay agreed upon was, conservatively, 2 ms (t_{DD}). To perform the delay measurement along the T1 line as illustrated in Figure 4.3, due to limitations in the oscilloscope sensitivity at the $\sim$ ms scale, while performing the measurement, the digital delay was set to 0. The manufacturer reported an intrinsic 21 ns delay, even with no digital delay set; this is included in our measurement. The results of the delay measurement along the T1 line are reported in Table 4.2. The t_A measurement for T1, already included the delay

induced from the lemo connector to the third FPGA (which sends out the global trigger signal) and from the FanOut. The overall delay measurement along the T1 line was evaluated as

$$\Delta t_{T1} = t_A + t_{DD}$$

where t_{DD} is the value set on the digital delay, 2 ms, for which the manufacturer reported an accuracy of 1 ppm, corresponding to an error of ± 2 ns. The resulting delay along the T1 line is 2000251 ± 3 ns. The 1-ppm accuracy in the digital delay will be improved in the upcoming future by measuring the digital delay with an oscilloscope capable of resolving the nanosecond delay in a millisecond scale time window.

4.2.2 Time propagation delay along the distribution lines

The Top CRT timing distribution lines were illustrated in Figure 3.32 and described in Section 3.4.6. Due to the inaccessibility of many of the FEBs, once the modules were installed, the delays introduced by the lemo cables between the Top CRT TDU and each module were estimated by design and precisely measured only for the first FEB of each timing line. The delays of the subsequent modules were estimated considering the addition of one 3 m long lemo cable at each step of the line. Using an oscilloscope, the average delay introduced by one 3 m long lemo cable was 15.3 ns, measured over a sample of $\sim$ 30 spare cables. The resulting delays per module have been reported in Table 4.3 along their respective position on the different timing distribution lines. The reported values are rounded to nanoseconds and, conservatively, an error of ±1 ns is assumed per module. Since the cables used for the T0 and T1 bus were chosen to be equal in length, the values reported in Table 4.3 refer to both.

The total delay for each module along T0 (Δt_{T0i}) and T1 (Δt_{T1i}) were evaluated as

$$\Delta t_{T0i} = \Delta t_{T0} + \Delta t_i \tag{4.1}$$

$$\Delta t_{T1i} = \Delta t_{T1} + \Delta t_i \tag{4.2}$$

respectively, where Δt_i is the delay value of the i-th module along its timing distribution line obtained from Table 4.3.

4.3 CRT calibration

After the Top CRT was included in the data acquisition, a data collection campaign was carried out to estimate the pedestal and gain values of each Top CRT channel. The pedestal and gain values can be obtained by fitting the integrated ADC charge spectrum of each channel, exploiting the feature that at each trigger the FEB store the ADC value of each of the 32 channels.

Timing line/ position in the line	*1*	*2*	*3*	*4*	*5*	*6*	*7*	*8*
1	58	73	74	59	59	74	118	59
2	74	89	89	75	74	89	133	75
3	89	104	105	90	90	105	149	90
4	104	119	120	105	105	120	164	105
5	120	135	135	120	120	135	179	121
6	135	150	151	136	136	151	195	136
7	150	165	166	151	151	166	210	151
8	165	181	181	166	166	181	225	166
9	181	196	196	182	182	196	240	182
10	196	211	212	197	197	212	256	197
11	211	226	227	212	212	227	271	212
12	227	242	242	228	227	242	286	228
13	242	257	258	243	243	258	302	243
14	257	272	273	258	258	273	317	258
15		288	288	273	273	288	332	
16				289	289		348	
17				304	304			

Table 4.3: Measurement of the delay in nanoseconds between the TDU of the Top CRT and each module along the eight different timing lines. The reported values have been rounded to the ns and the relative uncertainty depends on the the module position along the timing line, adding up to $\sim$ 4.5 ns for the last modules of the longer lines.

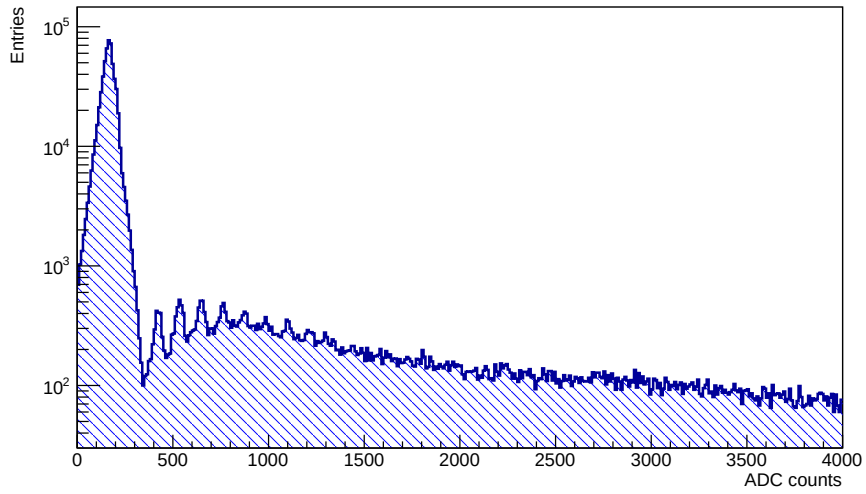

Figure 4.5: ADC counts distribution for a channel of a 10 mm scintillator bar of one of the Top CRT modules.

The pedestal was initially obtained by fitting with a gaussian distribution the ADC spectrum of a channel when it did not participate in the CRT hit channel coincidence. The gain was obtained as the average distance between the quantized photoelectron peaks in the integrated charge spectrum of cosmic muons. Quantized photoelectron peaks were fitted by using multiple Gaussian peaks.

In Figure 4.5 a typical distribution for one Top CRT channel corresponding to one 10 mm thick scintillator bar is shown, while in Figure 4.6 the same distribution for a channel of corresponding to a 15 mm scintillator is also shown. The single photoelectron peaks are visible, but the distribution shows a very large pedestal. To properly fit pedestal and gain, for each channel, we selected two diffrent samples: a random trigger (for pedestal) and triggering channels (for gain). The Top CRT FEB firmware currently does not provide the list of the channels that participate in the CRT triggering coincidence, but this can be obtained with good approximation by software identifying two consecutive channel above threshold in both the scintillator layers.

4.3.1 SiPM gain evaluation

An example of the ADC charge distribution spectrum for a Top CRT channel involved in the CRT triggering coincidence is presented in Figure 4.7 and corresponds to a 10 mm scintillator. Peaks were first identified using the TSpectrum class provided by ROOT[64]. The first identified 5 peaks

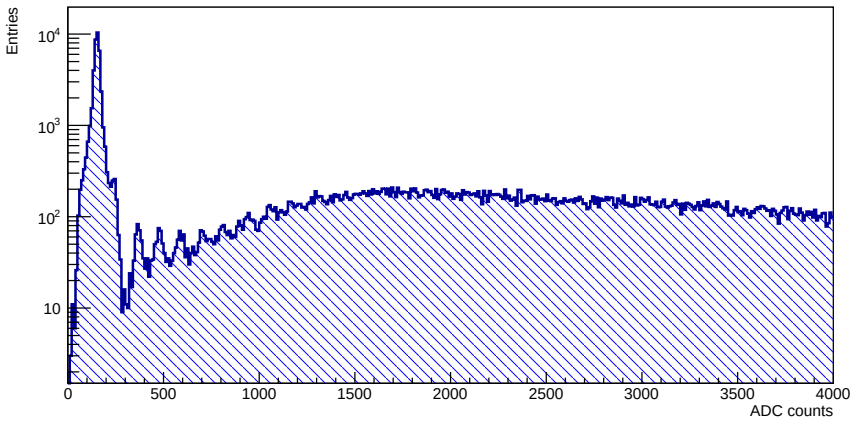

Figure 4.6: ADC counts distribution for a channel of a 15 mm scintillator bar of one of the Top CRT modules.

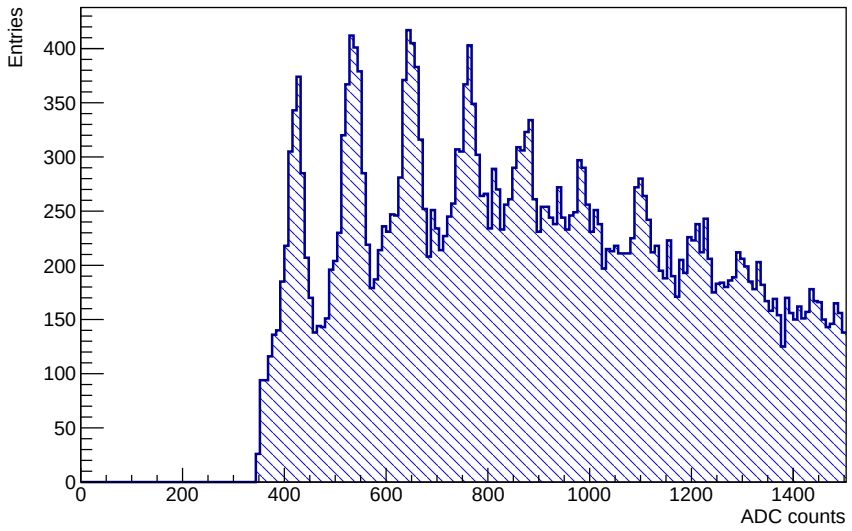

Figure 4.7: ADC counts distribution for a channel corresponding to a 10 mm scintillator bar when the channel is part of the CRT triggering coincidence. The spectrum is zoomed in the region below 1200 ADC to enhance the visibility of the single photoelectron peaks.

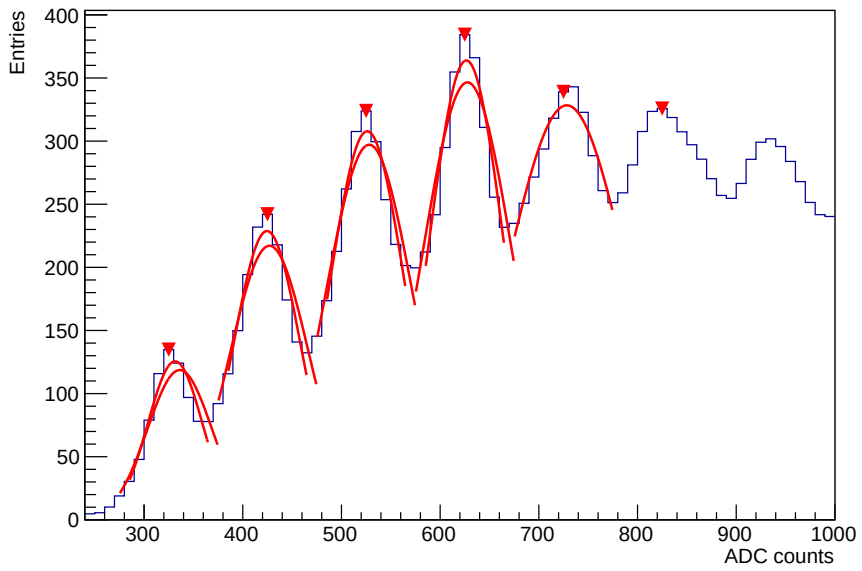

Figure 4.8: Recursive single photoelectron peaks fitting with a gaussian distribution for a 10 mm scintillator channel when participating in the CRT triggering coincidence. The pedestal is not shown and the left peak corresponds to 2 p.e.

were fitted using Gaussian distributions. For each fit, the minimum distance between the previous and the following peaks was used as the range; recursively, the range was reduced and the fit was repeated until the reduced χ^2 (χ^2_ν) was < 8, or until there were no more bins in the selected range. In Figure 4.8 a distribution of the charge spectrum for a 10 mm scintillator channel is shown with overlayed the recursive gaussian fit of the first 5 photoelectron peaks. The mean values of the peaks, resulting from the gaussian fit, were plotted versus the corresponding peak number, the gain was extrapolated as the slope of a linear fit of the distribution. In Figure 4.9 an example of a gain fit for a channel corresponding to a 10 mm scintillator is shown.

The gain fitting algorithm was run on all the working channels of the Top CRT modules. The distribution of the resulting gains is reported in Figure 4.10, the average gain value is 103 ± 10 ADC per photoelectron peak. some of the outliers were analyzed and it was observed that, especially for the 15 mm scintillators, some peaks were misidentified with others, therefore introducing errors in the fit. Future updates are foreseen to improve the gain fitting algorithm and further reduce the number of the outliers.

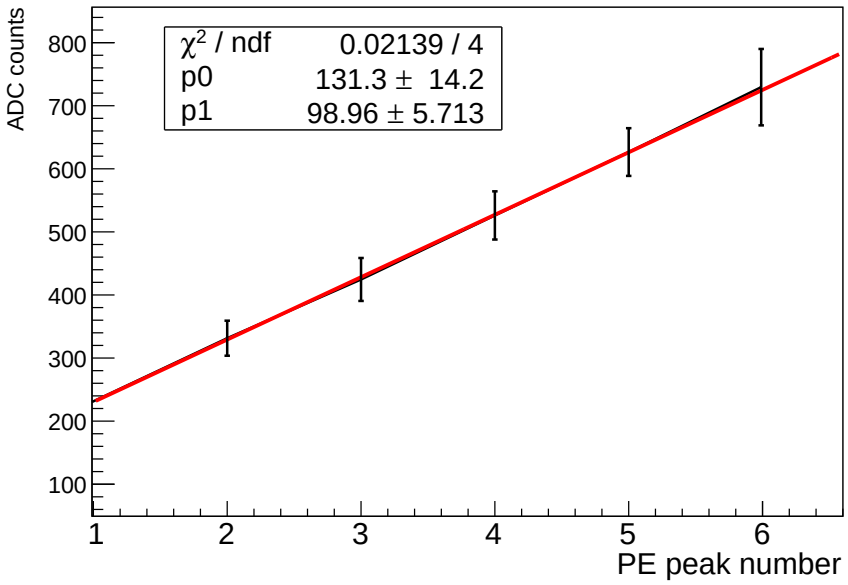

Figure 4.9: Distribution of the photoelectron peaks mean value versus the corresponding number, fitted using a linear fit to evaluate the gain from the slope of p.e. Error bars represents the sigma of the Gaussian fit for the corresponding peak.

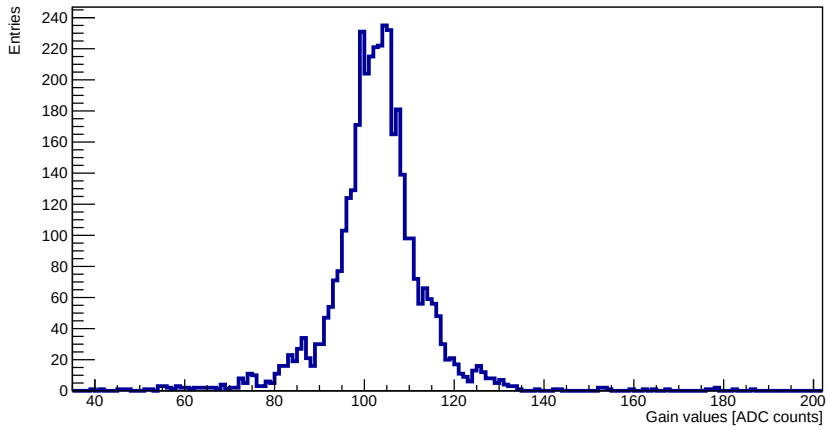

Figure 4.10: Distribution of the gain of all the channels of the Top CRT modules.

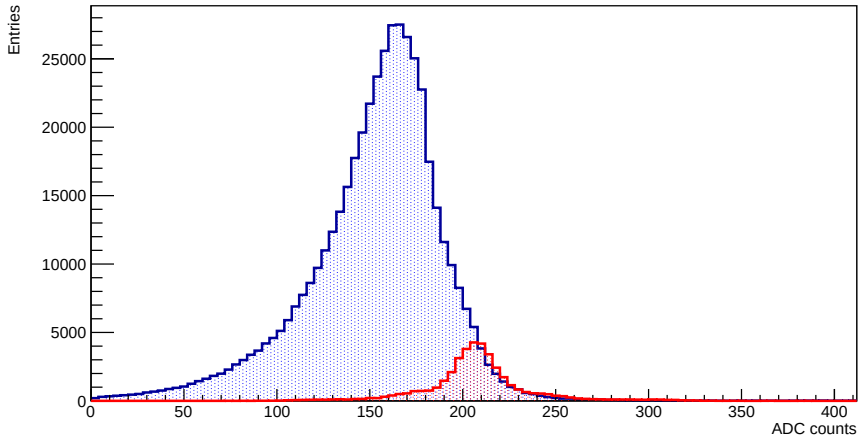

Figure 4.11: Comparison of pedestal distributions when the channel does not participate in the CRT triggering coincidence (blue) and when the board receives an external random trigger (red) for a channel of one Top CRT module.

4.3.2 Top CRT pedestal fit

In Figure 4.11 (blue) the ADC charge distribution for a channel corresponding to a 10 mm scintillator bar is shown when it is not involved in the coincidence that triggers CRT. The distribution of the pedestal is larger then the distance between the p.e. peaks. This behaviour is not suitable to correctly estimate the waveform baseline for the pedestal. By definition, random triggers of the CRT FEB should result in random values of each channel around its pedestal. Using the same dataset and exploiting the T1 and T0 special reset events which behaves as an external random trigger, a new sub-sample with a reduced statistic was obtained. In Figure 4.11 (red) the charge spectrum distribution of the same channel applying the selection of external random triggers is shown. The new distribution shows a Gaussian-like structure and the resulting peak is located at higher ADC values with respect to one selected from the non-triggering channels.

This effect was not observed in the Side CRT distributions. In the Side CRT case, out of the 32 channels, only one is supposed to be above threshold, while in the Top CRT, this is true for at least 4 channels. The FEBs were originally designed to work in a Side CRT-like scenario, while the requirement of 4 channels above threshold for the Top CRT could affect the FEB electronic. This effect is still under evaluation and it seems to be correlated with the amplitude of the triggering channels; additional tests are in progress.

However, the subsample obtained by using the external random trigger

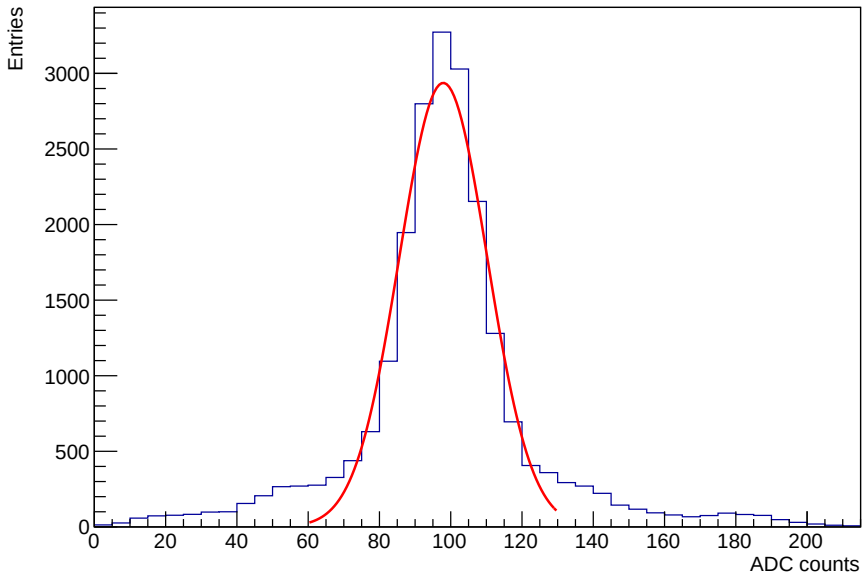

Figure 4.12: Pedestal fit for a channel corresponding to a 10 mm scintillator using a sub-sample of hits triggered by a random external trigger. The pedestal was fitted with a gaussian distribution.

was considered to be more suitable for the pedestal evaluation, which, following the same procedure described in the section dedicated to the gain fit, was obtained by a recursive Gaussian fit. In Figure 4.12 the result of a gaussian fit of the pedestal for a channel corresponding to a 10 mm scintillator is shown. The distribution of the pedestal distribution for all the Top CRT channels is presented in Figure 4.13.

4.4 Top CRT Hit reconstruction

Once CRT data fragments are generated and saved by the DAQ, they can be processed through the reconstruction chain. The first step of the chain is the selection and formatting of the raw data of each FEB to obtain a CRT Data product which can be used in the later stages of the reconstruction. The following step is the CRT Hit production, the hit reconstruction algorithm uses the CRT data as an input to reconstruct a CRT hit data product, reconstructing its global coordinates and providing higher level timing information. The CRT Hit data product can be used for higher level analysis as such as matching between a CRT Hit and an optical flash reconstructed by the PMTs, or matching of CRT hits with TPC reconstructed tracks.

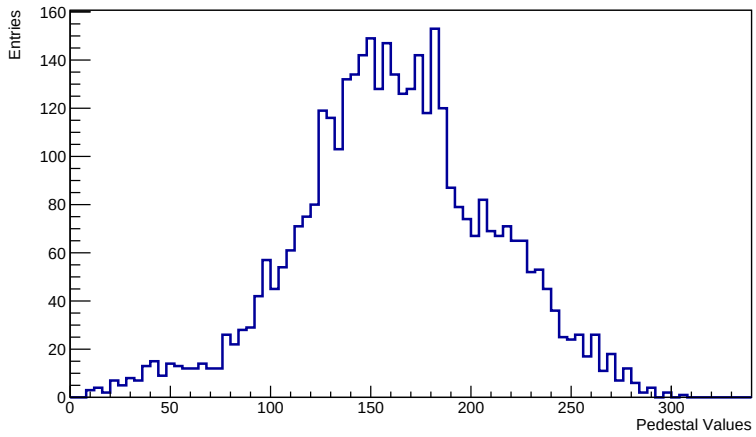

Figure 4.13: Distribution of the pedestal of all the channels of the Top CRT modules.

4.4.1 CRT data: decoding

At the decoding stage, the raw data from each FEB are selected and converted into a readable format (*decoding*). Some of the most relevant information of the CRT data product are:

- the FEB MAC5 address;
- the fragment ID, corresponding to the different CRT subdetector (Top, Side, Bottom);
- the poll start/stop timestamp provided by the CRT DAQ server;
- the *flags*, which represent the hit status (if it was an overflow of the TS0 or TS1 counters, or if it was a special reset hit of TS0 or TS1, or if it was a regular CRT Hit);
- *ts0* and *ts1*, respectively, values of the TS0 and TS1 counters;
- the ADC values of all 32 FEB channels.

Once a readable data format is obtained, a timestamp is assigned to each CRT Hit. The value of the ts0 counter is a number between 0 ns and 10^9 ns, for which the T0 counter is reset every second by an external PPS. Due to the propagation of the PPS signal along the T0 line, each counter is reset at a different absolute time with respect to another along the same timing line. To account for this difference, the counter value ts0 is corrected by adding the delay for that specific board:

$$ts0_d = ts0 + \Delta t_{T0i} \tag{4.3}$$

where the delay Δt_{T0i} is determined by equation 4.1. Following the addition of the specific board delays, only the absolute difference between the resulting value and the 10^9 ns is stored, to account, for example, for CRT hits which $ts0_d > 10^9$ ns:

$$ts0_{ns} = |10^9 - ts0_d| \tag{4.4}$$

The provide an absolute time to the CRT Hit, the full second in UNIX time stamp is obtained from the poll start and stop timestamps:

$$t0 = ts0_{ns} + FS_{polltime} * 10^9 \tag{4.5}$$

where *t0* is the absolute CRT Hit timestamp in ns and $FS_{polltime}$ is the full second of the poll time.

For what concerns the Top CRT data, each scintillator is read-out by 2 SiPMs on on the same end of the bar. For the Side CRT, at the decoder stage there is an additional step due to the its geometry, since the majority of the scintillator strips are readout on both ends by different FEBs, at the decoder stage, data fragments coming from adjacent layers are grouped together. The resulting CRT Data products can be used as is for calibration purposes or can be further processed to perform the CRT Hit reconstruction.

4.4.2 Photoelectron conversion

Following the calibration of pedestal and gains for all the Top CRT channels, the conversion of ADC counts to photo-electrons is obtained by:

$$n_{p.e.} = \frac{ADC_i - Ped_i}{G_i} \tag{4.6}$$

where $n_{p.e.}$ is the resulting number of photo-electrons, ADC_i is the ADC value of the i-th channel and Ped_i and G_i are, respectively, its pedestal and its gain as evaluated from the calibration.

The calibration was performed on both a sample of data processed from Run 0 (Commissioning data) and a sample of data from Run 1 (first physics run). It was estimated that for an effective calibration of the Top CRT, at least 50k events are needed, corresponding to ∼10 million CRT hits using the reduced 6 ms software window. In the future, we plan to introduce automatic calibration on a weekly basis.

4.4.3 CRT Hit: spatial reconstruction

The CRT Hit reconstruction is performed on the CRT Data product to reconstruct the global position in the detector coordinates and to perform additional corrections to the CRT Hit timestamp. Additional timing corrections are needed to account for the light propagation inside the scintillator from the CRT Hit position to the SiPM readout. An additional feature, which is

Type	Region	Region ID	Module (count)
Side CRT	west-south	40	0-17 (18)
	west-center	41	18-33 (16)
	west-north	42	34-51 (18)
	east-south	43	52-69 (18)
	east-center	44	70-85 (16)
	east-north	45	86-103 (18)
	south	46	104-142 (39)
	north	47	143-166 (24)
Bottom CRT	bottom	50	167-180 (14)
Top CRT	horizontal plane	30	181-264 (84)
	rim-west	31	265-278 (14)
	rim-east	32	279-292 (14)
	rim-south	33	293-298 (6)
	rim-north	34	299-304 (6)

Table 4.4: Total number of CRT modules ordered by the different CRT sub-detectors and the different detector regions.

exploited in this stage, is the processing of the global trigger timestamp to provide an additional time reference for each CRT Hit.

The first step of the CRT Hit reconstruction is the conversion from ADC to number of PE following equation 4.6, as described in the previous section. At this step, a preliminary selection of CRT data above a certain PE threshold can be performed, this is true for Side CRT hits for which a threshold of 7.5 PE was chosen. In the case of the Top CRT, the quadruple coincidence of the internal triggering logic is robust enough to select a very pure sample, therefore no cuts have been applied.

The second step of the CRT Hit reconstruction is the shifting of each module (associated with a specific FEB) into its coordinates in the detector volume. The module position is included in the geometry model of ICARUS and it has been thoroughly exploited for the detector simulation. Overall, the geometry of the CRT system is composed of 305 modules divided into the three different sub-detectors; in Table 4.4 a summary of the different modules and the corresponding regions are reported. An illustration of the mapping of the Top CRT module is presented in Figure 4.14. It is worth noting that despite the detector design (and subsequently the detector simulation) accounting for 6 modules along the Top CRT south rim, in reality only 5 were installed, to allow the access to ther detector roof.

The CRT hit is first reconstructed inside the single module and later translated into the global coordinate system. Hit reconstruction within each module is CRT subsystem specific.

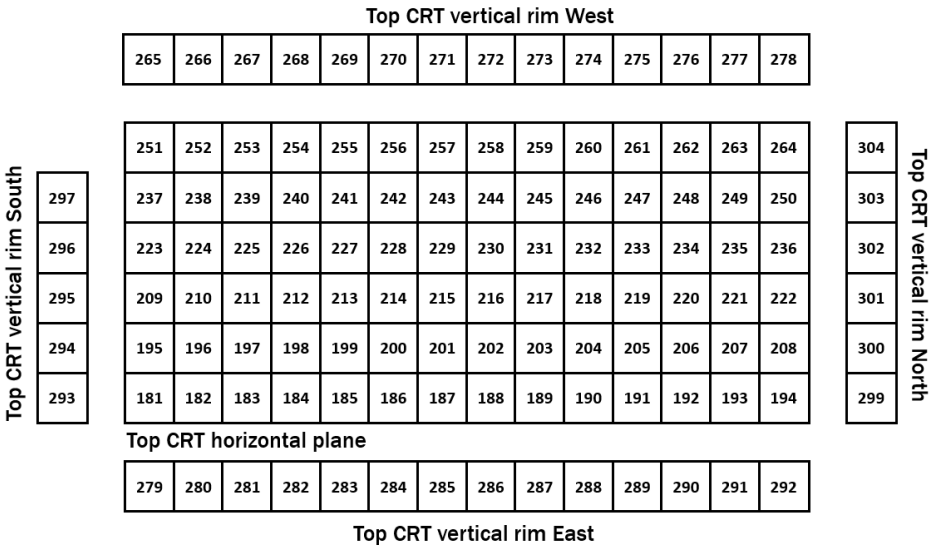

Figure 4.14: Mapping of the different software module IDs in the different regions of the Top CRT.

Top CRT: hit position

The Top CRT hit reconstruction is performed by selecting the two even-odd channels with higher PEs in the top layer (corresponding to a 10 mm scintillator strip) and those in the bottom layer (corresponding to a 15 mm scintillator strip). Due to the orthogonal orientation of the two layers, the position of a Top CRT hit is uniquely identified by the overlapping region (coincidence sector) of the two scintillator bars. The global coordinates of the CRT module are defined w.r.t. the center of the module, therefore the local coordinates of the CRT hit are reconstructed w.r.t. the middle position along each scintillator strip. During the commissioning and the analysis of the first data, a mismatch was observed between the real Top CRT module orientation and the one implemented in the simulation. Therefore, the simulation geometry was corrected and the Top CRT modules rotated by 180° around their perpendicular axis to reflect the real position of the SiPMs. The new geometry was tested and validated by comparing the channels above threshold and the reconstructed hit position for a specific subset of modules in each Top CRT wall.

The results of the Top CRT Hit reconstruction are reported in Figure 4.15. The plotted CRT Hit distribution correspond to a data sample of one run acquired during the commissioning of the Top CRT (April 2022, run 8148). Each point of the distribution correspond to a different coincidence sector of Top CRT and the Z axis, omitted to ease the visualization, reflects the number of hits in that specific location.

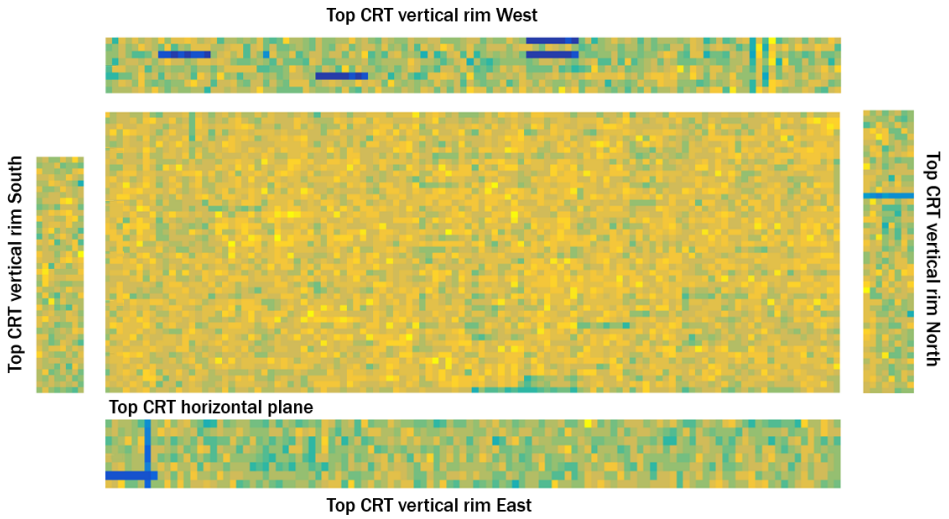

Figure 4.15: Distribution of the CRT Hits reconstructed in the different regions of the Top CRT. Blue regions correspond to malfunctioning channels.

Side CRT: hit position

The Side CRT hit reconstruction is different as the coincidence of adjacent layer has to be reconstructed at software level and bars and layers are readout by multiple FEBs. Hit scintillator strips are identified by selecting in each FEB the channel that generated the FEB trigger signal, using the highest charge amplitude as a discriminator. If the scintillator strip is readout on both ends by two different FEBs and both the corresponding channels are above threshold, the longitudinal position can be reconstructed by comparing the timestamps recorded by the FEBs:

$$T_A = T_0 + (L_0 - z) * V \tag{4.7}$$

$$T_B = T_0 + (L_0 + z) * V \tag{4.8}$$

$$T_A - T_B = 2z * V \tag{4.9}$$

$$z = (T_A - T_B)/2 * V \tag{4.10}$$

where, as illustrated in Figure 4.16, T_A and T_B are the timestamps recorded by FEB-A and FEB-B, z is the CRT hit position, L_0 is the position of the center of the scintillator strip, and V is the speed of light propagation within the scintillator / WLS fiber.

The reconstruction of the longitudinal position is performed on both the inner layer and the outer layer. The final CRT hit position is obtained as the average between the longitudinal position reconstructed in the two layers, averaging, also, the remaining transverse coordinates of each strip, as

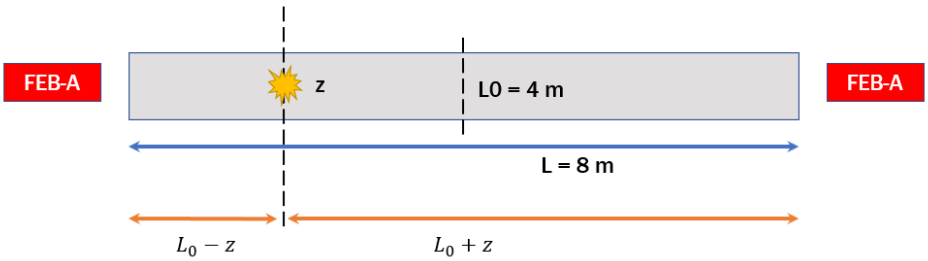

Figure 4.16: Illustration of the Side CRT hit position reconstruction along the 8 m long scintillator strips.

provided by the geometry. If the scintillator strip of only one of two layers is matched with two channels above the threshold, the CRT Hit position is defined only by the coordinates of that strip and by the reconstructed longitudinal position according to equation 4.10.

If no scintillator strip is associated with two channels above threshold in either of the two layers, scintillator strips matched with only one channel are considered. In this situation, the CRT hit position is assumed to be the middle position of the scintillator bar, averaged for the two layers if possible. In the case of the South wall (which exploits an X-Y configuration, where the outer layer is readout on one end only) the CRT hit position along the East-West direction is provided by the position of the vertical strip hit in the outer layer, while the top-bottom coordinate is given by the position of the strip hit in the inner layer. In the case of the downstream wall (which exploits parallel scintillator strips, cut and readout on one end only), the CRT Hit position is obtained as the average position of the strips hits in the two layers.

CRT hit: spatial resolution

Spatial resolutions of Top and Side CRTs are different and, also, region dependent. In the case of the Top CRT, the spatial resolution of the CRT hit, assuming a precision < 1 cm in the module coordinates provided by the detector geometry, is determined only by the width of the crossing scintillator strips. Since the crossing scintillators are 23 cm wide and the CRT hits are uniformly distributed along each strip, the spatial resolution σ along the transverse direction of the scintillator is estimated as follows:

$$\sigma = W/\sqrt{12} \tag{4.11}$$

where W is the width of the scintillator bar. In the local coordinates of the Top CRT modules, σ_x and σ_y are < 7 cm, while σ_z depends on the thickness of the scintillator and is estimated in the same way ($\sigma_z = \frac{2.5}{\sqrt{12}}$ cm).

Region	σ_x[cm]	σ_y[cm]
Side, lateral	16	229
Side, north	11	103
Side, south	17	14

Table 4.5: Spatial resolution of the Side CRT Hit reconstruction using local coordinates in the CRT region, with x as the lateral and y as the longitudinal coordinates. The resolution is quoted as one standard deviation of the full distribution for each coordinate.

The Side CRT timing resolution is currently under evaluation and, considering equation 4.10, it is the main contribution to the spatial resolution of the East and West walls. Generally, the error along the transverse direction of the scintillator strip is ~ 1 cm (σ_z in the local coordinates of the detector), while the resolution along the other two directions (quoting results reported from the simulation), is reported in Table 4.5.

Light propagation delay correction

Following the reconstruction of the CRT hit position, the timestamp of each CRT hit can be further improved by accounting for the light propagation inside the WLS fiber from the CRT position to the SiPM readout. The group velocity of light propagation inside the WLS fiber was estimated as 0.062 ns/cm, which refers to the same value used for equation 4.10 and in the detector simulation. The correction for the light propagation is obtained as follows:

$$\Delta t_\gamma = d * 0.062 \tag{4.12}$$

where d is the distance in cm between the CRT hit position and the SiPM readout. This correction model is used for the Side CRT reconstruction.

During the commissioning, this correction was also accepted for the Top CRT with some limitations. Unlike the side CRT, the Top CRT FEB firmware generates a timestamp of the triggered hit at the fulfillment of the triggering logic; therefore, as a preliminary step, the correction was applied considering the distance of the furthest SiPM w.r.t. to the hit position. Taking into account the Top CRT scintillator strips, this correction was < 1 ns for the sector closest to the SiPM readout, up to ~ 12 ns for the further regions. As it is presented in section 5.2, this correction was evaluated by fine-timing real data and exploiting the PMT-CRT matches.

An additional timing delay was included in the Top CRT hit reconstruction, to compensate for the micro-coaxial cable connecting the SiPMs and the FEB. The cable-induced delay was measured using an oscilloscope corresponding to a delay $\sim$ of 12 ns. A similar cable delay was also measured for the Side CRT and the appropriate correction was applied to the CRT Hit

reconstruction stage.
In the CRT hit reconstruction stage, each CRT hit timestamp is assigned an additional timing reference, provided by the Global Trigger logical signal reconstruction. The reconstruction of the trigger signal is described in section 4.5.

CRT hit data product

The result of the CRT hit reconstruction is a CRT Hit data product for which the following variables are stored:

- the FEB (or multiple FEBs for the Side CRTs) associated with the hit;
- the total number of photo-electrons in the CRT hit;
- the spatial coordinates and the respective errors;
- the CRT region of the hit;
- the absolute timestamp of the CRT hit (in ns UNIX standard time);
- the timestamp w.r.t. global trigger.

Following the CRT Hit reconstruction, the CRT Hit data products can be further used for higher-level analysis. In particular, Chapter 5 of this thesis will be dedicated to CRT-PMT matching and its exploitation for event selection purposes.

4.4.4 Top CRT channel testing

After the inclusion of the CRT modules in the DAQ and the subsequent data processing, it was possible to evaluate the status of the Top CRT and evaluate its functionalities and performance. The channel testing was a critical step for the Top CRT commissioning and a milestone to begin the overburden deployment activities. The Top CRT commissioning was completed by April 2022 and it enabled the start of the concrete blocks deployment. Once installed, the overburden prevented the extraction of the Top CRT modules, therefore it prevented any possible restoring and fixing operation of the SiPMs (FEBs are still reachable from the detector roof).

By analysing the output of the CRT Hit reconstruction, it was observed that 6 scintillators (all located along the Top CRT vertical rims), where not providing any trigger. This effect can be seen in Figure 4.15 as blue regions along the Top CRT vertical rims. The modules were successfully tested before the movement with the overhead crane for the installation. All these modules were stored in the same racks with faulty modules reported in 3.4.2. Possibly, the SiPMs corresponding to the dead channels were in a damaged but working state at the time of the electronic test, the crane movement or

the current in-rush (when turning on and off the SiPM bias with the DAQ) aggravated the damage. Unfortunately, these modules along the vertical rims can not be extracted, as, following their installation the supporting steel beams of the Top CRT horizontal plane were secured. Overall, the amount of dead channels is contained to 6 channels out of 4000 (0.15%), but, due to the internal triggering logic of the Top CRT FEB (requiring both the SiPMs of a same strip to be above 1.5 pe threshold), this reflects to 6 scintillators not providing any trigger. The total active surface of the Top CRT is reduced $\sim$ 2.5 m^2 and, luckily, it is all distributed along the vertical rims, which are exposed to a lower flux of cosmic particles w.r.t. to the horizontal plane. The active area is 99.7%, the value is in compliance with the experiment requirements. A possible improvement, to recover the scintillators, would be enabling for those specific modules the logic OR of all the channels, losing the effective Top CRT internal triggering logic and resulting in the need of a higher threshold to limit the electronic noise. This option is available, but not yet implemented.

In addition to the 6 channels with faulty SiPMs reported, an additional malfunctioning channel was observed in the Top CRT north rim. Differently from the others, this channel is responsive, but triggering at a significantly lower rate. The specific SiPM parameters were verified, to investigate for possible errors in the specific FEB parameters, but no anomalies were found. More tests are foreseen to investigate the issue.

4.5 Global Trigger

4.5.1 ICARUS trigger

The Global Trigger is a logical signal associated with the primary event trigger. The event trigger is generated when a predetermined number of PMT pairs (*PMT majority*) in the same TPC is above a certain threshold in coincidence with the expected beam gate. For ICARUS Run 1, the primary event trigger requirements were $\geq$ 5 PMT pairs with a 400 ADC threshold each (*on-beam majority trigger*). If the requirement is fulfilled, the trigger system send an enable signal to the PMT digitizers to save and sample the corresponding waveforms. PMT signals are recorded for $\pm$ 2 ms around the primary event trigger time, to recognize and tag cosmic rays crossing the detector during the 1 ms drift time of the TPC. Depending on the beam type, the beam gate width is significantly different (1.6 μs for BNB and 9.6μs for NuMI), therefore the on-beam majority trigger requirements are applied only to a small fraction of the 4 ms readout window of the PMT, the rest is called the *out-of-beam* time window. The requirements on the PMT triggering logic for the out-of-beam window are more stringent; for Run 1 the requirements were $\geq$ 10 PMT pairs with a 400 ADC threshold. Another difference between the on-beam and out-of-beam requirements is the sampling time of the PMT

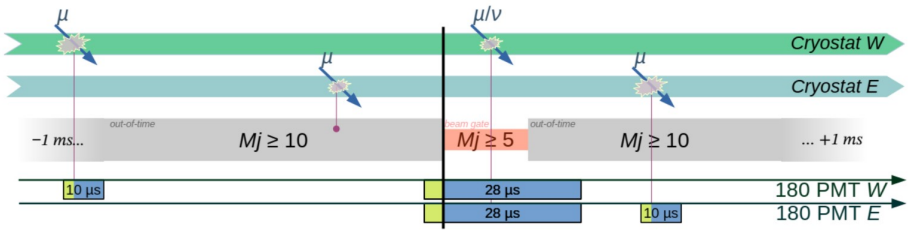

Figure 4.17: Schematic illustration of the different PMT trigger requirements for on-beam (orange) and out-of-beam (grey). The black line corresponds to the start of the neutrino beam spill.

waveforms, 28 μs for the on-beam and 10 μs for the out-of-beam. The different requirements were driven by the necessity to limit the data size and the waveform sampling in the time window where beam neutrinos are not expected. In Figure 4.17 a schematic illustration of the different PMT trigger requirements is presented for the on-beam and out-of-beam windows. Since the on-beam and out-of-beam windows have different threshold requirements, the latter cannot be directly used as the *background* of the neutrino-beam timing window. In order to have a comparable background sample, a fake beam gate window is opened between the different spills, and its requirements are the same as the normal on-beam trigger. This data stream is called *OffBeam* and the frequency of the fake signal depends on the beam type. Overall, in normal operations, ICARUS is running with 4 different data streams: BNB, OffBeam BNB, NuMI and OffBeam NuMI. The rate between the OffBeam and OnBeam triggers depends on the running configuration: during the Commissioning of the detector the rate between OffBeam and OnBeam data was 1/3 for BNB and 1/1 for NuMI; during Run 1 the ratio was 1/1 for both the beam streams. Another important data stream, used especially for calibration purposes, is the so called BNB and NuMI *minimum bias* trigger. The minimum bias generates triggers at the beam gate time regardless of light activity. During the ICARUS Run 1, 1/200 BNB triggers was acquired with the minimum bias requirements, for NuMI the ratio was 1/60 and for both OffBeam BNB and OffBeam NuMI it was 1/20.

4.5.2 CRT Global trigger acquisition

In order to effectively perform the cosmic background rejection, the CRT and PMT systems must be properly synchronized. Two different options can be exploited: using the absolute timestamp or using an additional timing reference, as such as the primary event trigger logical signal (or global trigger). If during the beam gate opening the majority 5 requirements of the PMTs is fulfilled, the digitization of the PMT waveforms is enabled and a logical signal is generated by an FPGA in the trigger rack. This logical signal is

referred to as global trigger signal, and it is distributed from a fan-out to the CRT and PMT subsystems. It is worth noting that a similar signal is generated from two different FPGAs and distributed to the different TPC board digitizers. Due to the different origin w.r.t. the global trigger signal sent to the PMT/CRT, additional delays should be accounted and measured for a synchronization with the TPC boards, but, due to their 400 ns sampling time, it is negligible.

The global trigger signal was also sent to a spare channel of one PMT digitizer to fine tune the timing propagation correction . The timestamp of the digitized global trigger signal, once properly corrected, can be used as a time reference for synchronizing the PMT signal (optical hits and optical flashes) with the CRT hits. As previously described in section 4.2, the global trigger logical signal is sent out to all the CRT FEBs along the T1 distribution line and all the relevant delays were measured with, conservatively, 1 ns resolution. The global trigger signal resets the ts1 counter and generates a special hit for which the values of the ts0 and ts1 counter are stored at the time of reset. This special reset event is referred to as *T1 reset hit*. If the FEB internal oscillator was an ideal device, no differences would be seen in the ts0 counter values of all the CRT FEBs at the time of the T1 reset hit.

In reality, the oscillation frequency is not nominal and small differences are expected (e.g. due to temperature). This variance is called the Allan variance[65]. The distribution of the CRT FEBs Allan variance can be obtained by comparing the ts0 counter values for the special T0 reset hits. The T0 counter is reset by a very precise PPS generated by a White Rabbit system[66]. The White-Rabbit regulated PPS is provided by a GPS timing signal. If the CRT FEB oscillator was an ideal device, all boards would show a ts0 value of 10^9 counts at the time of reset. The Allan variance can be obtained by plotting the difference between the internal clock counter values and 10^9 counts (corresponding to 1 s) at the time of the T0 reset hit. In Figure 4.18 the Allan deviation distribution for all the Top CRT FEBs is shown; data were obtained from commissioning runs. The variance can be up to 7 ns, which, if not properly accounted for, could significantly affect the CRT timing resolution. The CRT FEB should compensate for the internal deviations by means of a feedback voltage provided to the voltage controlled crystal oscillator. Nonetheless, the Allan variance could be compensated by using for each FEB its own ts0 of the T1 reset hit. Unfortunately, due to the bug reported in section 4.1.1, the special reset hits are not always correctly flagged and only $\sim$ 60% of them are identified. This percentage was estimated by plotting for each event the percentage of the FEB that correctly flags the T1 special reset signal; in Figure 4.19 the resulting distribution is shown, corresponding to a small sub-sample of the commissioning dataset.

The timestamp of the global trigger signal is reconstructed using the following equation:

$$TS(GT)_i = TS0_i + \Delta t_{T1i} \tag{4.13}$$

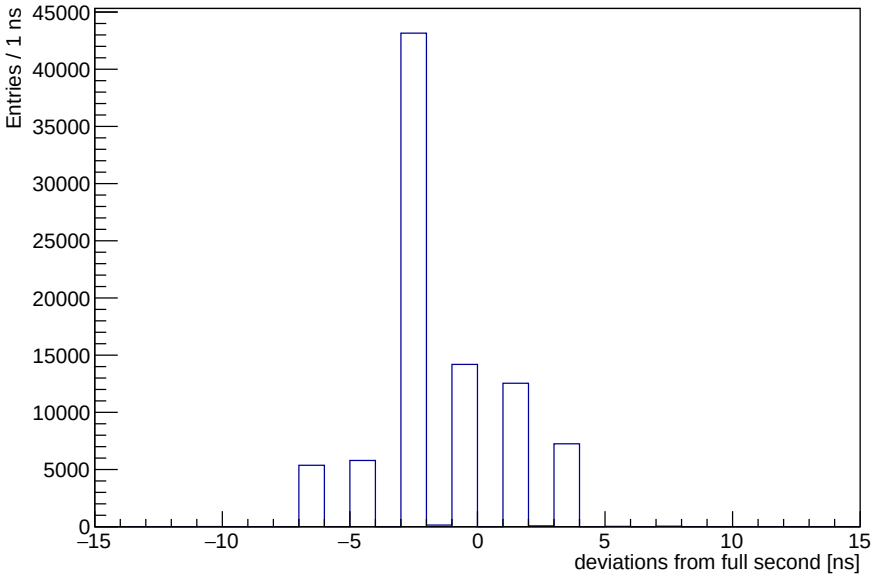

Figure 4.18: Distribution of the internal clock deviations from the reference full second for the Top CRT FEBs.

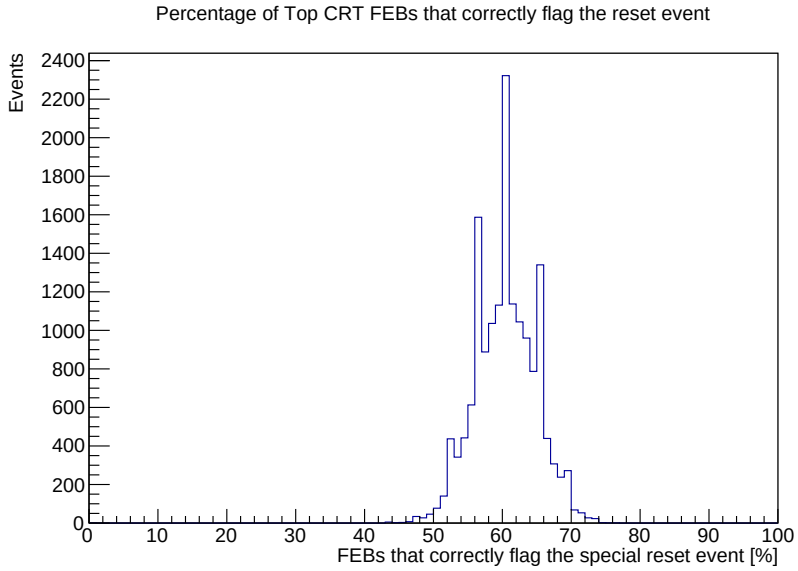

Figure 4.19: Distribution of the percentage of Top CRT FEBs that correctly flag the T1 reset event in each event.

where $TS(GT)_i$ is the timestamp associated with the global trigger signal reconstructed from the i-th Top CRT FEB, $TS0_i$ is the time at which the FEB digitizes the T1 reset signal (obtain from equation 4.5) and Δt_{T1i} is the delay along the T1 distribution of the i-th module. Considering the distribution reported in Figure 4.19, the Allan variance can be compensated using 4.13 only for a ∼60% of CRT hits, for those boards that do not flag the special reset event, the mode of the $TS(GT)_i$ was chosen as the best approximation.

The timestamp of the global trigger is reconstructed at the initial stage of the CRT Hit reconstruction algorithm by querying for the special reset hits for each FEB and assigning the the mode to those boards that miss it. Then after each CRT hit is reconstructed, an additional timestamp is assigned to it as its time difference w.r.t. to the global trigger. Since the majority of events in the ICARUS detector are triggered by cosmic particles, the same events will also be matched with a CRT hit at a certain time before the global trigger signal formation. In Figure 4.20 the distribution of the CRT Hits w.r.t. the global trigger signal is shown for a ± 1 ms around the trigger signal. The distribution shows a clear peak around 0 μs which is due to cosmic particles entering from the CRT and generating the trigger signal inside the TPC. By zooming in the timing window 1 μs before the trigger signal formation and considering only the Top CRT hits, the peak distribution is more visible and important features can be extrapolated, in particular, its mean position at ∼ 630 ns before the trigger signal and a characteristic tail between -600 and -800 ns. The zoomed in distribution is presented in Figure 4.21 and can be compared with the analogous distribution obtained for PMT optical flashes timestamps w.r.t. the trigger signal reconstructed by the PMT digitizers, in Figure 4.22 the distribution of the PMT optical flashes is shown. The ∼ 600 ns peak distance observed in both the CRT and PMT distribution is due to the delay between the PMT waveform digitization and the signal formation. The tail structure is observed in both the PMT and CRT distribution and it is due to a ∼ 160 ns buffer in the PMT digitizers: cosmic activity before the beam gate opening generates LVDS signals (sent out to the trigger FPGA) that stay in a high state for 160 ns. If the gate opens during the LVDS buffer time it generates a trigger, with an effective additional delay up to 160 ns w.r.t. the real flash time.

In Figure 4.23 a detailed schematic shows how a cosmic track hitting the CRT (green) and triggering the PMTs (red) is timestamped. This illustration shows the increasing of time along the horizontal axis and is limited only to the most relevant elements of the detector timing scheme.

It should be noted that the DAQ provides a timestamp for the global trigger and refers to the same logical signal sent to the CRT and PMT systems. The trigger timestamp provided by the DAQ is generated after digitization of the global trigger signal by the SPEXI board, this induces significant resolution effects due to the board clock (125 MHz) and the resulting 8 ns

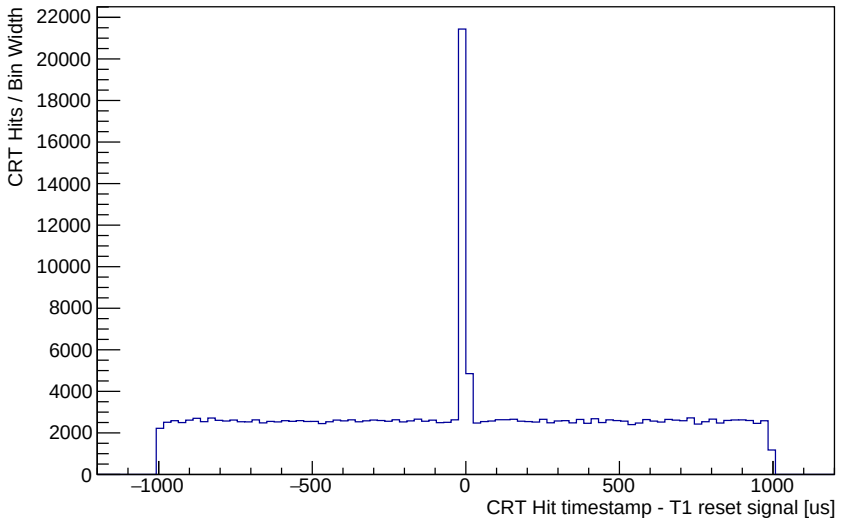

Figure 4.20: Distribution of the CRT Hits timestamps in a ± 1 ms window around the trigger signal.

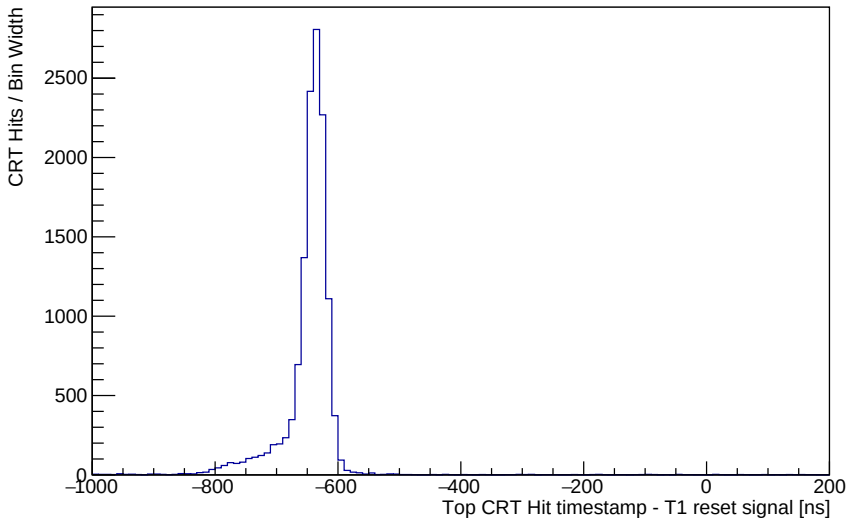

Figure 4.21: Distribution of the Top CRT hits timestamps w.r.t. the trigger signal in the zoomed in region 1 μs prior to the trigger formation.

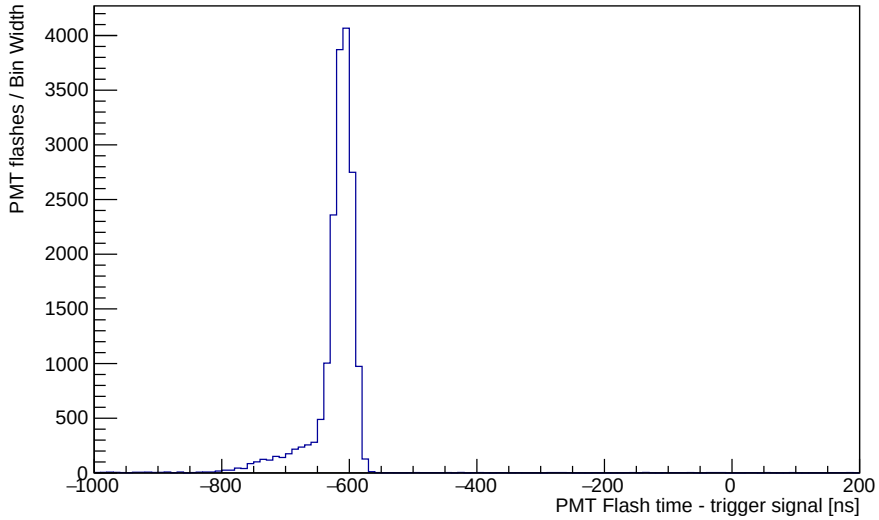

Figure 4.22: Distribution of the PMT optical flashes timestamps w.r.t. the digitized trigger signal zoomed in the zoomed region 1 μs prior to the trigger formation.

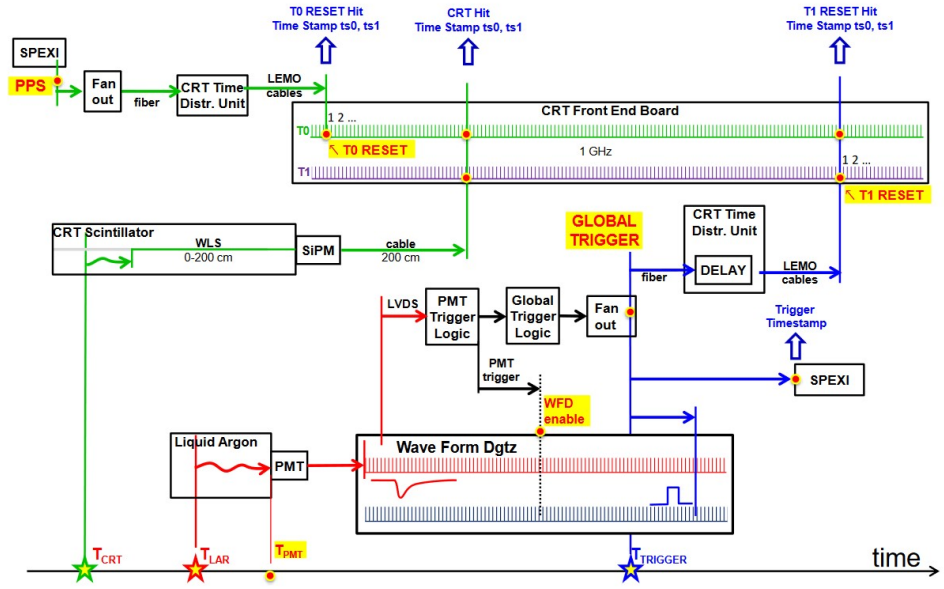

Figure 4.23: Detailed schematic of how a cosmic particle hitting the CRT (green) and triggering the PMTs (red) is time stamped. Time increases along the horizontal axis only.

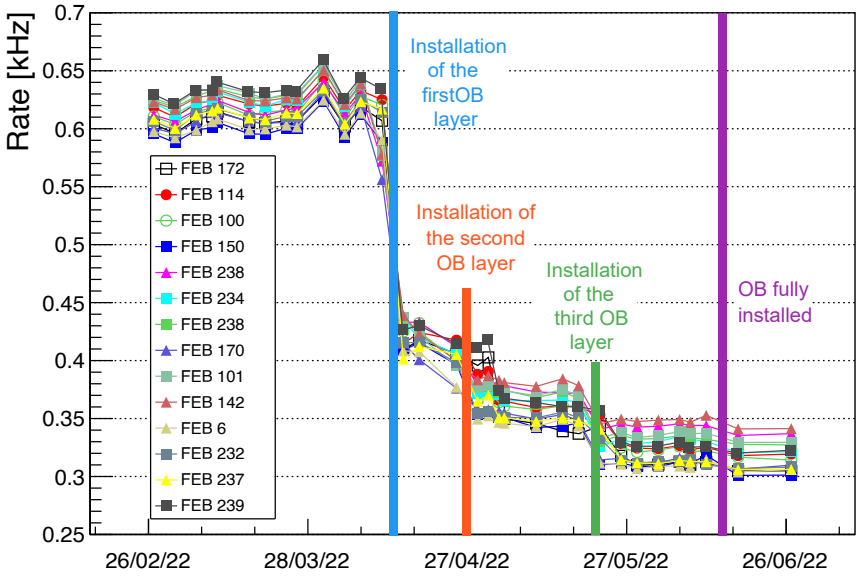

Figure 4.24: Average trigger rate as a function of time for a sample of Top CRT horizontal modules; the rate decrease follows the progress of the overburden installation.

discretization effect (the trigger timestamp is always a multiple of 8). Due to this reason, the trigger timestamp provided by the DAQ is affected by intrinsic systematics at the order of tens of ns and cannot be exploited for CRT-PMT matching.

4.6 Overburden and cosmic rate

The Top CRT commissioning was concluded at the beginning of April and it set the start of the installation of the 3m concrete overburden, described in section 2.6.4. The nominal mean rate of each horizontal Top CRT module before the installation of the overburden was $\sim$ 620 Hz, while the rate for vertically installed modules was $\sim$ 250 Hz, this result is in agreement with what was measured at the Frascati test stand. The cosmic ray spectrum at sea level is made of two components: the soft component ($\sim$ 30%) and the hard component ($\sim$ 70%). The hard component is composed of muons with a mean energy of 4 GeV and their average rate is $\sim$ 100 Hz/m^2 ($\sim$ 70 Hz/^{2} considering only straight going muons)[67]. Considering the Top CRT modules surface of $\sim$ 3.4 m^2, the expected cosmic muon rate is $\sim$ 340 Hz. The difference with the measured value is due to the soft component of the cosmic spectrum, made of electrons, positrons, and gammas, which, if

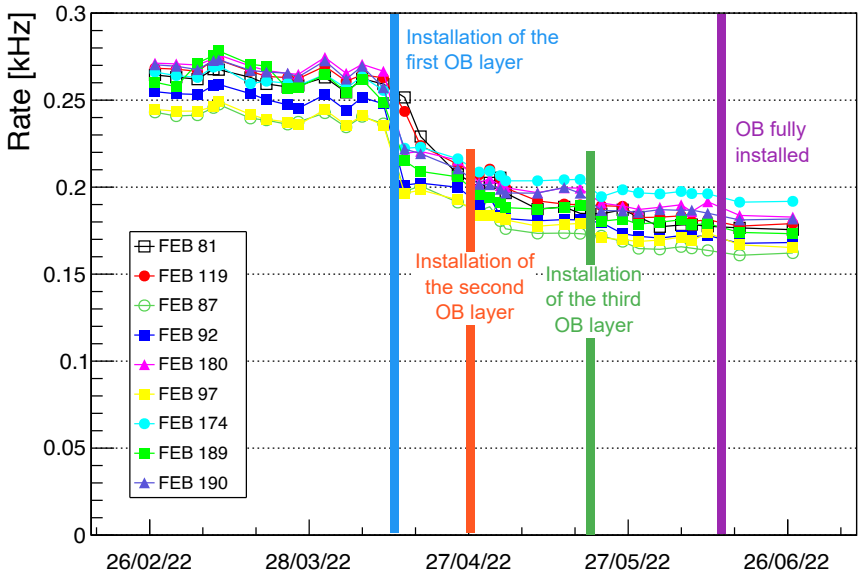

Figure 4.25: Average trigger rate as a function of time for a sample of Top CRT vertical modules.

energetic enough, can generate a trigger in the CRT modules. Considering the whole Top CRT horizontal surface, before the overburden installation the detector was exposed to a $\sim$ rate of 52 kHz cosmic particles.

During the installation of the overburden, it was possible to monitor day by day the average rate of each CRT module; therefore, it was possible to verify the effective reduction in the cosmic particle ray induced by the concrete layers. In Figure 4.24 and 4.25 the plot of the average cosmic particles rate as a function of the acquisition date is shown for a sub-sample of horizontal and vertical modules. After the full installation the Top CRT cosmic rate per module decreased from $\sim$ 620 Hz to $\sim$ 330 for the horizontal plane and from $\sim$ 250 to $\sim$ 180 for the vertical rims, in agreement with the soft electromagnetic component removal mediated by the concrete (see section 2.6.4. The new average rate per module is in agreement with the expected muon-only component of the cosmic spectrum[67]. The overall cosmic rate on the whole Top CRT surface after the full overburden installation is 35 kHz (28 kHz if considering only the horizontal plane).

The overburden was completed in mid-June 2022 and it set the final milestone for the beginning of the ICARUS Run-1, which lasted about 1 month, taking data both on the BNB and NuMI beamlines.

Chapter 5

Analysis of the combined Cosmic Ray Tagger and LAr scintillation light

The synchronization between the cosmic tagger hits and scintillations in LAr offer a unique opportunity to exploit one of the key aspects of the ICARUS experiment: the event timing. Throughout the previous chapters of this thesis, a lot of emphasis was put on the timing of all the different experiment components, namely the CRT and PMT timing, the trigger formation and the beam time structure. Effective background rejection and event selection tools can be obtained by comparing the CRT and PMT timing, determining the direction of a cosmic particle and, possibly, the origin of the primary event trigger whether or not it was matched with a CRT Hit.

In this chapter, I am presenting the first results of the CRT-PMT combined analysis and how the relative timing can be used for calibration, background rejection and event selection.

5.1 CRT-PMT matching

The CRT hits to PMT optical flashes match can be performed using only the synchronized timing between the two sub-detectors. Figure 5.1 shows the distribution of all the CRT hits (red) and optical flashes (blue) timestamps w.r.t. the digitized global trigger signal in the timing region associated with the primary event trigger. The dataset used to reproduce this plot was the the offbeam-BNB data-stream for one run of the ICARUS Run 1; overall, in this dataset 17k offbeam events were collected. The CRT Hit sample includes both Top and Side CRT hits. The evaluation of Side CRT time relative to the global trigger is performed by exploiting the mode of Top CRT T1 reset data, as the Side CRT reset event reconstruction was not in production at the time of this work (see 4.5). Figure 5.2 shows the CRT

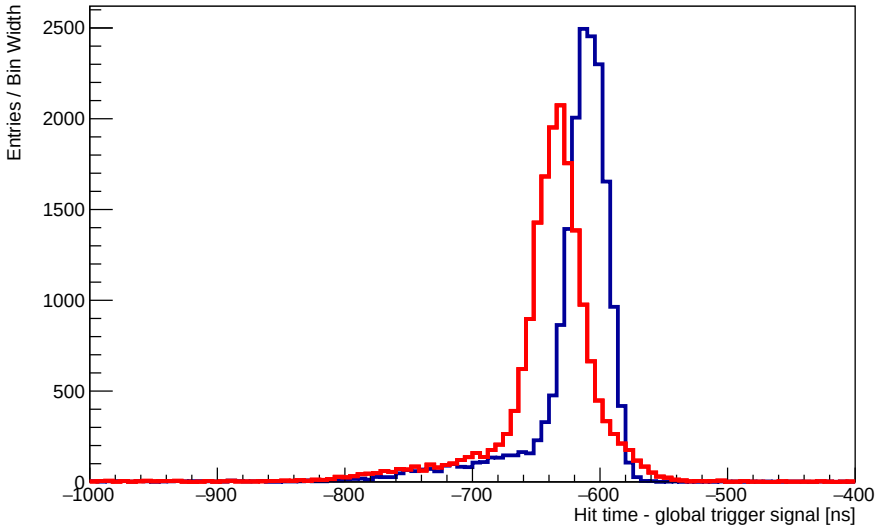

Figure 5.1: Time distribution of the CRT hits (red) and PMT optical flashes (blue) close to the primary event trigger w.r.t. the digitized global trigger signal.

hit time distribution distinguishing for the Top (green) and Side (red) sub-detectors, using the trigger signal as the time reference; the sum of the two distributions is also shown as a blue dashed line. The shift between the CRT hits and the optical flashes distribution is expected by assuming a time of flight of several ns between the cosmic hit in the CRT plane and the flash reconstruction in the active liquid argon volume.

An optical flash is a PMT related data product that groups together all the optical hits associated with one trigger. Each optical hit corresponds to a digitized and sampled PMT waveform and it carries over timing (absolute timestamps and w.r.t. the digitized global trigger signal), amplitude (pulse height and its photoelectron conversion) and spatial (PMT position) information. The PMT waveforms are sampled for 28 μs and 10 μs in the on-beam and out-of-beam windows respectively, although, for this analysis, only the first 1 μs is kept. Each optical flash is assigned the timestamp of the optical hit with the highest pulse height.

The CRT-PMT matching is performed by coupling one or more CRT hits with one optical flash; the association is performed only by means of time information by selecting CRT hits and optical flashes which are up to 100 ns apart, in the global trigger time reference system. Depending on the cosmic track topology, more than one CRT hits could be matched with an optical flash, this is true, for example, for particles with a wide angle w.r.t. the detector roof, generating two CRT hits, one entering through the Top CRT

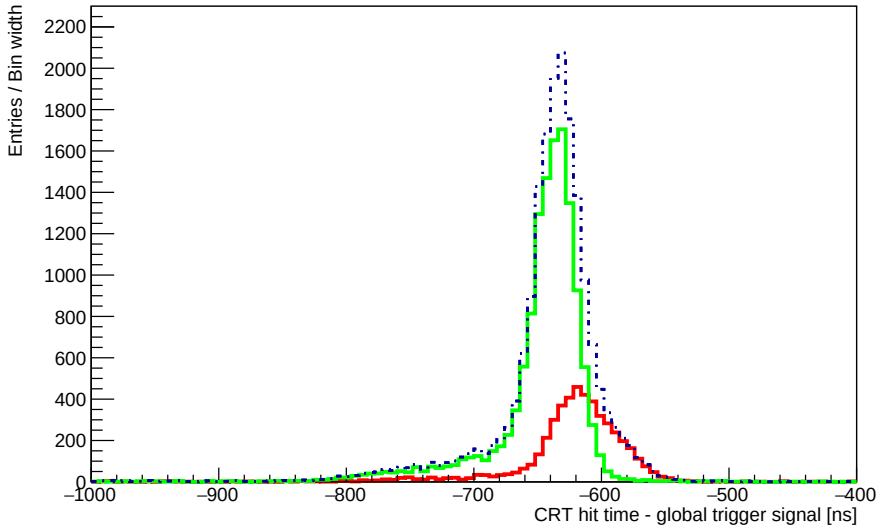

Figure 5.2: Time distribution of CRT hits (dashed blue) close to the primary event trigger w.r.t. the global trigger signal. The distribution is also plotted for the Top (green) and Side (red) CRT components.

and one exiting through the Side CRT. Another situation for which multiple CRT hits are expected is, for example, a shower like event, where, due to the 1 μs sampling of the optical hits, the light generated by two or more particles could not be disentangled within one optical flash and it would be matched with one CRT hit for every tagged component of the shower. Finally, random coincidences and electronic noise within 100 ns of a matched optical flash are a potential source of background. Each optical flash is assigned a position evaluated as the light barycenter weighted by the amplitude of each optical hit. The light barycenter is a viable approximation for the flash position, but, as it will be described in the next sections of this chapter, it needs to be refined to precisely evaluate the flight length and the time of flight of the cosmic track.

Depending on the time difference between the optical flash and the CRT hit, it is possible to estimate a direction of the cosmic particle:

$$\Delta t_{CRT-Flash} = t_{CRT} - t_{Flash} \tag{5.1}$$

the cosmic direction is defined *entering* for $\Delta t_{CRT-Flash} < 0$ ns and *exiting* for $\Delta t_{CRT-Flash} > 0$ ns.

$\Delta t_{CRT-Flash}$ depends on the flight length of the cosmic particle, but it is not a direct measure of the time of flight, as it also includes the scintillation light propagation time from the track to the PMTs. Figure 5.3 shows the distribution of the $\Delta t_{CRT-Flash}$ for a large sample of Top CRT hits matched

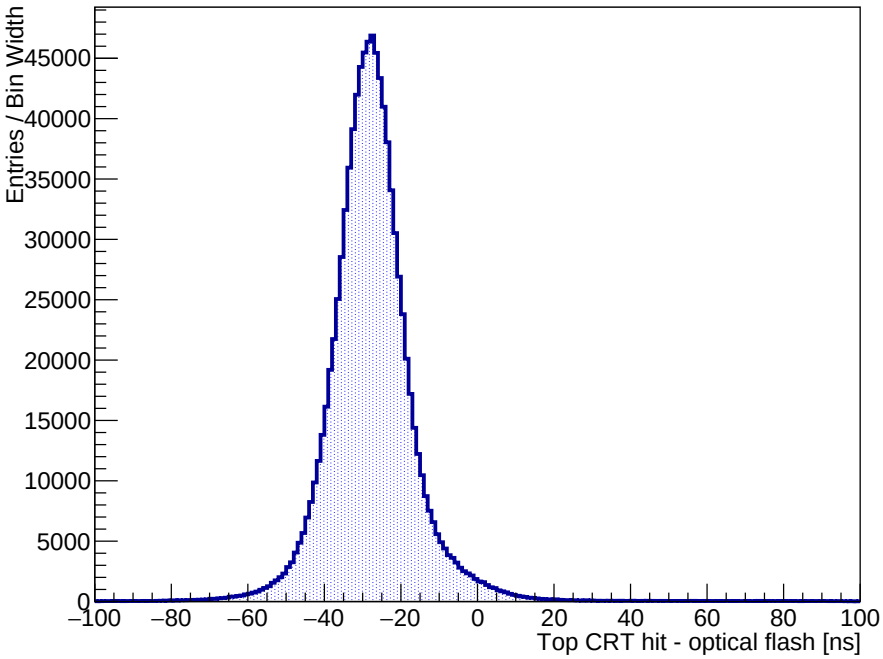

Figure 5.3: Distribution of the $\Delta t_{CRT-Flash}$ for all the Top CRT in the $\pm$ 100 ns matching window.

with an optical flash within the whole acquisition window. The distribution of the CRT hits populates the region < 0 ns, with a signature peak at -27 ns and a Gaussian-like shape. The negative values of the Top CRT distribution are expected, as the Top CRT is supposed to intercept alone 80% of the entering cosmics. Figure 5.4 shows the distribution of $\Delta t_{CRT-Flash}$ for the Side CRT hits matched with an optical flash. The resulting distribution is significantly different from the Top CRT one, as it shows two different peaks, one in the negative region and one in the positive. Similarly to the Top CRT hits, the negative region is due to cosmic particles entering from the Side CRT modules and generating a flash in the liquid argon active region. The negative peak is closer to 0 ns w.r.t. Figure 5.3 since the Side CRT panels are closer to the LAr vessel walls. The second peak, visible in the positive region of the distribution, is generated by cosmic particles exiting from the detector.

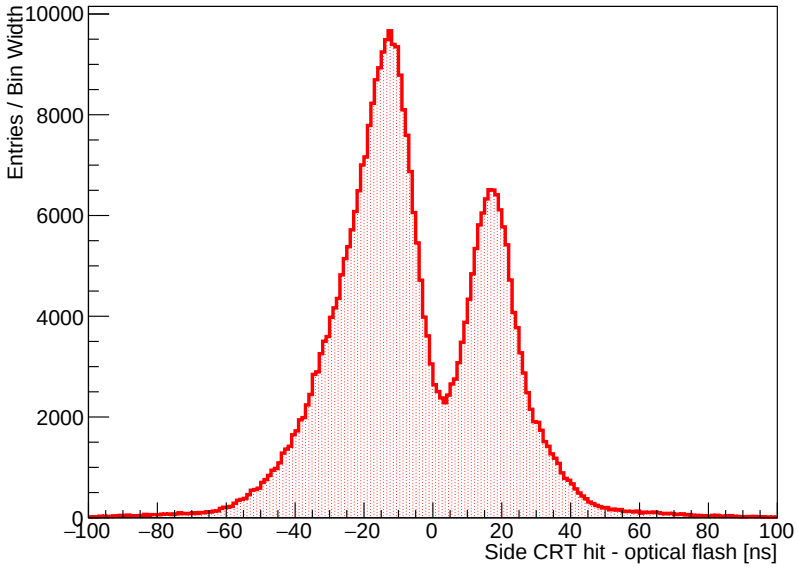

Figure 5.4: Distribution of the $\Delta t_{CRT-Flash}$ for all the Side CRT in the $\pm$ 100 ns matching window.

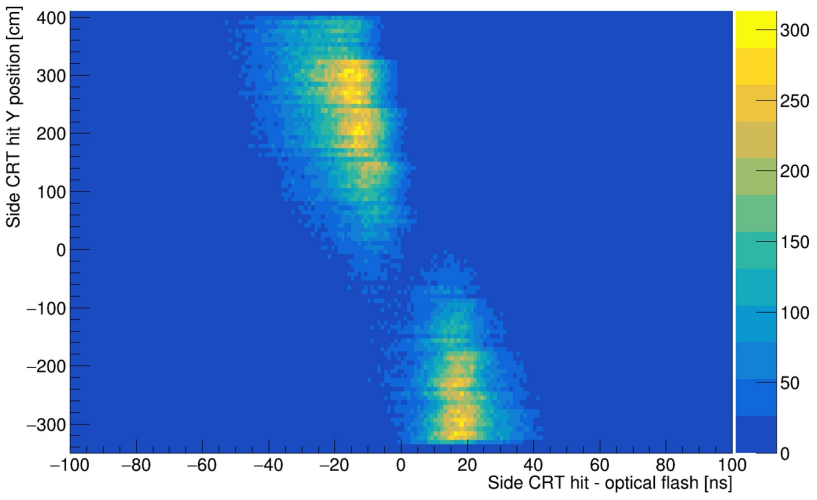

Figure 5.5: Distribution of the Side CRT hit position along the vertical direction vs the time difference with the matched optical flash.

The distinction between the two peaks can be better understood by plotting the relative Side CRT hit position along the vertical direction of the detector, this distribution is presented in Figure 5.5. The negative peak favours regions in the upper half of the detector volume. For geometrical effects, entering cosmics from the lower region are disfavoured by the zenith angle dependence. The positive peak, differently, favours the lower region of the Side CRT, as cosmics entering from the Top CRT and exiting from the upper region of the Side CRT would not cross the active liquid argon volume, therefore they would not be matched with an optical flash.

Figure 5.6 shows the overlay, in logarithmic scale, of the $\Delta t_{CRT-Flash}$ for Top (blue) and Side (red) CRTs. The relative population of the entering peaks for Top and Side CRT, is in agreement with the design expected cosmic muons geometrical acceptance of the two detectors (Top CRT $\sim$ 80% and Side CRT $\sim$ 20%).

Depending on the amount and the relative timing of the CRT hits matched with an optical flash, a preliminary classification can be achieved:

- optical flashes with no CRT hits matched;
- optical flashes preceded by a Top CRT hit;
- optical flashes preceded by a Side CRT hit;
- optical flashes preceded by a Top CRT hit and followed by a Side CRT hit;
- optical flashes followed by a Top CRT hit;
- optical flashes followed by a Side CRT hit;
- all the other situations.

These categories are exclusive. In order to study the effectiveness of the CRT-PMT matching, a big sample of more than 1 million optical flashes was analyzed using $\sim$ half of the Offbeam-BNB data sample collected during the Run 1 of ICARUS. The decision to use the Offbeam-BNB data sample was driven by the necessity of a pure sample of cosmic particles, without any effect that could have been induced by beam-related activity. The results of the analysis are reported in Figure 5.7 and Figure 5.8 where all the optical flashes have been categorized in different classes depending on the number of matched CRT hits and their relative timing. Table 5.1 reports a summary of the population of the different classes and the corresponding percentage.

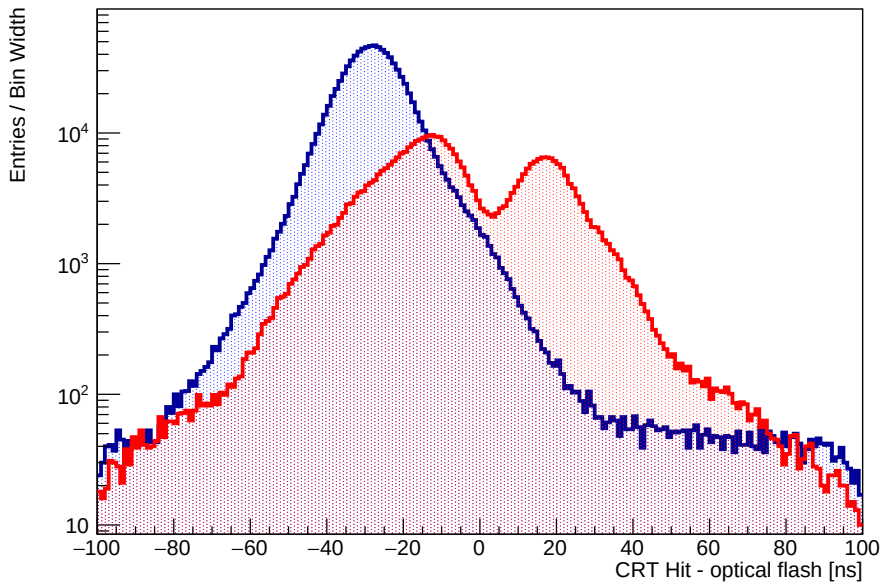

Figure 5.6: Overlap of Figure 5.3 (blue) and Figure 5.4 (red) in logarithmic scale.

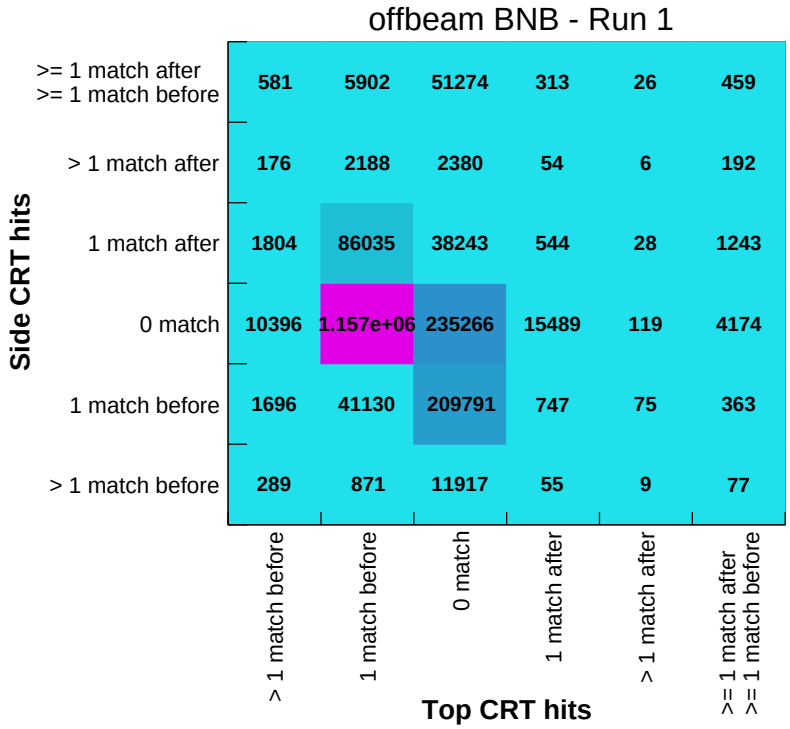

Figure 5.7: Categorization of the optical flashes depending on the results of the CRT-PMT matching. The data sample corresponds to $\sim$ 1.9 million optical flashes collected during the Run 1 of the ICARUS experiment. A match before (after) means that the CRT hit is collected before (after) the optical flash in LAr.

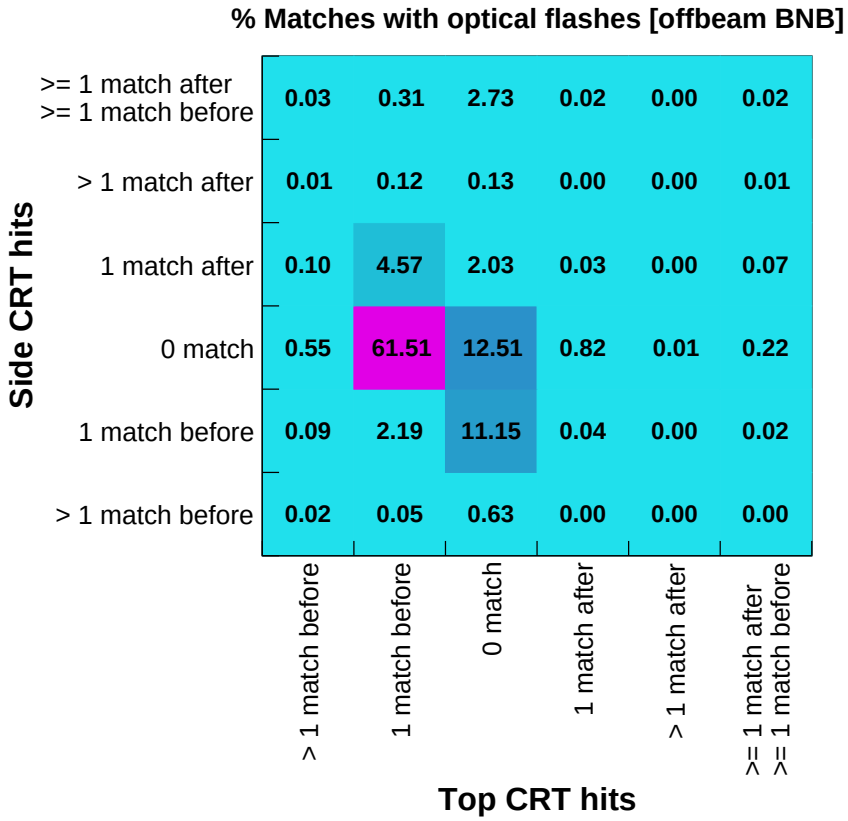

Figure 5.8: Relative percentage of optical flashes matching with Top and Side CRT hits for the $\sim$ 1.9 million optical flashes offbeam BNB data sample.

As expected from a cosmics-only data sample, the vast majority of optical flashes are preceded by a Top CRT hit (61.5%), and only 11.2% of them are preceded Side CRT hit. Concerning the class of optical flashes not matched with any CRT, several effects should be considered, namely: efficiency, geometrical acceptance, threshold effects, dead-time of the CRT boards and, eventually, neutral particles. In addition to these effects, optical flashes originated from late scintillation light of the liquid argon or wrongly reconstructed optical flashes can't be matched with CRT activity. Following the preliminary functionality tests, the average measured Top CRT efficiency was ∼96%, which could, considering also the dead channels, account for part of the not-tagged cosmic particles, nonetheless others effects should be considered. Another important contribution is determined by the dead-volume between adjacent Top CRT modules, corresponding to ∼2 cm, which adds up to ∼5.5 m^2 (1.9 % of the top surface), integrating over the whole horizontal plane. On top of this, the north wall of the Side CRT is not entirely covered, creating several square meters of dead-space. Additionally, threshold effects should be considered, in particular for the Side CRT, since the Top CRT internal triggering logic grants the possibility to operate with a very loose 1.5 p.e. threshold: due to high electronic noise, induced by the proximity with the liquid argon purification system, the Side CRT requires an high 7 p.e. threshold in each channel to trigger and generate an hit. Another rare, but possible effect is due to a crossing cosmic within the 22 μs board dead-time following the digitization of another CRT hit or a special reset event. Lastly, a contribution from non-tagged neutral particle interacting in the LAr volume is expected. In the close future, once the TPC tracks and CRT hit matching tool will be available, a numerical evaluation of the overall CRT efficiency can be estimated by back-projecting the TPC tracks to the CRT plane, determining the crossing point and verifying the presence of the CRT hit.

Table 5.1 reports also the the population of the classes with flashes followed by an hit on the CRT planes. The determination of *entering/exiting* relies on the timing resolution of the $\Delta t_{CRT-Flash}$ measurement. In the case of the Top CRT ∼3-4 ns timing resolution is not worrying, since, considering a minimum ionizing particle like a cosmic muon, it would correspond to uncertainty less then 1.5 m, well within the 4 m distance between the modules and the liquid argon active volume. In the case of the Side CRT, the scintillator panels are few cm from the cryostat walls, therefore, depending on the optical flash position they could not be able to resolve the direction of a track. In addition, the CRT tagging inefficiency could miss the entering cosmic track, resulting in a flash only followed by a Side CRT hit.

As a premise of this section it was stated that $\Delta t_{CRT-Flash}$ refers to the difference between the CRT hit time and the collection time of the scintillation light by the PMT. At this stage, a light propagation model in the liquid argon is not considered, but it is clear that in order to perform a pre-

	offbeam BNB Run 1	
Classification	**Entries**	**%**
No CRT match	235266	12.51
1 Entering from Top	1157004	61.51
1 Entering from Side	209791	11.15
1 Entering from Top 1 Exiting from Side	86035	4.57
1 Exiting from Top	15489	0.82
1 Exiting from Side	38243	2.03
Others	139088	7.39

Table 5.1: Summary of event classification depending on the number of matched CRT hits and their relative time with respect to the PMT optical flash. The data sample corresponds to $\sim$ 1.9 million optical flashes collected during the Run 1 of the ICARUS experiment.

cise classification just using timing information, the timing resolution of the $\Delta t_{CRT-Flash}$ has to be evaluated and the light propagation inside the liquid argon has to be included in this time-of-flight model.

5.2 Light propagation in Top CRT modules

The analysis of the CRT hits and the optical flashes offers the opportunity to fine tune the light propagation model, in order to estimate the corresponding propagation delay in each of the 64 coincidence sectors of the Top CRT modules. Conceptually, the distribution of $\Delta t_{CRT-Flash}$ presented in Figure 5.3 corresponds to the superimposition of all the 64 coincidence sectors of all the 123 Top CRT modules. By reprocessing the hit reconstruction stage of the collected data without the application of the light propagation model and summing the data of all Top CRT modules, the distribution of the $\Delta t_{CRT-Flash}$ can be obtained for each of the 64 sectors. Figure 5.9 shows the mean value of the $\Delta t_{CRT-Flash}$ distribution in each of the Top CRT 64 sectors, obtained by fitting the corresponding distribution with a Gaussian. As expected, the sectors further away from the SiPM readout present a smaller $\Delta t_{CRT-Flash}$ since:

$$\Delta t_{CRT-Flash} = t_{CRT-Hit} - t_{PMT} \tag{5.2}$$

and

$$t_{CRT-Hit} = t_{FEB} - t_{LP} \tag{5.3}$$

where t_{LP} is the light propagation time within the WLS fibre. Without a light propagation correction, the relative error $t_{LP}/t_{CRT-Hit}$ increases along

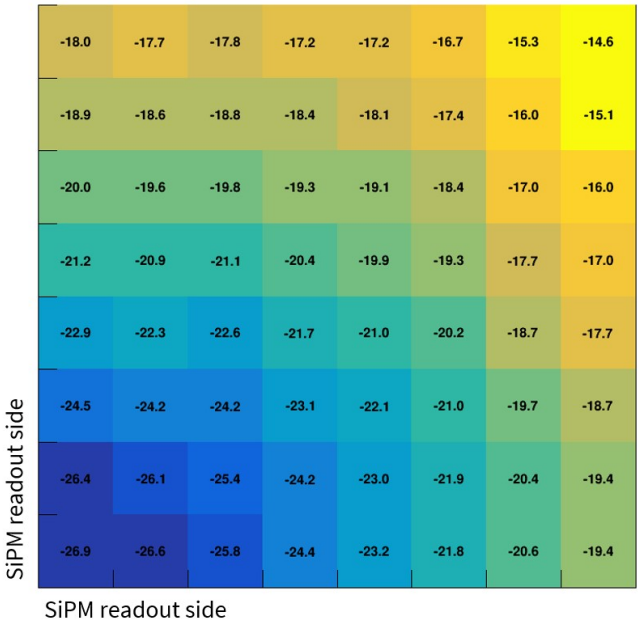

Figure 5.9: Mean $\Delta t_{CRT-Flash}$ in ns for each sector of the superimposed Top CRT modules without the light propagation model. The mean value was evaluated by fitting the distribution of each $\Delta t_{CRT-Flash}$ with a Gaussian function.

with the distance of the readout, resulting in $\Delta t_{CRT-Flash}$ smaller for further sectors.

Starting from Figure 5.9, a light delay calibration can be obtained by first equalizing the mean value of all the sectors to the one closer to the SiPM readout. The result is the correction mask presented in Figure 5.10. The correction, still, is not complete, since it should also account for the light propagation from the central point of the sector to the SiPM readout. On such a short distance (∼12 cm), the light propagation correction reported in equation 4.12 introduces relatively small errors, therefore it is considered acceptable. The delay of the closest sector (∼0.7 ns) is added as an offset to all sectors. The newly obtained correction mask can be applied at the hit reconstruction stage, with an improved correction of up to 1.5 ns, for the furthest sectors.

Following the improvements to the Top CRT light propagation model, the mean $\Delta t_{CRT-Flash}$ was obtained for each module by fitting the resulting distribution with a Gaussian fit, Figure 5.11 shows a fit for one module of the horizontal plane (module 188 in the Figure 4.14 notation). Figure 5.12 shows the distribution of the mean $\Delta t_{CRT-Flash}$ per each module, overlayed on its relative position in the Top CRT mapping. An interesting feature that can be inferred by this distribution is the visible "shadow" of the detector active

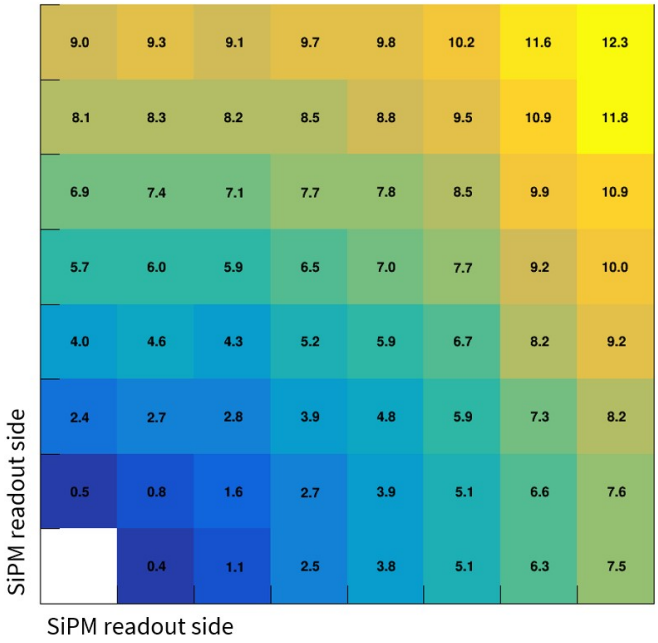

Figure 5.10: Correction mask obtained by equalizing all the Top CRT sectors mean $\Delta t_{CRT-Flash}$ in ns to the sector closer to SiPM readout.

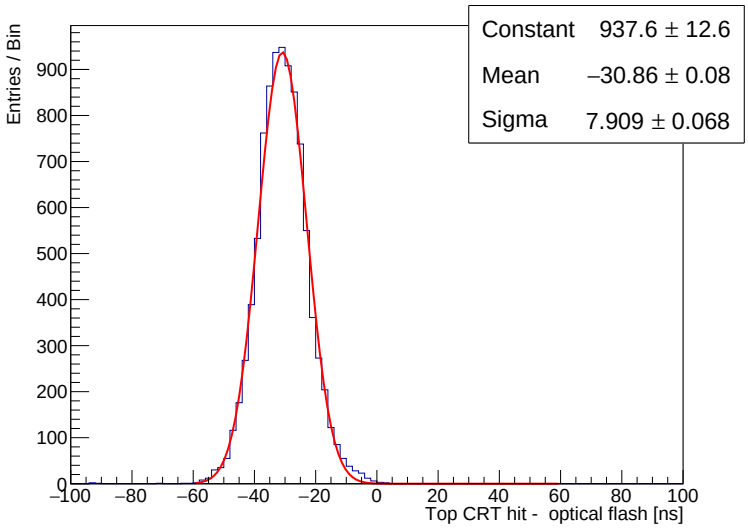

Figure 5.11: Distribution of the time difference in ns for all the flashes matched with one specific Top CRT module in the horizontal plane.

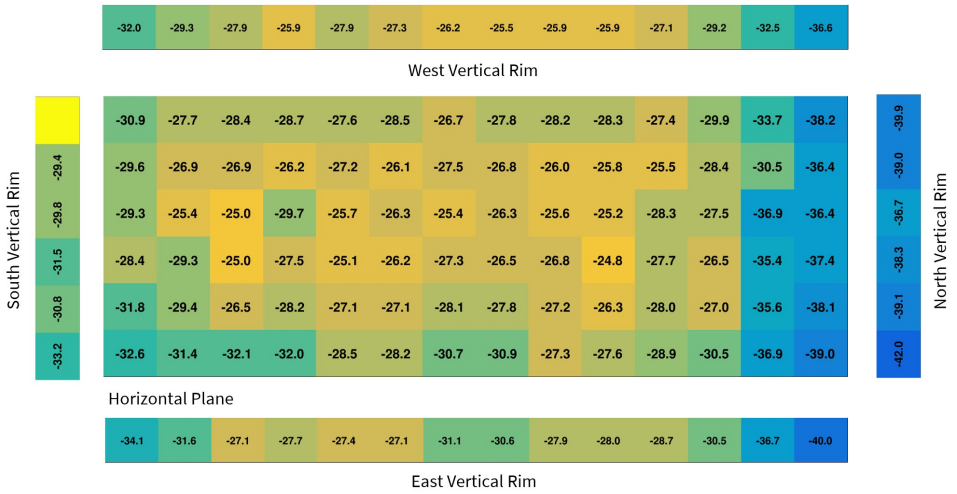

Figure 5.12: Distribution of the mean $\Delta t_{CRT-Flash}$ in ns per each module, overlayed on its relative position in the Top CRT mapping.

volume below the Top CRT modules. The last two rows of Top CRT modules on the north end of the detector are not directly installed on top the TPC volume, therefore, cosmic tracks crossing these modules and generating an optical flash in the liquid argon travel a longer flight length, corresponding to a bigger $|\Delta t_{CRT-Flash}|$. In the future, by enhancing the statistic, the shadow of the active liquid argon volume will be perceptible with a better resolution by plotting the mean $\Delta t_{CRT-Flash}$ for each sector. Figure 5.13 shows the distribution of the standard deviation of the Gaussian fit per each module overlayed on its relative position. The average σ is $\sim$ 8 ns and this spread includes several effects like the topology of the cosmic track, the propagation time of the scintillation light and, of course, the flight length which was not considered.

5.3 CRT-PMT time resolution: improved analysis

The average spread of $\sim$ 8 ns is affected by the missing corrections of the different flight length and the scintillation light propagation. A new analysis has been performed by considering these unaccounted effects of the cosmic track propagation. Differently from a neutrino interaction, in which a clear vertex can be associated with an optical flash, a cosmic muon does not allow to unambiguously determine a flash point from which reconstructing the flight length. The scintillation light is emitted throughout the whole liquid argon volume and, geometrically, it is possible to associate with each optical hit (corresponding to one PMT) a point along the cosmic track which is more

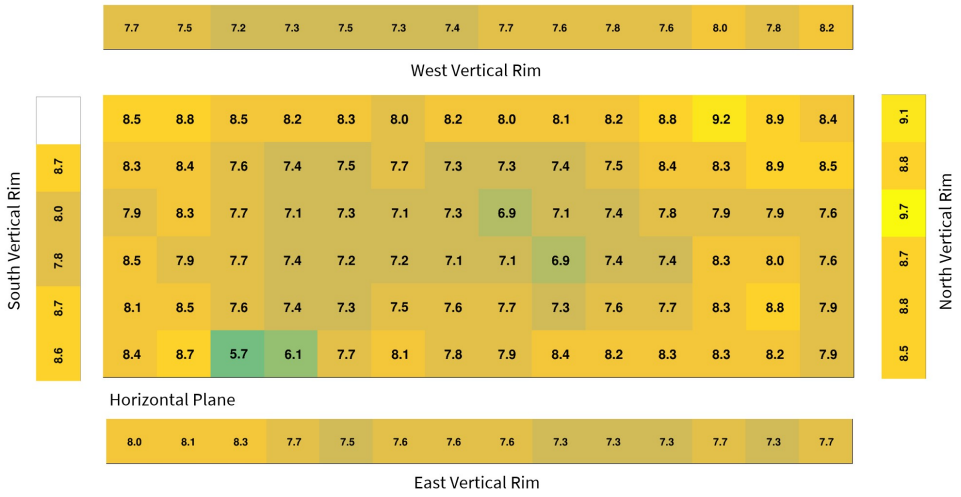

Figure 5.13: Distribution of the $\Delta t_{CRT-Flash}$ standard deviations per each module, overlayed on its relative position in the Top CRT mapping

likely to have emitted the collected scintillation light.

5.3.1 Scintillation light production

The production mechanism of the scintillation light in liquid argon is known since several decades, literature offers extensive descriptions and its spectrum is well known[68]. Ionizing particles traveling in LAr produce free excitons and electron-hole pairs. Free excitons and holes are self-trapped within about 1 ps and result into excited, Ar_2^*, or ionized, Ar_2^+, argon dimers. Ar_2^+ recombines with a thermalized electron to form Ar_2^* which decays non-radiatively to the first singlet and triplet states $^1\Sigma_u^+$ and $^3\Sigma_u^+$. The dis-excitation of these two states leads to the emission of the scintillation light with a very different lifetime: $\sim$ ns $^1\Sigma_u^+$ and $\sim \mu s$ for $^3\Sigma_u^+$. The scintillation light photon yield for a minimum ionizing particle is $\sim 4.1{\times}10^4\ \gamma/MeV$ in absence of electric field. In ICARUS, considering an electric field of 500 V/cm, the expected yield is $\sim 2.4{\times}10^4\ \gamma/MeV$.

5.3.2 Least time path

An improved analysis requires precise topological information of the crossing cosmic tracks. Potentially, a track trajectory reconstructed with the TPC data is able to provide all the topological information needed (the track direction and its position at each point), unfortunately, the CRT hit to TPC track matching was not in production at the time of this thesis. Nevertheless, the CRT-PMT matching algorithm was able to provide a golden sample of cosmic tracks entering from the Top CRT, generating a flash in the liquid

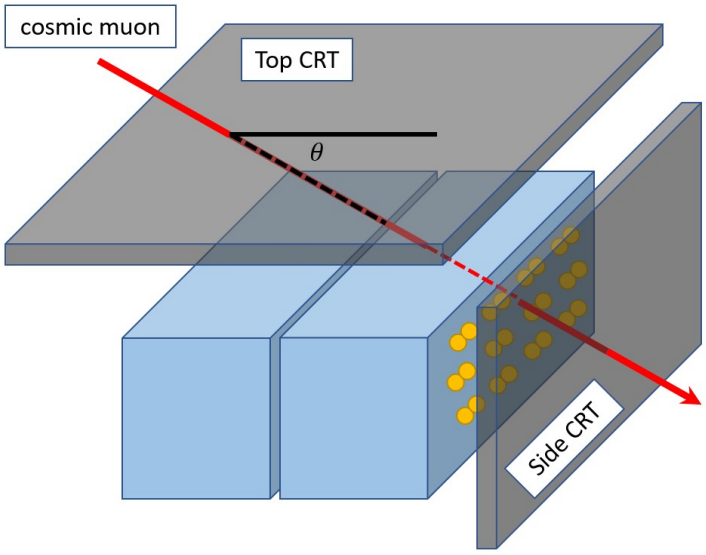

Figure 5.14: Sketch of the golden sample of tracks entering from the Top CRT, generating a flash inside the liquid argon and exiting from the Side CRT. θ is incidence angle with respect to the detector plane.

argon and exiting from the Side CRT. This sample is reported in Table 5.1 and it consists of ∼86k tracks. Figure 5.14 shows an illustration of the golden sample used for this analysis. Thanks to the precise spatial position of the reconstructed Top and Side CRT hits, by assuming that the cosmic muon is straight-going and does not scatter along its path, the cosmic track direction is reconstructed in the parametric form $r(\ell, m, n)$ of the straight line that connects the two CRT hits. The distribution of the incidence angle θ of the selected tracks (w.r.t. the detector plane, see Figure 5.14) is shown in Figure 5.15. The selected tracks are entering with an average wide 37° angle with respect to the CRT horizontal plane.

An additional selection was applied to identify cosmic tracks that are crossing the PMT plane and hitting the Side CRT East or West walls. This cut was chosen to study a sample in which the Side CRT reconstruction is homogeneous, without possible systematics due to the different hit reconstruction performed on the South and the North Side CRT walls. Finally, a further cut was applied to use only cosmic tracks where the Side CRT hits were reconstructed on both the inner and outer layers by two FEBs, removing conditions in which the CRT hit position is assigned by default into the central point of the scintillator strip. Following these cuts, the surviving sample was 57k tracks out of the initial 86k (∼66%).

For each track, we can create a geometrical model in which we can estimate the position along the track (inside the liquid argon active volume)

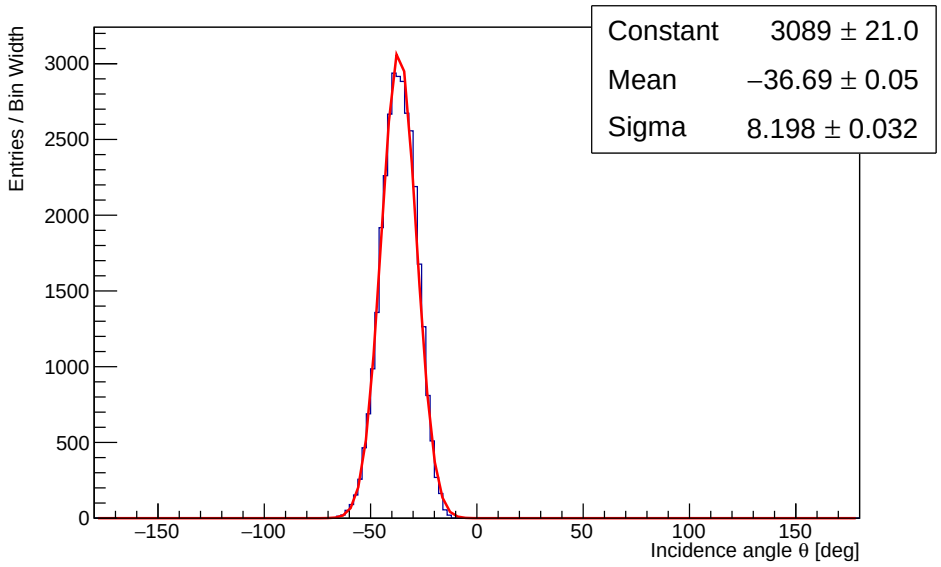

Figure 5.15: Distribution of the incidence angle θ of the selected cosmic tracks entering from the Top CRT, generating a flash in the liquid argon, and exiting through the Side CRT. The incidence angle is calculated w.r.t. to the Top CRT horizontal plane.

from which the first photon collected by a certain PMT is most likely emitted. This model is based on the assumption that the muons are relativistic, therefore their travel speed in liquid argon is comparable to the speed of light c and the emitted scintillation photons propagate in liquid argon at speed c/n, where n is the refractive index of the liquid argon. Figure 5.16 shows an illustration of the model assumed for this analysis, where T and S are the Top and Side CRT hits respectively, the black arrow is the cosmic muon track, the dashed lines are the path of photons reaching the PMT (P) produced at two different positions along the track: D is the closest point of the track to the PMT and d is its distance, E is the position from which the first photon collected by the PMT is most likely emitted and x is its relative distance w.r.t. D. The E position is obtained by minimizing the sum of the cosmic travel time from the Top CRT hit and the photon propagation time:

$$t_{tot}(x) \equiv t_\mu + t_\gamma = \frac{1}{c}(\overline{TD} - x) + \frac{n}{c}\sqrt{x^2 + d^2} \tag{5.4}$$

$$\frac{dt_{tot}(x)}{dx} = 0 \rightarrow x_e = \frac{d}{\sqrt{n^2 - 1}} \tag{5.5}$$

where x_e is distance from D for which the t_{tot} is minimal. The earliest photon reaching a certain PMT is (most likely) emitted with an angle α

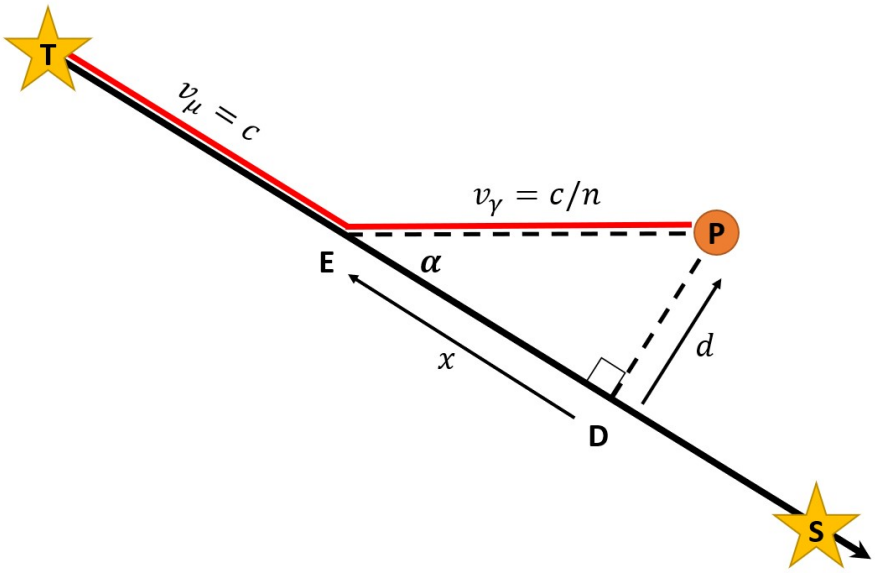

Figure 5.16: Least time path (red) for a cosmic muon entering from the Top CRT (T), generating scintillation light recorded by the PMTs (P) and exiting from the Side CRT (S). α is the emission angle of the earliest photon reaching a certain PMT and E is the most likely emission position.

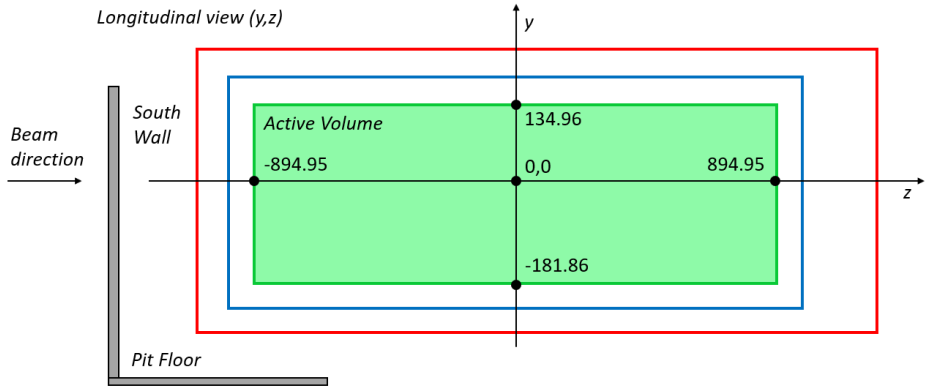

Figure 5.17: Active volume coordinates in the in the longitudinal view. Coordinates are in cm and the illustration is not in scale.

which depends only on the liquid argon refraction index n:

$$\sin^2 \alpha = \frac{n^2 - 1}{n^2} \tag{5.6}$$

assuming a refraction index $n \simeq 1.36$, $\alpha \simeq 43°$.

The model described up to this point, is intrinsically dependent on the refractive index of the liquid argon. For this analysis, an *effective* liquid argon refraction index n_{eff} was considered. The n_{eff} was estimated by a recent published result of a direct measurement of the light group velocity in liquid argon, $\frac{1}{v_g} = 7.46 \pm 0.08$ ns/m, where v_g is the group velocity [69]. The effective refraction index can be derived from:

$$n_{eff} = c/v_g \tag{5.7}$$

where c is the speed of light in vacuum. The result is n_{eff} ~2.24 and this value was used to determine the propagation time of the first photon and the corresponding emission angle $\alpha(n_{eff}) \sim 63.5°$.

An additional selection cut was applied to consider only tracks where the earliest emission photon point (E in Figure 5.16) is within the liquid argon active volume (illustrated in Figure 5.17 and Figure 5.18). This last selection was driven by the necessity to remove situations in which, accounting for geometrical acceptance of the PMT, the least time path model is not valid anymore. Following this latter cut, the survival sample is 44651 tracks, corresponding to $\sim$ 52% of the initial cosmics entering from the Top CRT and exiting from the Side CRT.

The determination of the least time path for the propagation of the cosmic muon and the scintillation light to each PMT allows to determine the fastest travel time according to equation 5.4. In this improved analysis, the

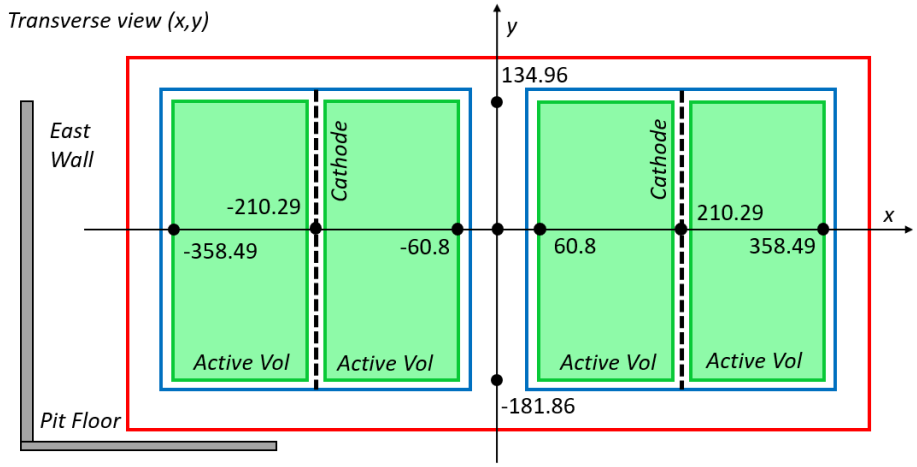

Figure 5.18: Active volume coordinates in the in the transverse view. Coordinates are in cm and the illustration is not in scale.

CRT-PMT matching time resolution can be obtained by plotting the residual (Δt) between the measured CRT-PMT time difference and the evaluated overall time along the fastest path:

$$\Delta t = \Delta t_{CRT-hit} - t_{FP} \tag{5.8}$$

where $\Delta t_{CRT-hit}$ is the difference between the CRT hit time and the first optical hit that composes the optical flash and t_{FP} is the propagation time along the fastest path. The fastest path was evaluated considering the position of the PMT that collected the first optical hit. Figure 5.19 shows the distribution of the residuals Δt considering the path from the Top CRT hit to the PMT associated with the first PMT.

As previously described, the scintillation light emitted from the point E is not isotropic and the first photon collected by each PMT is produced after a certain delay determined by the fast scintillation light lifetime. In order to consider also the scintillation light emission component, the Δt distribution was fitted with a model composed by the convolution of a Gaussian distribution with an exponential decay. The $\Delta t_{CRT-hit}$ time resolutions considering the Top CRT hits is determined by the Gaussian sigma and it includes both PMT and CRT timing resolutions and any other unaccounted physics effect. The exponential decay was chosen to describe the fast scintillation light emission. Overall the model considered three free parameters: the *bias* and the σ from the Gaussian distribution and the lifetime τ (the inverse of the exponential decay constant). The fit was performed using the ROOFIT analysis framework and the results are presented in Figure 5.20. The results of the fit show a *bias* $\sim$ -0.8 ns and a $\sigma < 3.7$ ns, with a systematic error

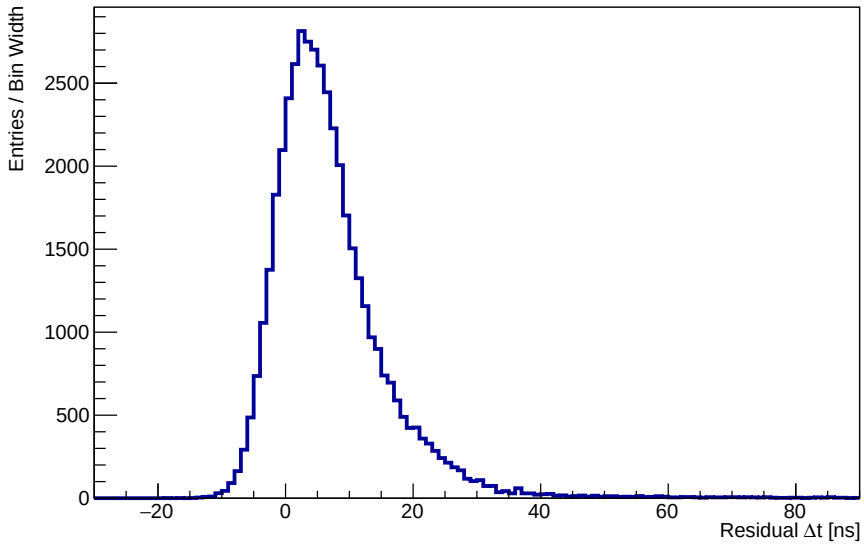

Figure 5.19: Distribution of the residual Δt between the measured $\Delta t_{CRT-hit}$ for The Top CRT hits and the evaluated overall travel time along the fastest path.

of the order of $\sim$ 1 ns and negligible statistical error. The lifetime of the convoluted exponential is $\sim$ 7.8 ns, this value is in agreement with the τ_f values reported in literature.

The results presented in this section show that using a sample of tracks for which the cosmic track direction can be reconstructed (in this case by means of the CRT system) a time resolution better than 4 ns can be achieved. These results can be obtained only if precise topological information of the cosmic track are available and this is true, as reported in Table 5.1, for 4.6% of the matched optical flashes. Once a proper CRT hit and TPC track matching algorithm will be available, this analysis can be extended to a larger sub-sample of tracks. In addition, these promising results highlight the possibility to perform measurements of the liquid argon proprieties as such as lifetime and refraction index measurements.

5.4 CRT-PMT based neutrino event selection

The results of section 5.1 can be exploited to perform a preliminary event selection only by means of CRT and PMT information. The CRT-PMT based classification is applied to all the flashes in the acquisition window; Figure 5.1 shows that the optical flashes associated with the primary event trigger have a clear signature distribution peaked at 600 ns before the trigger signal

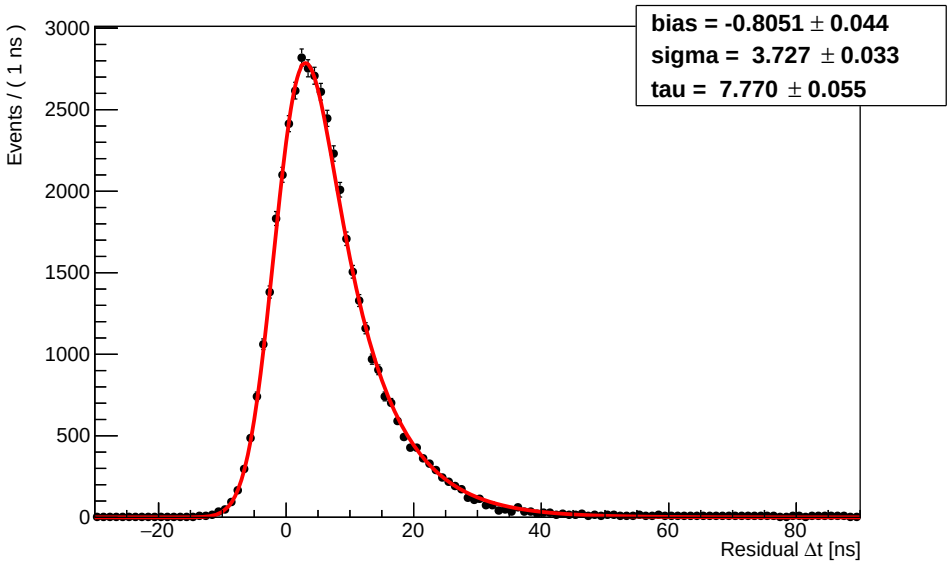

Figure 5.20: Fit of the residual Δt using a Gaussian convoluted with an exponential decay. Only the Top CRT hits are considered.

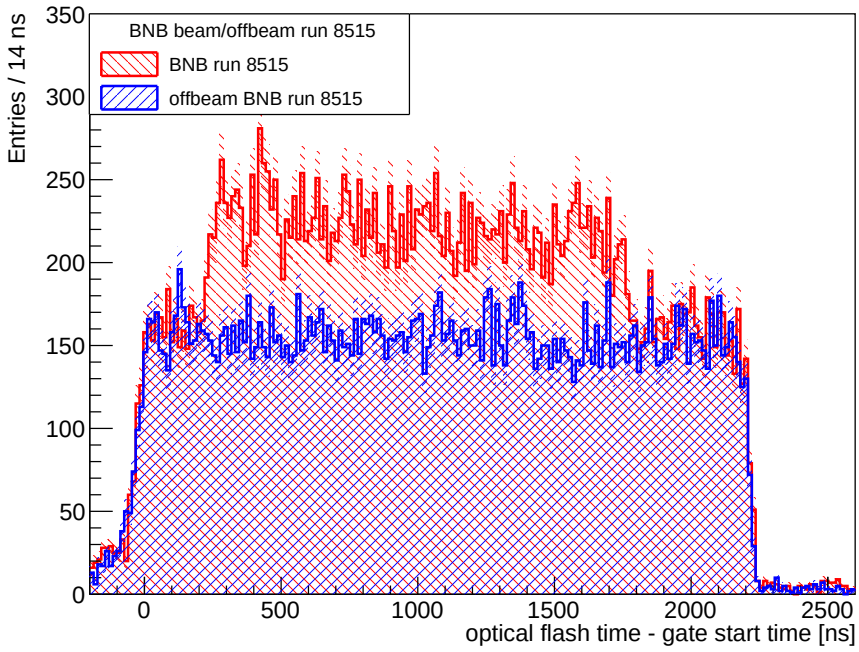

Figure 5.21: Distribution of the optical flashes time w.r.t. the beam gate opening for the BNB sample (red) and the offbeam BNB sample (blue).

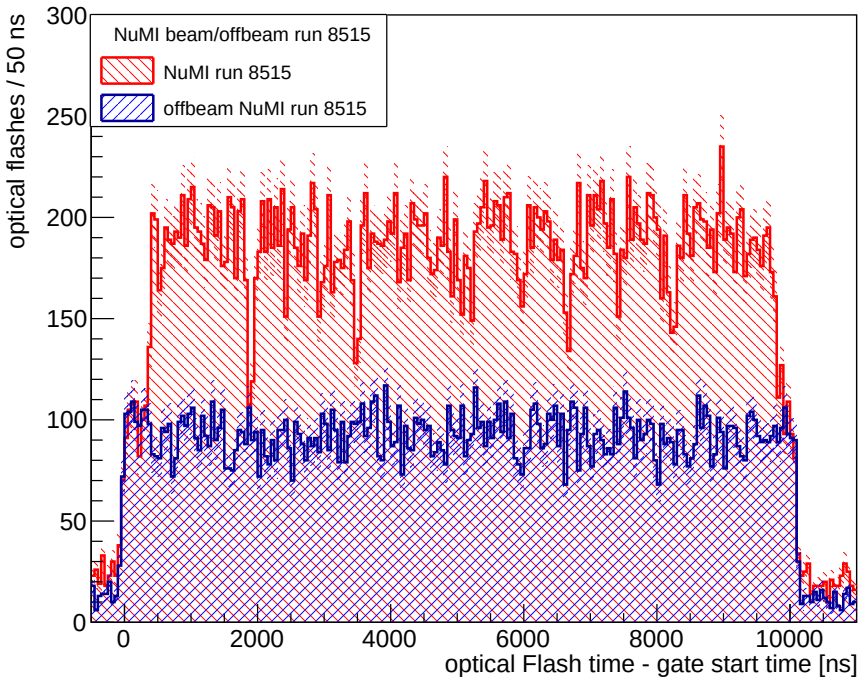

Figure 5.22: Distribution of the optical flashes time w.r.t. the beam gate opening for the NuMI sample (red) and the offbeam NuMI sample (blue). The structure of the 6 batches of protons per spill extracted in the Main Injector is visible.

formation, therefore by considering only the optical flash associated with primary event trigger (or in general considering all the optical flashes within the beam spill) the classification presented in section 5.1 can be applied for event selection purposes.

The advantages of a CRT-PMT based event classification are multiple, an example is the potentiality to perform a preliminary filtering of interesting events ahead of the slow and computationally heavy processing of all the TPC waveforms, reducing the overall processing time.

In order to study the effectiveness of a CRT-PMT based event selection, run number 8515 collected during the Run 1 of ICARUS was studied using the CRT-PMT matching analysis. Run 8515 started on June 23 2022 and the total duration of the run was 106 hours corresponding to $0.3{\cdot}10^{18}$ POTs for BNB and $5.4{\cdot}10^{18}$ POTs for NuMI. This analysis used both beam and offbeam events (for background evaluation) for both NuMI and BNB. Following the processing of the events and the intrinsic inefficiencies of the job submission, the final data sample used for this analysis is: 31039 events for BNB, 23958 events for offbeam BNB, 30325 events for NuMI and 16608 events for offbeam NuMI.

As a first step of this analysis, only the events with one or more optical flashes inside the spill were selected. The distribution of the optical flashes time was evaluated w.r.t. the beam gate opening time. Figure 5.21 shows the overlap of the BNB and offbeam BNB data sample; the BNB beam spill window (1.6 μs long) is contained within the 2.2 μs enlarged beam gate width. The excess of optical flashes due to beam related activities (red) is visible w.r.t. the offbeam baseline (blue).

Figure 5.22 shows the overlap of the NuMI and offbeam NuMI data sample; the NuMI beam spill (9.6 μs long) is contained within the 10 μs enlarged beam gate width. The excess of optical flashes due to beam related activity (red) is visible w.r.t. the offbeam baseline (blue). An interesting feature that can be inferred from the NuMI optical flashes excess is the 6 batches structure due to the proton batches injection from the Booster to the Main Injector.

The CRT-PMT matching was performed on all the optical flashes within the beam spill window (200-1800 ns w.r.t. the BNB gate for BNB and 200-9800 ns w.r.t. the NuMI gate for NuMI) for both the beam and offbeam data sample.

5.4.1 BNB event classification

Overall, for the BNB and offbeam BNB data sample 25189 and 17696 optical flashes were respectively found within the BNB spill window. The flash classification was obtained by considering the amount of matched CRT hits and the relative timing, the results for BNB and offbeam BNB are reported in Figure 5.23 and Figure 5.25 respectively, Figure 5.24 and Figure 5.26 show

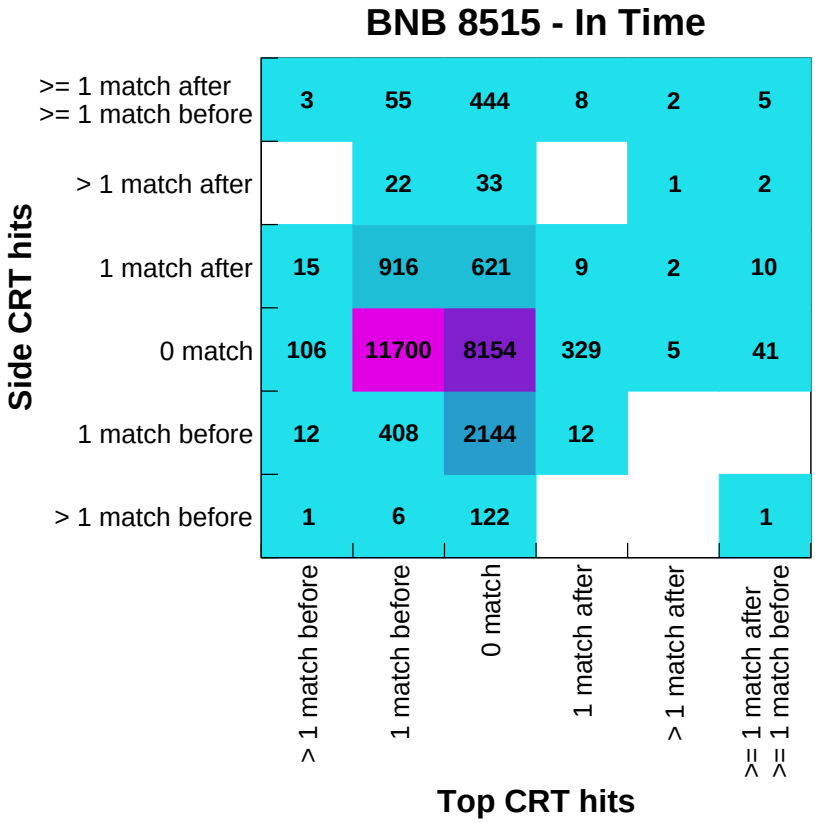

Figure 5.23: Number of optical flashes within the BNB spill matched with Top and Side CRT hits. The analyzed sample is 31039 BNB events from run 8515, corresponding to 25189 optical flashes within the beam spill window.

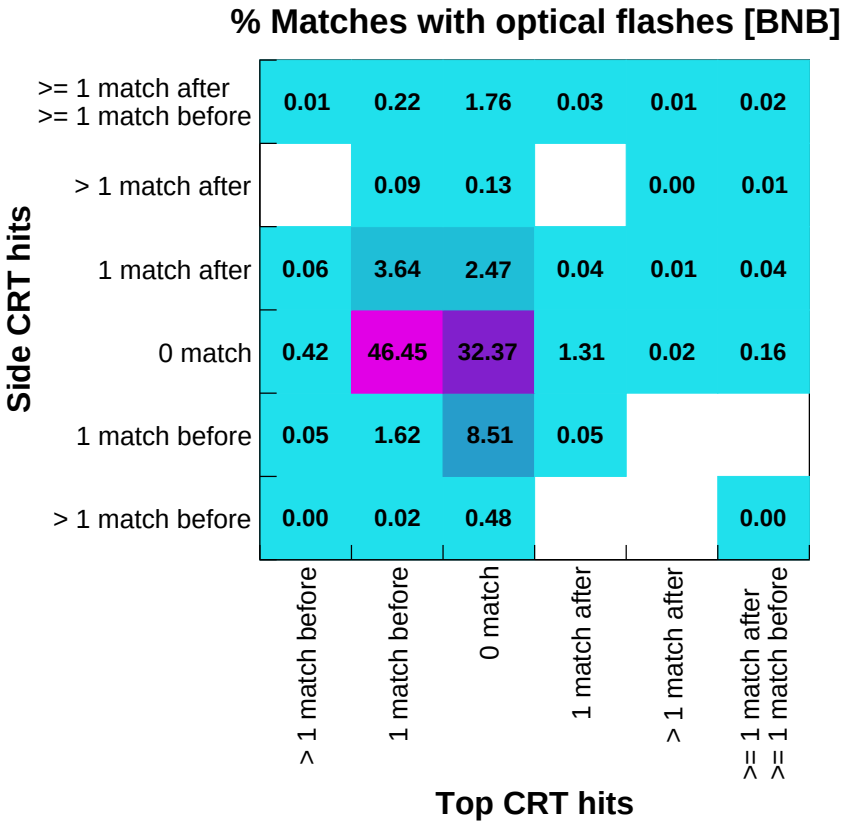

Figure 5.24: Relative percentage of optical flashes within the BNB spill matched with Top and Side CRT hits for the BNB sample.

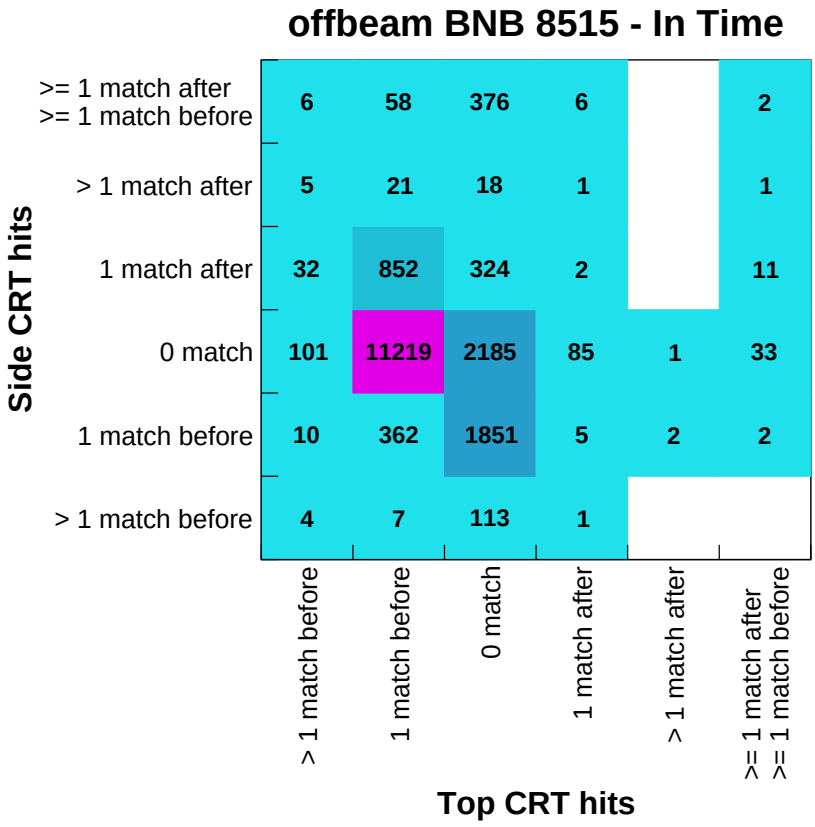

Figure 5.25: Number of optical flashes within the offbeam BNB gate (inside the BNB spill window) matched with Top and Side CRT hits. The analyzed sample is 23958 offbeam BNB events from run 8515, corresponding to 17696 optical flashes within the beam spill window.

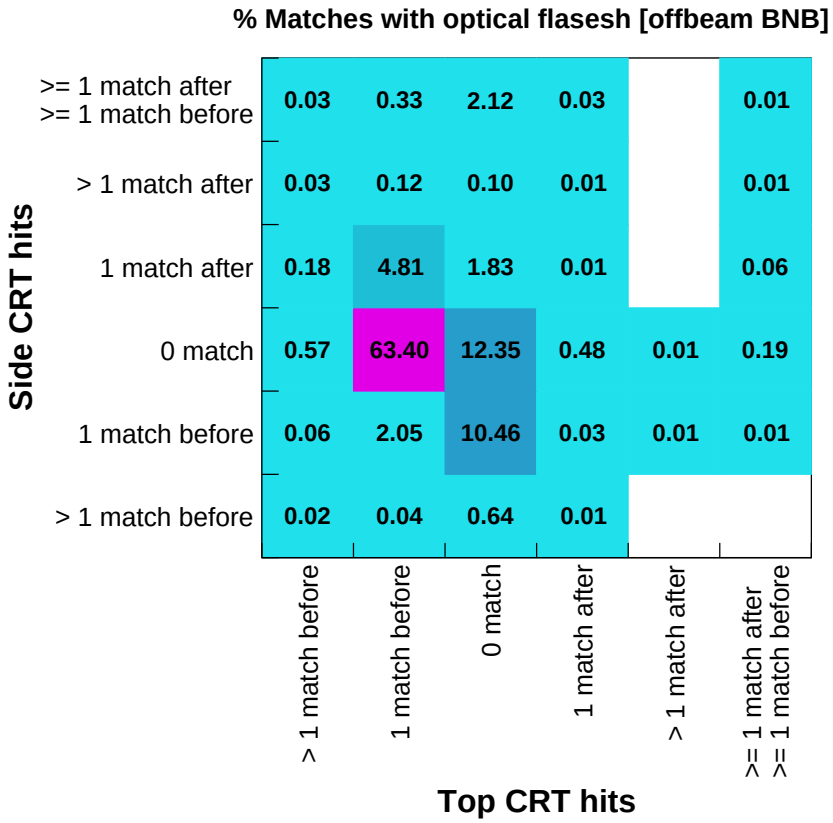

Figure 5.26: Relative percentage of optical flashes within the offbeam BNB gate (inside the BNB spill window) matched with Top and Side CRT hits for the offbeam BNB sample.

the corresponding percentages w.r.t. the selected number of optical flashes.

	BNB		offbeam BNB	
Classification	**Entries**	**%**	**Entries**	**%**
No CRT match	8154	32.37	2185	12.35
1 Entering from Top	11700	46.45	11219	63.40
1 Entering from Side	2144	8.51	1851	10.46
1 Entering from Top 1 Exiting from Side	916	3.64	852	4.81
1 Exiting from Top	329	1.31	85	0.48
1 Exiting from Side	621	2.47	324	1.83
Others	1325	5.26	1180	6.67

Table 5.2: Classification of the BNB and offbeam BNB run 8515 data sample using the matched CRT hits information.

Table 5.2 shows a direct comparison of the flash classification for BNB and offbeam BNB. The offbeam BNB relative percentages are in agreement with those presented in Table 5.1. The comparison of the two datasets shows an enrichment of the class without any CRT match, as expected by fully contained neutrino interactions from the beam. Additional enriched classes are those where the optical flash is associated with only one exiting CRT hit on both the Top or the Side CRT, possibly due to not fully contained ν_μ CC interactions with muon exiting and hitting the CRT planes.

The classification of the optical flashes matched with CRT hits allows to perform a preliminary selection of neutrino candidate interactions. Figure 5.27 shows a ν_μ CC candidate interaction that was selected with the requirement that the optical flash was not matched with any CRT hit. The processed event was studied using the event display and the neutrino candidate interaction was found; the muon candidate was fully contained within the LAr volume.

The results of this analysis on the BNB case show that, for an analysis of fully contained neutrino interactions, the request of no CRT matches with an optical flash rejects $\sim$ 68 % of the full BNB data sample, corresponding to an analogous data reduction and faster analysis.

5.4.2 NuMI event classification

Overall, for the NuMI and offbeam NuMI data sample 35687 and 17756 optical flashes were respectively found within the NuMI spill window. The flash classification was obtained by considering the amount of matched CRT hits and the relative timing, the results for NuMI and offbeam NuMI are reported in Figure 5.28 and Figure 5.30 respectively, Figure 5.29 and Figure 5.31 show the corresponding percentages w.r.t. the selected number of optical flashes. Table 5.3 shows a direct comparison of the flash classification for NuMI and offbeam NuMI. The offbeam NuMI relative percentages are in

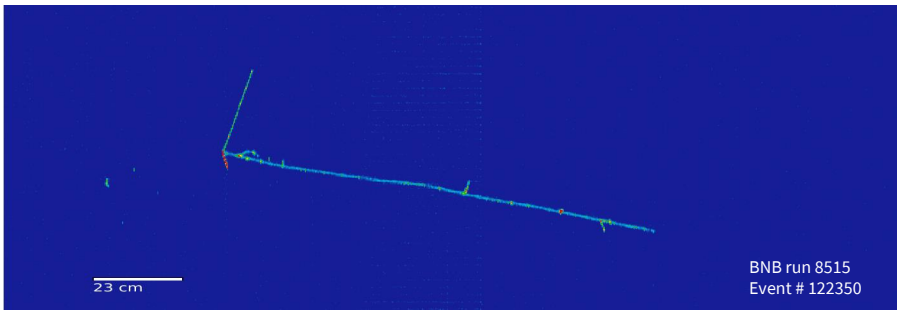

Figure 5.27: Example of one ν_μ CC candidate selected from the BNB run 8515 data sample where one optical flash within the BNB beam spill was not matched with any CRT hit.

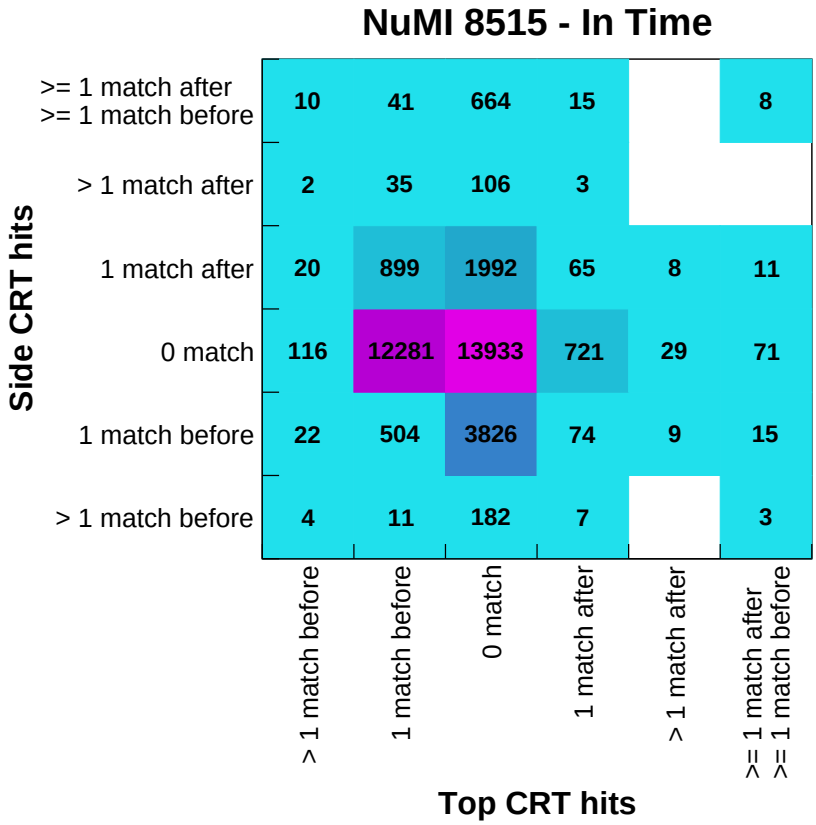

Figure 5.28: Number of optical flashes within the NuMI spill matched with Top and Side CRT hits. The analyzed sample is 30325 NuMI events from run 8515, corresponding to 35687 optical flashes within the beam spill window.

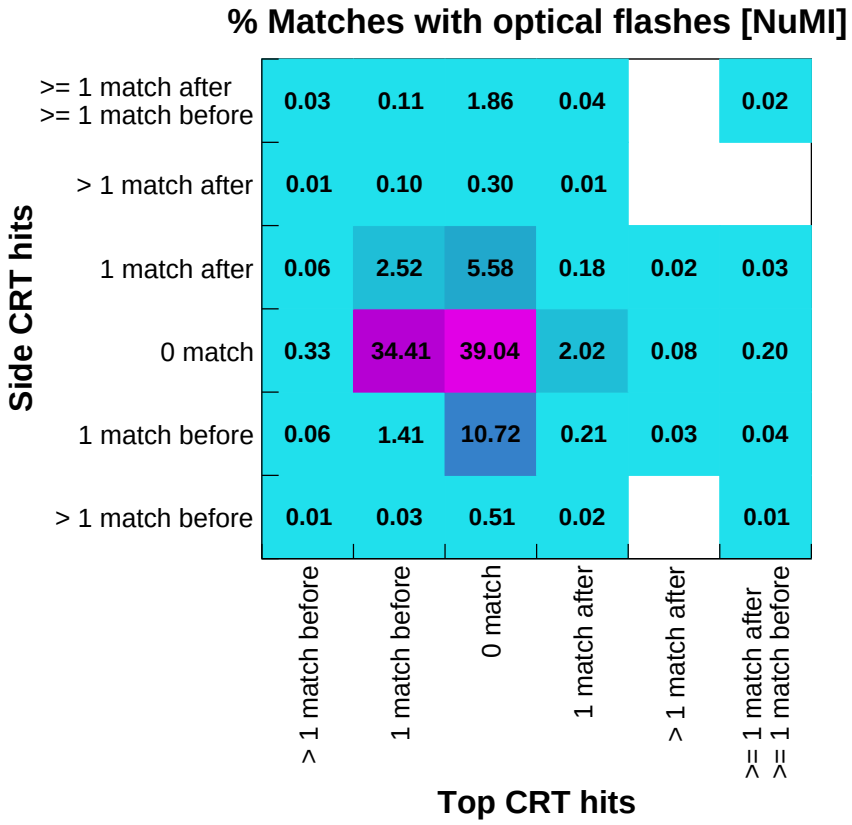

Figure 5.29: Relative percentage of optical flashes within the NuMI spill matched with Top and Side CRT hits for the NuMI sample.

	NuMI		offbeam NuMI	
Classification	**Entries**	**%**	**Entries**	**%**
No CRT match	13933	39.04	2257	12.71
1 Entering from Top	12281	34.41	111154	62.82
1 Entering from Side	3826	10.72	1856	10.45
1 Entering from Top 1 Exiting from Side	899	2.52	839	4.73
1 Exiting from Top	721	2.02	85	0.48
1 Exiting from Side	1992	5.58	333	1.88
Others	2035	5.71	1232	6.94

Table 5.3: Classification of the NuMI and offbeam NuMI run 8515 data sample using the matched CRT hits information.

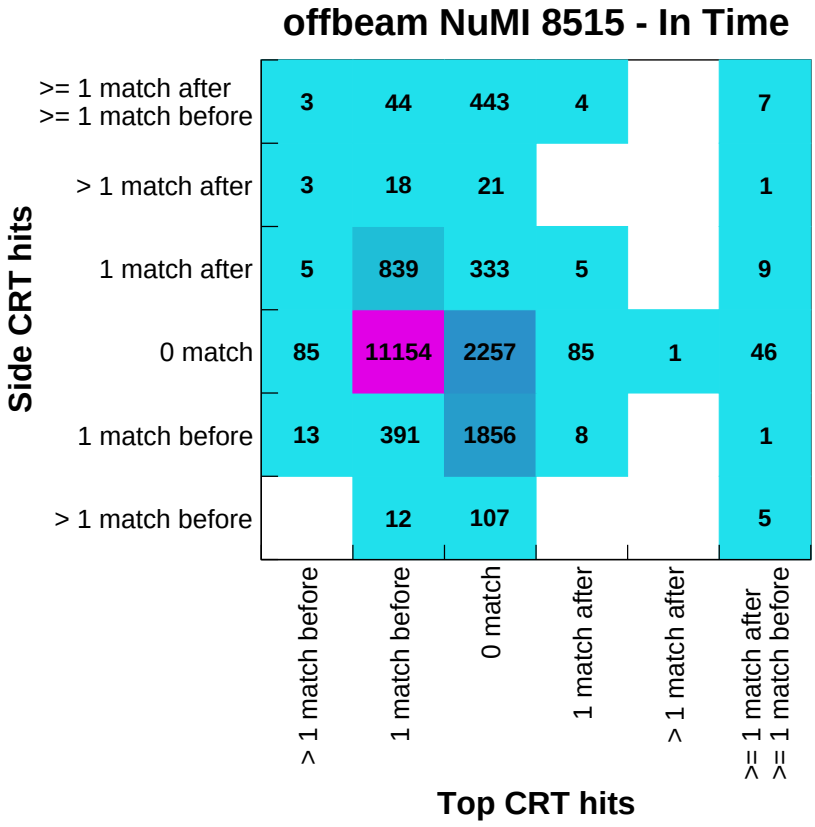

Figure 5.30: Number of optical flashes within the offbeam NuMI gate (inside the NuMI spill window) matched with Top and Side CRT hits. The analyzed sample is 16608 offbeam NuMI events from run 8515, corresponding to 17756 optical flashes within the beam spill window.

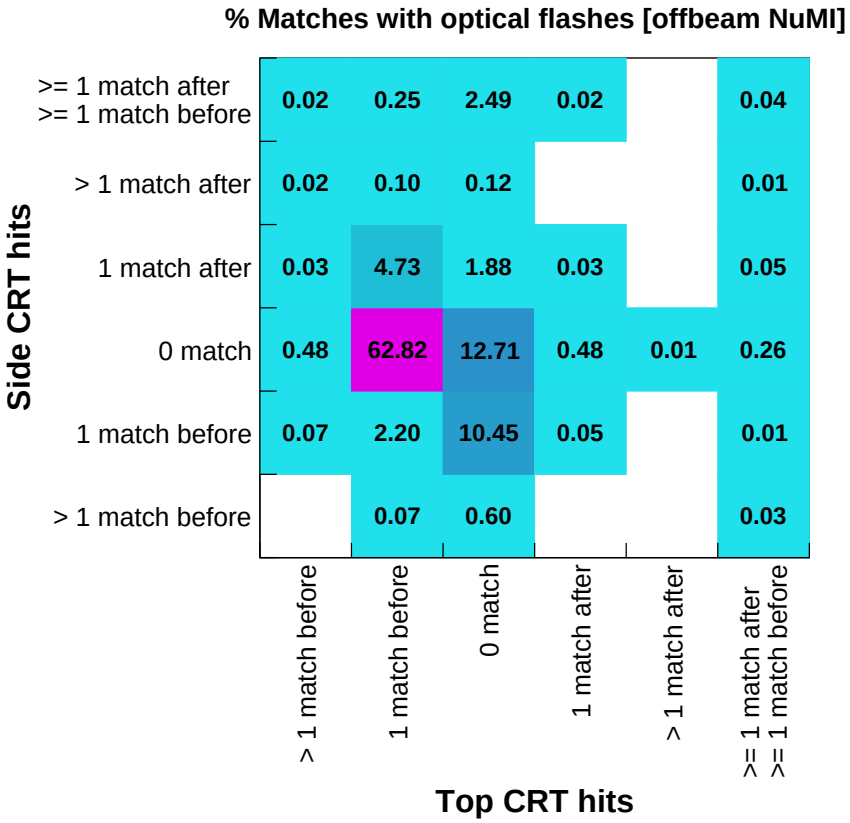

Figure 5.31: Relative percentage of optical flashes within the offbeam NuMI gate (inside the NuMI spill window) matched with Top and Side CRT hits for the offbeam NuMI sample.

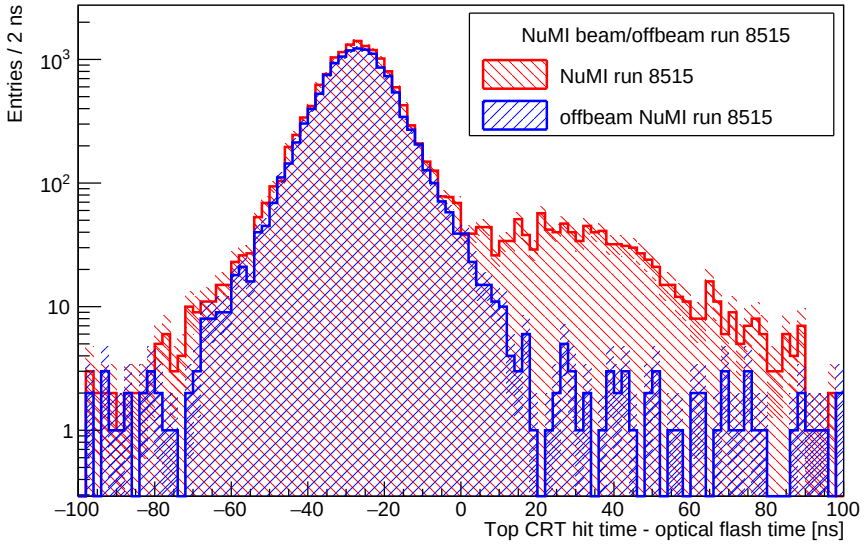

Figure 5.32: Distribution in logarithmic scale of the $\Delta t_{CRT-Flash}$ for Top CRT hits matched with optical flashes within the NuMI beam spill window for the beam sample (red) and offbeam sample (blue). The enhanced region with positive $\Delta t_{CRT-Flash}$ due to not fully contained ν_μ CC interactions is visible.

agreement with those presented in Table 5.1. In analogy with the BNB case, an enrichment is seen for the class without any CRT match and those where the optical flash is followed CRT hit on both the Top or the Side CRT. In the latter classes, the relative is percentage is bigger w.r.t the BNB case, this is expected since the NuMI neutrinos are more energetic, therefore the muons are longer and have an higher probability to reach the further CRT planes. A more detailed study on the analysis of not fully contained ν_μ interactions from the NuMI is presented in section 5.4.2.

The results of this analysis on the NuMI case show that, for selection of fully contained neutrino interactions, the request of no CRT matches with an in beam time optical flash rejects $\sim$ 61 % of the full NuMI data sample, corresponding to an analogous data reduction and faster analysis.

NuMI: not fully contained muons

The study on the event selection of not fully contained ν_μ was performed on the NuMI data sample since it shows, according to Table 5.3, a rich population of optical flashes matched with exiting CRT hits. In particular, this study focuses only on muons exiting through the Top CRT detector roof. Figure 5.32 shows the overlapped distribution of the $\Delta t_{CRT-Flash}$ for Top

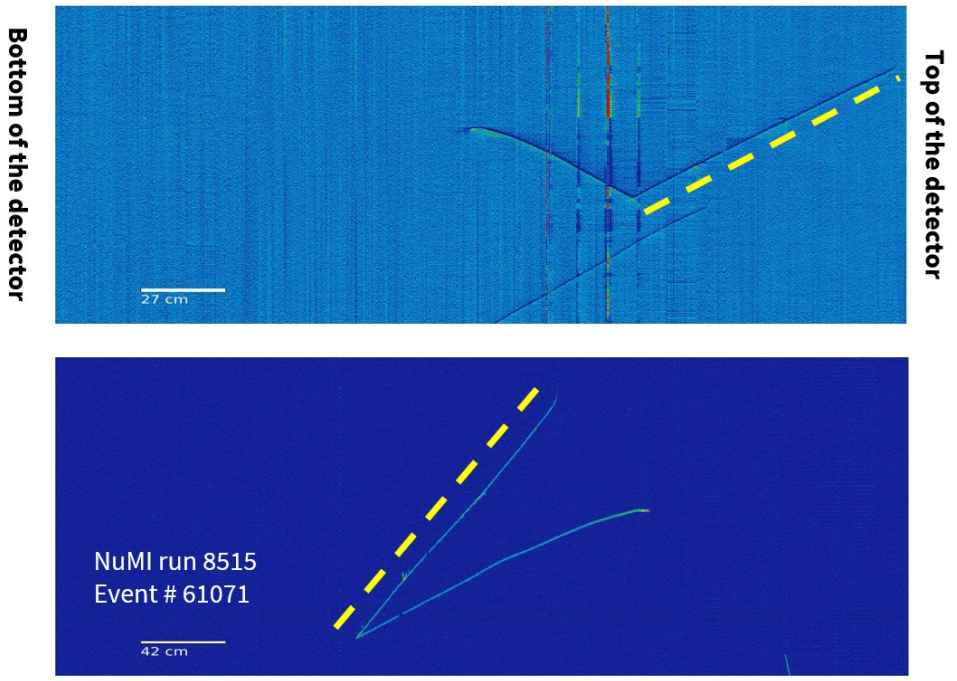

Figure 5.33: Visually identified QE-like ν_μ CC candidate from the NuMI data sample (event 61071) where the muon candidate (dotted line) is moving towards the top.

CRT hits from NuMI (red) and offbeam NuMI (blue) in logarithmic scale; an excess in the positive regions is visible due to beam related activity.

An event scanning campaign was performed to study some of the optical flashes associated with only one Top CRT hit in the positive $\Delta t_{CRT-Flash}$ region, in particular in the 25-40 ns region, where the Signal-to-Noise ration (~ 10) is higher. 70 events were selected and visually scanned: 27 showed the signature of ν_μ CC-like interactions where the muon was not fully contained an going towards the Top of the detector; 27 showed activity associated with *rock muons* (ν_μ interactions with the rock surrounding the detector) or activity behind the wire planes; for 16 of them it was not possible to precisely identify the track associated with the optical flash.

Figure 5.33 and Figure 5.34 report two ν_μ CC-like interactions visually scanned in this analysis where the muon candidate (dotted yellow line) is not fully contained and it is directed towards the Top CRT. This validation with the visual scanning was restricted to NuMI fully contained events.

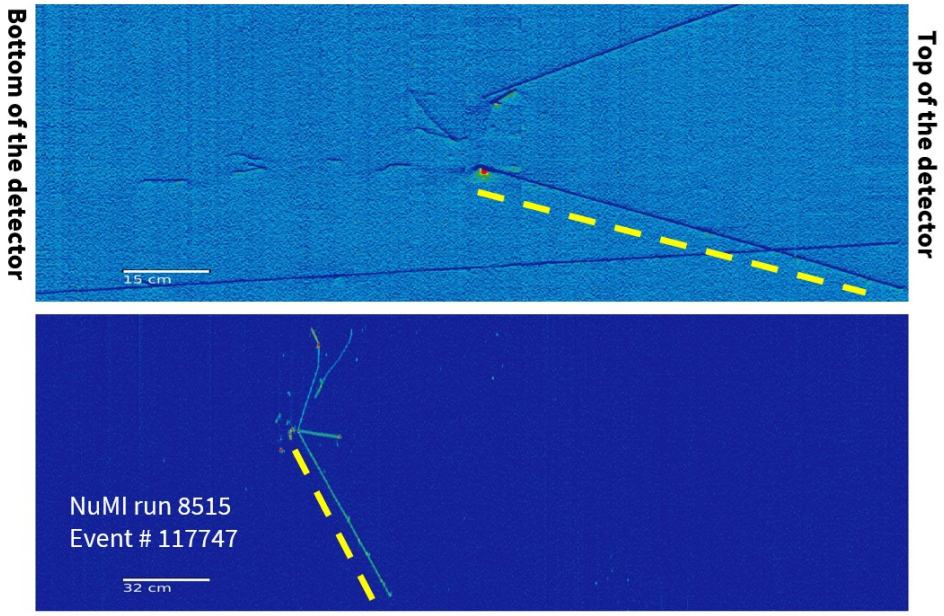

Figure 5.34: Visually identified ν_μ CC candidate with lot of activity (two electromagnetic showers possibly associated with a π^0 are also visible) from the NuMI data sample (event 117747) where the muon candidate (dotted line) is moving towards the top.

5.5 Prospects

The CRT-PMT matching proved to be a useful and effective tool that can perform a preliminary event selection, rejecting events where the optical flashes are matched with clear cosmic like signatures. Depending on the analysis, the requirements on the selections can be more or less stringent, for example, beam induced charged activity entering from the Side CRT should not be rejected for sensitive BSM searches on the NuMI off-axis beam, in order not to cut potential BSM signals.

Even though for a small sample of events, the CRT-PMT matching preliminary selection capabilities have been exploited in the identification of both samples of fully contained and not fully contained ν_μ CC-like events by the event scanners.

Additionally, the CRT-PMT match was used to perform data-driven calibration of the CRT timing system and it showed the potentiality to perform measurements of liquid argon properties.

The next improvement is foreseen with the inclusion of algorithm to match a TPC reconstructed track with one or more CRT hits. The CRT-TPC track matching algorithm is essential to definitively provide an evaluation of the CRT tagging efficiency and to perform an effective cosmic background removal.

Conclusions

The ICARUS detector at Fermilab is located along the Booster Neutrino Beamline 600 m from neutrino source and at 6° off axis with respect to the NuMI beamline, $\sim$ 800 m from the proton target. ICARUS is the first large-scale LArTPC detector which formerly had operated at the Gran Sasso underground laboratory. At Fermilab the detector is located at shallow depth, thus exposed to a large flux of cosmic particles crossing the detector during the $\sim$ 1 ms long drift time of the TPC. In order to mitigate the cosmogenic background, ICARUS is instrumented with a Cosmic Ray Tagger system, ensuring a 4π coverage of the liquid argon volume. The cosmic tagger, organized into three different subsystems (Top, Side and Bottom CRT), covers a surface area of $\sim$ 1100 m^2.

The Top CRT is composed of 123 hodoscope modules deployed on top of the ICARUS cryostat. The modules, which were built and tested at the INFN-LNF in Italy, have an average tagging efficiency greater than 96%. They were shipped to FNAL at the beginning of 2021 and their installation was carried out in Q4 2021. During the commissioning of the Top CRT system, started in January 2022, the delays along the timing signal distributions were accurately measured. Before their integration in the data acquisition system, the modules were tested and a calibration campaign of the $\sim$ 4000 readout channels of the Top CRT was performed. Each channel was characterized in terms of SiPM pedestal and Gain. Six broken channels were found, the corresponding inactive detector surface is $\sim$ 2.5 m^2, 0.3% of the whole Top CRT surface. A modification of the CRT triggering logic which would enable the recovery of the dead surface is planned. The commissioning of the Top CRT was completed satisfactorily by the beginning of April 2022, setting the start of the installation on top of it of a 3 m concrete overburden. Since April 2022, the Top CRT modules are all included in the detector data acquisition system and constantly monitored. The commissioning of ICARUS was completed in mid June 2022, with the full installation of the concrete overburden. The Top CRT offered a unique tool to monitor the gradual reduction in the cosmic ray flux reaching the detector surface: the average rate per module decreased from $\sim$ 600 Hz to $\sim$ 330 Hz, in agreement with the absorption of the soft electromagnetic and hadronic components of the cosmic ray flux.

The CRT and the photon detection systems use the digitized global trigger signal as time reference for their relative synchronization. The precise measurement and correction of all the delays along the timing distribution lines determined a ns-scale alignment of both the CRT and PMT subsystems. A CRT-PMT matching tool was developed using the relative time between a CRT hit and an optical flash as the main matching criterion, determining the direction (entering or exiting the TPC) of a cosmic particle and, possibly, the nature of the triggering event, i.e. whether or not associated with a cosmic particle. The results of the CRT-PMT matching were studied to address both the *in time* (optical flashes within the beam gate) and *out of time* (optical flashes during the drift time) samples, to determine the performance of the matching procedure as a cosmic background rejection tool. A cosmics only sample was selected using part of the offbeam BNB data sample acquired during the ICARUS Run 1, including ~ 1.9 millions optical flashes, and it was determined that $\sim 62\%$ were preceded by a Top CRT hit, $\sim 11\%$ by a Side CRT hit and, neglecting the other classifications, $\sim 12\%$ were not matched with any CRT. Geometrical effects and intrinsic inefficiencies are mainly responsible for this latter value. The matching algorithm was then tested on both the in-time data sample for both the BNB and NuMI data for one run of ICARUS Run 1 (run 8515). The relative percentage of the in-time optical flashes not matched with any CRT hit significantly increases to ~ 32 (39)% for BNB (NuMI) with respect to the out of beam sample.

The events with in-time optical flashes not matched with any CRT hit were selected to perform an event scanning campaign aimed at identifying a sample of fully contained neutrino interactions. In addition, NuMI events with one *in time* optical flash followed by an exiting CRT hit on the Top CRT were studied to select a sample of not fully contained ν_μ. The CRT-PMT match was exploited to perform a data driven calibration of the CRT timing system indicating the possibility to measure relevant liquid argon properties (scintillation light emission lifetime and refractive index). The results show that using a sample of tracks for which the particle trajectory is reconstructed (in this case by means of the CRT system) a time resolution better than 4 ns can be achieved.

The background rejection capabilities of the CRT systems will be further exploited in the near future by implementing the match with TPC-reconstructed tracks. The algorithm, which is currently under development, will also allow the determination of the CRT tagging efficiency.

Bibliography

[1] W. Pauli, *Wissenschaftlicher Briefwechsel mit Bohr, Einstein, Heisenberg*, vol. 259, 1930.

[2] F. Reines and C. L. Cowan, "The neutrino," *Nature*, vol. 178, p. 446, 1956. DOI: https://doi.org/10.1038/178446a0.

[3] C. S. Wu, E. Ambler, R. W. Hayward, D. D. Hoppes, and R. P. Hudson, "Experimental test of parity conservation in beta decay," *Phys. Rev.*, vol. 105, pp. 1413–1415, 4 Feb. 1957. DOI: 10.1103/PhysRev.105.1413.

[4] M. Goldhaber, L. Grodzins, and A. W. Sunyar, "Helicity of neutrinos," *Phys. Rev.*, vol. 109, pp. 1015–1017, 3 Feb. 1958. DOI: 10.1103/PhysRev.109.1015.

[5] L. Landau, *Nuclear Physics*, vol. 3, no. 1, pp. 127–131, 1957, ISSN: 0029-5582. DOI: https://doi.org/10.1016/0029-5582(57)90061-5.

[6] T. D. Lee and C. N. Yang, "Parity nonconservation and a two-component theory of the neutrino," *Phys. Rev.*, vol. 105, pp. 1671–1675, 5 Mar. 1957. DOI: 10.1103/PhysRev.105.1671.

[7] A. Salam, "On parity conservation and neutrino mass," *Nuovo Cim.*, vol. 5, p. 299, 1957. DOI: 10.1007/BF02812841.

[8] S. L. Glashow, "Partial-symmetries of weak interactions," *Nuclear Physics*, vol. 22, no. 4, pp. 579–588, 1961, ISSN: 0029-5582. DOI: https://doi.org/10.1016/0029-5582(61)90469-2.

[9] S. Weinberg, "A model of leptons," *Phys. Rev. Lett.*, vol. 19, pp. 1264–1266, 21 Nov. 1967. DOI: 10.1103/PhysRevLett.19.1264.

[10] G. Danby *et al.*, "Observation of high-energy neutrino reactions and the existence of two kinds of neutrinos," *Phys. Rev. Lett.*, vol. 9, pp. 36–44, 1 Jul. 1962. DOI: 10.1103/PhysRevLett.9.36.

[11] K. Kodama *et al.*, "Observation of tau neutrino interactions," *Physics Letters B*, vol. 504, no. 3, pp. 218–224, 2001, ISSN: 0370-2693. DOI: https://doi.org/10.1016/S0370-2693(01)00307-0.

[12] B. Pontecorvo, "Mesonium and anti-mesonium," *Sov. Phys. JETP*, vol. 6, p. 429, 1957.

[13] V. Gribov and B. Pontecorvo, "Neutrino astronomy and lepton charge," *Physics Letters B*, vol. 28, no. 7, pp. 493–496, 1969, ISSN: 0370-2693. DOI: https://doi.org/10.1016/0370-2693(69)90525-5.

[14] Z. Maki, M. Nakagawa, and S. Sakata, "Remarks on the Unified Model of Elementary Particles," *Progress of Theoretical Physics*, vol. 28, no. 5, pp. 870–880, Nov. 1962, ISSN: 0033-068X. DOI: 10.1143/PTP.28.870.

[15] B. T. Cleveland *et al.*, "Measurement of the solar electron neutrino flux with the homestake chlorine detector," *The Astrophysical Journal*, vol. 496, no. 1, p. 505, Mar. 1998. DOI: 10.1086/305343.

[16] Q. R. Ahmad *et al.*, "Measurement of the rate of $\nu_e + d \rightarrow p + p + e^-$ interactions produced by ^8B solar neutrinos at the sudbury neutrino observatory," *Phys. Rev. Lett.*, vol. 87, p. 071 301, 7 Jul. 2001. DOI: 10.1103/PhysRevLett.87.071301.

[17] Q. R. Ahmad *et al.*, "Direct evidence for neutrino flavor transformation from neutral-current interactions in the sudbury neutrino observatory," *Phys. Rev. Lett.*, vol. 89, p. 011 301, 1 Jun. 2002. DOI: 10.1103/PhysRevLett.89.011301.

[18] Y. Fukuda *et al.*, "Evidence for oscillation of atmospheric neutrinos," *Phys. Rev. Lett.*, vol. 81, pp. 1562–1567, 8 Aug. 1998. DOI: 10.1103/PhysRevLett.81.1562.

[19] R. L. Workman *et al.*, "Review of Particle Physics," *PTEP*, vol. 2022, p. 083C01, 2022. DOI: 10.1093/ptep/ptac097.

[20] S. Bilenky, J. Hošek, and S. Petcov, "On the oscillations of neutrinos with dirac and majorana masses," *Physics Letters B*, vol. 94, no. 4, pp. 495–498, 1980, ISSN: 0370-2693. DOI: https://doi.org/10.1016/0370-2693(80)90927-2.

[21] J. Schechter and J. W. F. Valle, "Neutrino masses in su(2) $\bigotimes$ u(1) theories," *Phys. Rev. D*, vol. 22, pp. 2227–2235, 9 Nov. 1980. DOI: 10.1103/PhysRevD.22.2227.

[22] S. Weinberg, *Phys. Rev. Lett.*, vol. 43, p. 1566, 1979.

[23] S. Pascoli, "Neutrino physics," *CERN Yellow Rep. School Proc.*, vol. 6, M. Mulders and C. Duhr, Eds., pp. 213–259, 2019. DOI: 10.23730/CYRSP-2019-006.213.

[24] A. Atre, T. Han, S. Pascoli, and B. Zhang, *Journal of High Energy Physics*, vol. 2009, no. 05, p. 030, May 2009. DOI: 10.1088/1126-6708/2009/05/030.

[25] Letizia, Peruzzo, "Search for heavy neutrinos at the na48/2 and na62 experiments at cern," *EPJ Web Conf.*, vol. 182, p. 02 095, 2018. DOI: 10.1051/epjconf/201818202095.

[26] K. N. Abazajian *et al.*, *Light sterile neutrinos: A white paper*, 2012. DOI: 10.48550/ARXIV.1204.5379.

[27] C. Giunti, Y. Li, C. Ternes, and Z. Xin, "Reactor antineutrino anomaly in light of recent flux model refinements," *Physics Letters B*, vol. 829, p. 137 054, Jun. 2022. DOI: 10.1016/j.physletb.2022.137054.

[28] W. Hampel *et al.*, "GALLEX solar neutrino observations: Results for GALLEX IV," *Phys. Lett. B*, vol. 447, pp. 127–133, 1999. DOI: 10.1016/S0370-2693(98)01579-2.

[29] J. N. Abdurashitov *et al.*, "Measurement of the response of a gallium metal solar neutrino experiment to neutrinos from a ^{51}Cr source," *Phys. Rev. C*, vol. 59, pp. 2246–2263, 4 Apr. 1999. DOI: 10.1103/PhysRevC.59.2246.

[30] M. A. Acero *et al.*, *White paper on light sterile neutrino searches and related phenomenology*, 2022. DOI: 10.48550/ARXIV.2203.07323.

[31] C. Athanassopoulos *et al.*, "The liquid scintillator neutrino detector and LAMPF neutrino source," *Nuclear Instruments and Methods in Physics Research Section A: Accelerators, Spectrometers, Detectors and Associated Equipment*, vol. 388, no. 1-2, pp. 149–172, Mar. 1997. DOI: 10.1016/s0168-9002(96)01155-2.

[32] B. Armbruster *et al.*, *Physical Review D*, vol. 65, no. 11, Jun. 2002. DOI: 10.1103/physrevd.65.112001.

[33] A. Aguilar *et al.*, *Physical Review D*, vol. 64, no. 11, Nov. 2001. DOI: 10.1103/physrevd.64.112007.

[34] A. A. Aguilar-Arevalo *et al.*, "Neutrino flux prediction at MiniBooNE," *Physical Review D*, vol. 79, no. 7, Apr. 2009. DOI: 10.1103/physrevd.79.072002.

[35] A. Aguilar-Arevalo *et al.*, "The MiniBooNE detector," *Nuclear Instruments and Methods in Physics Research Section A: Accelerators, Spectrometers, Detectors and Associated Equipment*, vol. 599, no. 1, pp. 28–46, Feb. 2009. DOI: 10.1016/j.nima.2008.10.028.

[36] A. Aguilar-Arevalo *et al.*, "Updated MiniBooNE neutrino oscillation results with increased data and new background studies," *Physical Review D*, vol. 103, no. 5, Mar. 2021. DOI: 10.1103/physrevd.103.052002.

[37] A. Aguilar-Arevalo *et al.*, "Significant excess of electronlike events in the MiniBooNE short-baseline neutrino experiment," *Physical Review Letters*, vol. 121, no. 22, Nov. 2018. DOI: 10.1103/physrevlett.121.221801.

[38] A. Serebrov *et al.*, "Neutrino-4 experiment on search for sterile neutrino with multi-section model of detector," *Journal of Physics: Conference Series*, vol. 888, p. 012 089, Sep. 2017. DOI: 10.1088/1742-6596/888/1/012089.

[39] A. Serebrov *et al.*, "Search for sterile neutrinos with the neutrino-4 experiment and measurement results," *Physical Review D*, vol. 104, no. 3, Aug. 2021. DOI: 10.1103/physrevd.104.032003.

[40] M. Dentler *et al.*, "Updated global analysis of neutrino oscillations in the presence of eV-scale sterile neutrinos," *Journal of High Energy Physics*, vol. 2018, no. 8, Aug. 2018. DOI: 10.1007/jhep08(2018)010.

[41] C. Rubbia, "The liquid-argon time projection chamber: a new concept for neutrino detectors," CERN, Geneva, Tech. Rep., 1977.

[42] M. Antonello *et al.*, "A Proposal for a Three Detector Short-Baseline Neutrino Oscillation Program in the Fermilab Booster Neutrino Beam," Mar. 2015. arXiv: 1503.01520 [physics.ins-det].

[43] P. A. Machado, O. Palamara, and D. W. Schmitz, "The Short-Baseline Neutrino Program at Fermilab," *Ann. Rev. Nucl. Part. Sci.*, vol. 69, pp. 363–387, 2019. DOI: 10.1146/annurev-nucl-101917-020949. arXiv: 1903.04608 [hep-ex].

[44] V. Shiltsev, "Fermilab Proton Accelerator Complex Status and Improvement Plans," *Mod. Phys. Lett. A*, vol. 32, no. 16, p. 1 730 012, 2017. DOI: 10.1142/S0217732317300129.

[45] P. Adamson *et al.*, "The NuMI Neutrino Beam," *Nucl. Instrum. Meth. A*, vol. 806, pp. 279–306, 2016. DOI: 10.1016/j.nima.2015.08.063. arXiv: 1507.06690 [physics.acc-ph].

[46] A. Machado and E. Segreto, "Arapuca a new device for liquid argon scintillation light detection," *Journal of Instrumentation*, vol. 11, no. 02, p. C02004, Feb. 2016. DOI: 10.1088/1748-0221/11/02/C02004.

[47] A. A. Machado *et al.*, "The X-ARAPUCA: An improvement of the ARAPUCA device," Apr. 2018. DOI: 10.1088/1748-0221/13/04/C04026. arXiv: 1804.01407 [physics.ins-det].

[48] R. Acciarri *et al.*, "Design and construction of the MicroBooNE detector," *Journal of Instrumentation*, vol. 12, no. 02, P02017–P02017, Feb. 2017. DOI: 10.1088/1748-0221/12/02/p02017.

[49] P. Abratenko *et al.*, "Search for neutrino-induced neutral-current Δ radiative decay in microboone and a first test of the miniboone low energy excess under a single-photon hypothesis," *Phys. Rev. Lett.*, vol. 128, p. 111 801, 11 Mar. 2022. DOI: 10.1103/PhysRevLett.128.111801.

[50] P. Abratenko *et al.*, "Search for an anomalous excess of charged-current quasielastic ν_e interactions with the microboone experiment using deep-learning-based reconstruction," *Phys. Rev. D*, vol. 105, p. 112 003, 11 Jun. 2022. DOI: 10.1103/PhysRevD.105.112003.

[51] P. Abratenko *et al.*, "Search for an anomalous excess of charged-current ν_e interactions without pions in the final state with the microboone experiment," *Phys. Rev. D*, vol. 105, p. 112 004, 11 Jun. 2022. DOI: 10.1103/PhysRevD.105.112004.

[52] P. Abratenko *et al.*, "Search for an anomalous excess of inclusive charged-current ν_e interactions in the microboone experiment using wire-cell reconstruction," *Phys. Rev. D*, vol. 105, p. 112 005, 11 Jun. 2022. DOI: 10.1103/PhysRevD.105.112005.

[53] P. Abratenko *et al.*, "Search for an excess of electron neutrino interactions in microboone using multiple final-state topologies," *Phys. Rev. Lett.*, vol. 128, p. 241 801, 24 Jun. 2022. DOI: 10.1103/PhysRevLett.128.241801.

[54] P. Abratenko *et al.*, "First Constraints on Light Sterile Neutrino Oscillations from Combined Appearance and Disappearance Searches with the MicroBooNE Detector," *Phys. Rev. Lett.*, vol. 130, no. 1, p. 011 801, 2023. DOI: 10.1103/PhysRevLett.130.011801. arXiv: 2210.10216 [hep-ex].

[55] F. Arneodo *et al.*, "Performance Of A Liquid Argon Time Projection Chamber Exposed To The WANF Neutrino Beam," *Phys. Rev. D*, vol. 74, p. 112 001, 2006. DOI: 10.1103/PhysRevD.74.112001. arXiv: physics/0609205.

[56] M. Antonello *et al.*, "Operation and performance of the icarus t600 cryogenic plant at gran sasso underground laboratory," *Journal of Instrumentation*, vol. 10, no. 12, P12004, Dec. 2015. DOI: 10.1088/1748-0221/10/12/P12004.

[57] B. Behera and the ICARUS collaboration, "Cosmogenic background suppression at the icarus using a concrete overburden," *Journal of Physics: Conference Series*, vol. 2156, no. 1, p. 012 181, Dec. 2021. DOI: 10.1088/1742-6596/2156/1/012181.

[58] P. Abratenko *et al.*, "ICARUS at the Fermilab Short-Baseline Neutrino Program – Initial Operation," Tech. Rep., 2023. arXiv: 2301.08634.

[59] H. de Kerret *et al.*, "The double chooz antineutrino detectors," *The European Physical Journal C*, vol. 82, no. 9, Sep. 2022. DOI: 10.1140/epjc/s10052-022-10726-x.

[60] D. Michael *et al.*, "The magnetized steel and scintillator calorimeters of the minos experiment," *Nuclear Instruments and Methods in Physics Research Section A: Accelerators, Spectrometers, Detectors and Associated Equipment*, vol. 596, no. 2, pp. 190–228, 2008, ISSN: 0168-9002. DOI: https://doi.org/10.1016/j.nima.2008.08.003.

[61] *DT5702, 32 Channel SiPM Readout Board for Cosmic Rays Veto BOXED.* [Online]. Available: https://www.caen.it/products/dt5702/.

[62] *A 32-channel front-end ASIC designed to readout silicon photo-multipliers (SiPM) for scientific instrumentation application.* [Online]. Available: https://www.weeroc.com/products/sipm-read-out/citiroc-1a.

[63] A. Aduszkiewicz and R. Rechenmacher, "Dt5702 data corruption," *SBN internal note*, vol. 18683-v4, Jul. 2020.

[64] R. Brun and F. Rademakers, *Nucl. Inst. and Meth. in Phys. Res.*, vol. A 389, pp. 81–86, 1997.

[65] D. Allan, "Statistics of atomic frequency standards," *Proceedings of IEEE*, vol. 54, pp. 221–230, 1966.

[66] P. Moreira, J. Serrano, T. Wlostowski, P. Loschmidt, and G. Gaderer, "White rabbit: Sub-nanosecond timing distribution over ethernet," in *2009 International Symposium on Precision Clock Synchronization for Measurement, Control and Communication*, 2009, pp. 1–5. DOI: 10.1109/ISPCS.2009.5340196.

[67] R. L. Workman *et al.*, "Review of Particle Physics," *PTEP*, vol. 2022, pp. 520–527, 2022. DOI: 10.1093/ptep/ptac097.

[68] E. Segreto, "Properties of Liquid Argon Scintillation Light Emission," *Phys. Rev. D*, vol. 103, no. 4, p. 043 001, 2021. DOI: 10.1103/PhysRevD.103.043001. arXiv: 2012.06527 [physics.ins-det].

[69] M. Babicz *et al.*, "A measurement of the group velocity of scintillation light in liquid argon," *Journal of Instrumentation*, vol. 15, no. 09, P09009, Sep. 2020. DOI: 10.1088/1748-0221/15/09/P09009.